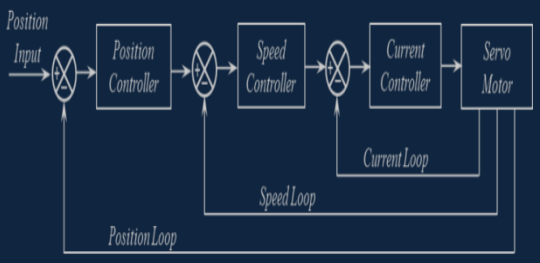

International Advanced Researches and Engineering Journal

e-ISSN

2618-575X

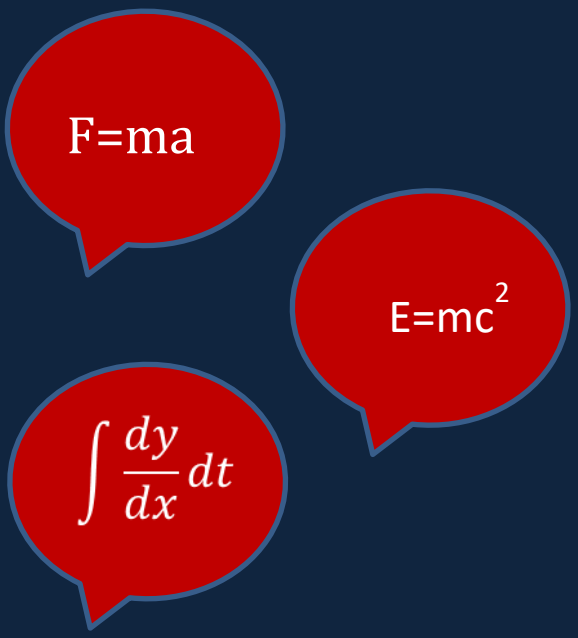

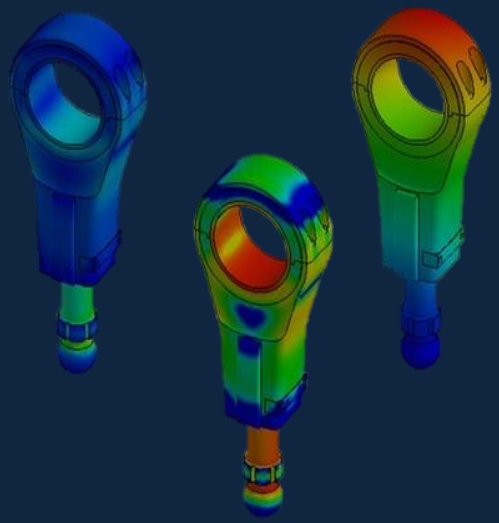

Volume 09 | **Issue** 01

April, 2025

e-ISSN: 2618-575X

Available online at www.dergipark.org.tr/en

INTERNATIONAL ADVANCED RESEARCHES
and
ENGINEERING JOURNAL

Journal homepage: www.dergipark.org.tr/en/pub/iarej

International
Open Access

Volume 09
Issue 01
April, 2025

International Advanced Researches and Engineering Journal (IAREJ) is a double-blind peer-reviewed and publicly available online journal that has Editorial Board (https://dergipark.org.tr/en/pub/iarej/board). The editor in chief of IAREJ welcomes the submissions that cover theoretical and/or applied researches on **Engineering** and related science with Engineering. The publication language of the Journal is **English**. **Writing Rules** are given in Author Guidelines (https://dergipark.org.tr/en/pub/iarej/writing-rules). IAREJ publishes **original papers** that are research papers and technical review papers.

IAREJ publication, which is **open access**, is **free of charge**. There is no article submission and processing charges (APCs).

IAREJ is indexed & abstracted in:

Crossref (Doi prefix: 10.35860/iarej.)
Directory of Open Access Scholarly Researches (ROAD)
Directory of Research Journals Indexing (DRJI)
EBSCO
Google Scholar
Index Copernicus (ICI Journal Master List)
J-Gate
TUBITAK ULAKBIM TR Dizin (TR index)
WorldCAT

Authors are responsible from the copyrights of the figures and the contents of the manuscripts, accuracy of the references, quotations and proposed ideas and the Publication Ethics (https://dergipark.org.tr/en/pub/iarej/page/4240).

Available online at www.dergipark.org.tr/en

INTERNATIONAL ADVANCED RESEARCHES
and
ENGINEERING JOURNAL

Journal homepage: www.dergipark.org.tr/en/pub/iarej

International
Open Access

Volume 09
Issue 01

April, 2025

e-ISSN: 2618-575X

TABLE of CONTENTS

Available online at www.dergipark.org.tr/en

INTERNATIONAL ADVANCED RESEARCHES
and
ENGINEERING JOURNAL

Journal homepage: www.dergipark.org.tr/en/pub/iarej

e-ISSN: 2618-575X

International Open Access

Volume 09
Issue 01

April, 2025

Research Article

Multi-Objective optimization of a parabolic trough solar power plant integrated with an organic Rankine cycle: based on high pressure and working fluid mass flow rate

Ömer Faruk GÜLER [a]

[a]*Afyon Kocatepe University, Faculty of Technology, Afyon, 03200, Turkey*

ARTICLE INFO

Article history:
Received 23 September 2024
Accepted 29 January 2025
Published 23 April 2025

Keywords:
Multi-objective optimization
PTC solar energy plant
Thermoeconomic analysis

ABSTRACT

The optimization of a parabolic trough solar power plant is conducted using a multi-objective optimization algorithm in this study. Initially, the design of the plant, planned to be built in Afyonkarahisar province, is developed. Thermodynamic and thermo-economic analyses are performed based on this design. Key variables significantly affecting the system's outputs are identified as the fluid flow rate used in the Organic Rankine Cycle (ORC) and the turbine inlet pressure. A parametric study is carried out for these variables. However, optimizing the system requires more than just these parameters. The system is optimized multi-objectively, considering all relevant variables. A graphical multi-objective optimization algorithm is applied in this process. For the base case values of a 30 kg/s flow rate and 3500 kPa turbine inlet pressure, the net energy production, exergy efficiency, and unit energy cost are 0.8443 MW, 2.32%, and 0.2230 $/kWh, respectively. After optimization, the best results are achieved at a flow rate of 42 kg/s and a pressure of 4000 kPa. For the optimized case, the net energy production, exergy efficiency, and unit energy cost improve to 1.228 MW, 3.37%, and 0.1781 $/kWh, respectively.

1. Introduction

The importance of renewable energy is undeniable. For this reason, many organizations aim to transition to zero-emission energy production methods by the 2050s [1]. Among the many studies on renewable energy, solar energy research holds a significant share. Solar energy systems are continuously diversifying, and among them, concentrator solar energy systems are particularly important due to their high power density. Parabolic trough collectors (PTCs) are one of the most extensively studied systems in the literature.

Some studies focus on detailed designs and the development or improvement of components for energy facilities [2]. Others conduct system analyses to evaluate the most efficient configurations using designed components. To maximize energy utilization, exergy analyses are often performed to achieve maximum efficiency [3]. Optimized systems aim to determine the most efficient operating ranges to achieve the highest possible performance. However, as system complexity increases, the number of variables and outputs also grows. For instance, optimizing efficiency and energy production in a system with a single power-producing turbine may also reduce costs. However, in more complex systems, the points where maximum efficiency and minimum cost align may differ, or a highly efficient system may fail to produce sufficient power. At this stage, algorithms capable of optimizing multiple variables simultaneously are needed [4,5]. Multi-objective optimization algorithms address this challenge by optimizing several objective functions concurrently [6]. In various studies, both basic and multi-objective optimization algorithms have been employed [7,8]. Some studies utilize complex algorithms through software packages and built-in tools [9]. For example, Desai and Bandyopadhyay [10] designed a PTC-based system without a separate storage unit. The system included a hot fluid cycle and a Rankine cycle, using variables such as turbine inlet temperature, turbine inlet pressure, design radiation, and system size. Optimization efforts resulted in a minimum energy cost of 0.188 $/kWh. In another study [11], a more complex system was analyzed. Heat from parabolic collectors was transferred via an intermediary fluid and then stepwise into a Rankine cycle, producing energy through both high-pressure and low-pressure turbines. Using the Combined Energy-

* Corresponding author. Tel.: *+90 272 218 2536*
E-mail addresses: ofguler@aku.edu.tr *(O.F.Guler)*
ORCID: 0000-0002-3344-341X *(O.F.Guler)*
DOI: 10.35860/iarej.1554883

Exergy Control Method, which integrates energy and exergy analysis, system efficiencies of 36.06% were achieved, alongside a 25.09% improvement in system response time. After a triple optimization, energy efficiency, exergy efficiency, and response time improved to 34.02%, 28.25%, and 17.63%, respectively. Colakoğlu and Durmayaz [12] designed a complex solar energy system featuring energy production through a gas turbine and secondary utilization of the remaining energy via systems such as the Kalina Cycle and Organic Rankine Cycle (ORC). The system also provided heating and cooling. Optimization efforts enhanced the exergetic quality factor. Georgousis et al. [13] performed multi-objective optimization of a polygeneration system using a geometric approach, a method similar to the one used in this study. Modabber and Manesh [14] examined a trigeneration system incorporating a solar PTC, producing power, desalination, and heat. They analyzed parameters like unit energy cost, environmental impact, and exergy efficiency using both a multi-objective genetic algorithm and a water cycle algorithm. The latter achieved a 12.66% increase in exergy efficiency, with total operating costs of 47.4 $/h and an environmental impact of 49.2 pts/h. Esfahani et al. [15] conducted an energy, exergy, economic, and environmental analysis of a solar energy system designed for Iran. Their study showed the highest energy efficiency in July (73.6%) and the highest exergy efficiency in January (20.11%). The lowest unit exergy cost was 70.17 $/GJ in June, and CO_2 savings were 0.0193$/h. Multi-objective genetic algorithm optimization improved exergy efficiency by 6.27% and reduced total system costs by 20.36%.In another study [16], a system using different heat transfer fluids in PTCs was optimized. Mixtures like aluminum oxide, MgO, TiO, and ZnO were employed, and exergy analyses were conducted for systems combined with the Kalina Cycle. Multi-objective genetic algorithm optimization determined optimal system parameters. These studies demonstrate the critical role of multi-objective optimization in energy, efficiency, and cost analyses, especially for multi-generation systems. Complex applications like ammonia and hydrogen production, pure water generation, electricity production, and heat production require even more intricate analyses. While many researchers rely on software packages, traditional methods like one-dimensional genetic algorithms and graphical techniques are still widely used.

The novelty of this study lies in the combining conventional PTC calculations and energy system integration with economic analyses, particularly multi-objective optimization algorithm. Under the conditions of Afyonkarahisar, this modeled system not only offers a regionally applicable design but also serves as a reference for other renewable energy studies through the optimization system to be implemented. For this purpose, in this study, a parabolic trough solar energy system was designed and integrated with an ORC for energy production. In addition to traditional graphical optimization methods, a normalization algorithm was applied to the graphical data, creating a unified objective function. Energy, exergy, and economic analyses were performed to determine optimal operating conditions.

2. Method

2.1 System Description

A solar power system is being designed for implementation in Afyonkarahisar province, a region with significant solar energy potential. The system schematic is presented in Figure 1. Due to its continental climate, Afyonkarahisar experiences minimal haze, allowing abundant use of clear sunlight. According to the literature, solar irradiation values during summer range from 600 to 1000 W/m² [17]. For this study, an average irradiation value of 800 W/m² was used, consistent with common practices in reputable publications [18]. Calculations were based on a steady-state system independent of time, a standard approach for such analyses. Parabolic trough collectors (PTCs) are employed to harness solar energy. The planned installation site has an area of 50,000 m², and an appropriate number of collectors has been selected for this site. Each PTC measures 25 m by 5 m, with the system comprising 200 parallel flow groups, each containing two serial collectors. This configuration enables the achievement of high temperatures necessary for electricity generation. The working principle of PTCs involves concentrating solar energy to reach elevated temperatures. In the system, Therminol VP-1 is used as the heat transfer fluid (HTF), which is heated by the concentrated solar energy. The high-temperature fluid then transfers its heat to an ORC via a heat exchanger, enabling electricity generation. The ORC employs R-134a as the working fluid and consists of a pump, a heat exchanger, a turbine, and a condenser. R134a is a working fluid frequently used within the temperature ranges of this study. Alternative fluid selections can also be explored in a separate study [18]. Each component is modeled as a control volume under the open system assumption. The isentropic efficiencies of the turbine and pump are both assumed to be 85%. The dead state conditions, representing ambient reference values, are defined as 100 kPa and 298 K, with the subscript “0” used for notation. In this study, the system's energy and exergy efficiencies were calculated, and the system was optimized using a multi-objective optimization algorithm. Since solar irradiation was assumed to be constant, the optimization primarily focused on the ORC. The objectives included minimizing cost while maximizing net energy and exergy efficiencies. The optimization variables were the ORC turbine inlet pressure and mass flow rate.

2.2 Thermal Analysis of PTC

The maximum energy is obtained with a PTC collector is the total amount of irradiation per unit area (Eq. (1))[18].

$$Q_{in} = I.A_{tot} \tag{1}$$

Only a certain part of this energy is converted into useful energy. This converted energy can be measured from the difference between the inlet and outlet water temperatures:

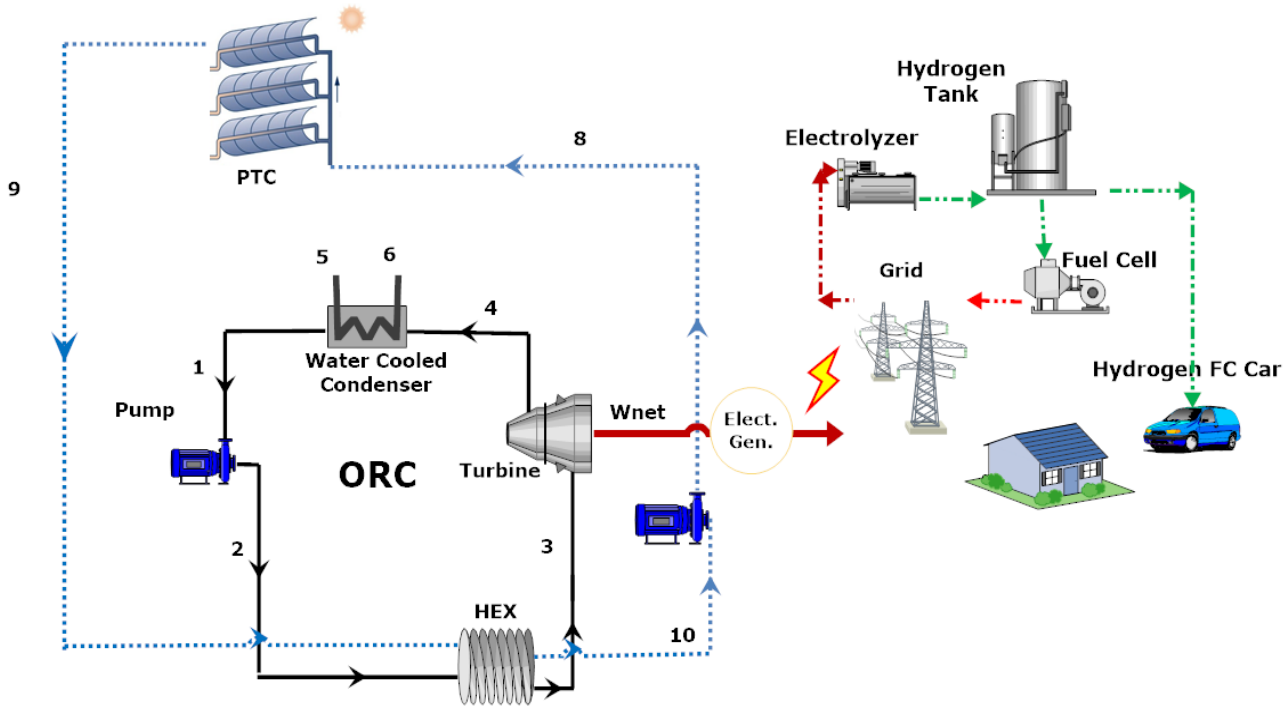

Figure 1. Schematic representation of the modeled system.

$$Q_u = \dot{m}_{tot}.C_{p,htf}.\left(T_{htf,out} - T_{htf,in}\right) \quad (2)$$

However, it is more difficult to calculate and estimate without knowing the exit temperature. For this, it is necessary to determine the losses from the collected energy. First of all, there is the concept of optical efficiency, only a part of the incoming energy can be optically focused and absorbed by the surfaces [19]. It shown in Eq. (3)

$$Q_{abs} = Q_{in}.\eta_{optical} \quad (3)$$

The optical efficiency term encompasses various factors such as transmittance, reflectance, and absorbance [20]. In this study, these factors are not detailed individually. The receiver's optical efficiency is taken as 0.806 (or 80.6%), which aligns with values reported in the literature [19].

Following optical losses, thermal losses also occur and can be analyzed as heat flow within the pipe. Determining these thermal losses requires knowledge of the surface temperatures. The analysis involves examining the heat transfer between surfaces step by step. First, heat transfer occurs between the liquid inside the pipe and the pipe wall. To quantify this, the flow characteristics within the pipe and the Nusselt number (Nu) are calculated. This step yields the useful heat transfer. Next, heat transfer occurs between the outer surface of the pipe and the glass cover. Finally, another heat transfer takes place between the glass cover and the sky or surrounding air. The heat fluxes for these thermal losses are equal, and the surface temperatures of the components are interdependent. Using an iterative approach, the heat fluxes are balanced, allowing the unknown surface temperatures to be estimated. The final, precise values are obtained after several iterations.

The outermost layer involves heat transfer between the glass cover and the sky. In this process, convection from the cover to the air and irradiation from the cover to the sky are considered. These two mechanisms are expressed as a combined heat transfer in Eq. (4) [21]. Sky temperature is Eq. (5) [22];

$$Q_{loss} = A_{co}.h_{amb}.(T_c - T_{amb}) + A_{co}.\sigma.\varepsilon_c.(T_c^4 - T_{sky}^4) \quad (4)$$

$$T_{sky} = 0.0553.T_{amb}^{1.5} \quad (5)$$

The thermal convection coefficient of air can be found by using Nusselt correlations in Eq.(6) [19].

$$Nu_{amb} = 0.193.\mathrm{Re}_{amb}^{0.618}.\mathrm{Pr}_{amb}^{0.33} \quad (6)$$

To calculate the Nusselt number, the Reynolds number from Eq. (7) is substituted into Eq. (6). Subsequently, the convection coefficient is determined by substituting the Nusselt number into Eq. (8) [23];

$$\mathrm{Re}_{amb} = \frac{u_{amb}.D_{co}}{\nu_{amb}} \quad (7)$$

$$Nu_{amb} = \frac{h_{amb}.D_{co}}{k_{amb}} \quad (8)$$

In the same way, another heat transfer surface occurs between the cover and the tube. Since this area is vacuum, only irradiation is involved and this showed in Eq. (9) [24].

$$Q_{loss} = \frac{A_{ro}.\sigma.\left(T_r^4 - T_c^4\right)}{\frac{1}{\varepsilon_r} + \frac{1-\varepsilon_c}{\varepsilon_c}.\left(\frac{A_{ro}}{A_{ci}}\right)} \quad (9)$$

The heat transfer between the flow in the innermost tube also occurs only as convection. The flow in the tube can be solved with the heat transfer model [24];

$$Q_u = A_{ri}.h_{htf}.(T_r - T_{htf,m}) \quad (10)$$

Total energy balance is;

$$Q_{abs} = Q_u + Q_{loss} \quad (11)$$

After finding the useful heat, the solar energy output temperature can be found. Thus, the temperature of the HTF that heats the ORC cycle has been determined.

2.3 Thermodynamic analysis of ORC

The cycle is then analyzed. There is a heat exchanger turbine, pump and condenser in the cycle. The energy and exergy balance of these systems is given in Table 1[25].

2.4 Economic Analysis

The interest value and future value of money are calculated according to Equations (12-15) [26];

$$F = P\left(1+i\right)^n \quad (12)$$

$$F = P\left(1+\frac{i}{p}\right)^{np} \quad (13)$$

$$i_{eff} = \left(1+\frac{i}{p}\right)^{p} - 1 \quad (14)$$

$$F = P\left(1+ni_{eff}\right) \quad (15)$$

The "cost recovery factor" (CRF) is calculated according to its lifetime and interest rate in Eq. (16) [26] to calculate the annual recovery of a cost.

$$CRF = \frac{A}{P} = \frac{i_{eff}\left(1+i_{eff}\right)^n}{(1+i_{eff})^n - 1} \quad (16)$$

If the annual levelized investment cost of the component is calculated from here, Eq. (17) is obtained [26].

$$\dot{Z}_c^{IC} = \frac{CRF}{\tau} C_c.\left(1+r_n\right)^2 \quad (17)$$

In addition to the annual levelized investment cost of the component, maintenance, and operating costs will also be included. If these costs are included, the total cost will be Eq. (18).

$$\dot{Z}_c = \dot{Z}_c^{IC} + \dot{Z}_c^{M} \quad (18)$$

Maintenance operating costs vary depending on the component. It is shown in Eq. (19).

$$\dot{Z}_c^{M} = \frac{CRF.C_{L,M}}{\tau} \frac{C_c}{\sum_k C_c} \quad (19)$$

Up to this point, only the cost of the component has been examined, its annual levelized cost. However, the system produces energy and actively each unit of energy flow or change has a cost to the system. In short, if all these changes are shown as exergy and the cost of each exergy change is calculated, the cost of each unit of exergy or the product produced on the system can also be found. This method is called the SPECO method [26].

The sum of the exergy and levelized cost of the components entering the system constitutes the cost of the products coming out. This can be shown mathematically as;

$$\dot{C}_{P,tot} = \dot{C}_{F,tot} + \dot{Z}_{tot}^{IC} + \dot{Z}_{tot}^{M} \quad (20)$$

2.5 Hydrogen Technology

Hydrogen has been a highly researched topic in recent years, serving as a critical technology for energy storage and transportation [27]. Using fuel cells, chemical energy can be converted into electrical energy, enabling hydrogen-powered electric vehicles to become a reality. In addition to its utilization, the production of hydrogen is equally important. While fossil fuel-based reforming remains a common method, electrolysis powered by renewable energy sources is gaining significance. Electrolyzers, as key hydrogen production mechanisms, are still under development and expected to see broader adoption in the future [28]. In this study, an electrolyzer and a fuel cell were incorporated into the model to simulate hydrogen production and utilization.

The modeling was conducted from a purely thermodynamic perspective, and the corresponding analyses and models are presented in Table 1. The efficiencies of the electrolyzer and fuel cell were assumed to be 70%. Although this value is below the theoretical upper limit of 83-85%, it aligns well with practical data commonly reported in the

literature [29, 30]. Although some studies use lower values, the highest practical values found in the literature were preferred in this study to better align with future projections. Additionally, the efficiencies of these systems are influenced by factors such as operating conditions, environmental impacts, and system scale. These factors can involve highly detailed analyses within their own scope.

Table 1. Thermodynamic behavior of the system components

Pump	Conservation of Mass	$\dot{m}_1 = \dot{m}_2$
	Energy Balance	$\dot{W}_p = \dot{m} v_1 (P_2 - P_1) / \eta_p$ $\eta_p = \frac{W_{p,rev}}{W_p}$
	Exergy Balance	$\dot{E}x_{dest} = W_p - W_{p,rev}$
Turbine	Conservation of Mass	$\dot{m}_1 = \dot{m}_2$
	Energy Balance	$\dot{W}_{turb} = \dot{m}_1 (h_1 - h_2)$ $\eta_{türbin} = \frac{h_1 - h_2}{h_1 - h_{2,s}}$
	Exergy Balance	$\dot{E}x_{dest} = \dot{W}_{türbin,rev} - \dot{W}_{türbin}$
Heat Exchanger	Conservation of Mass	$\dot{m}_{c,g} = \dot{m}_{c,ç} \quad \dot{m}_{h1,g} = \dot{m}_{h1,ç} \quad \dot{m}_{h2,g} = \dot{m}_{h2,ç}$
	Energy Balance	$\dot{m}_{h1,i}(h_{h,i} - h_{h,e}) = \dot{m}_{c,i}(h_{c,e} - h_{c,i})$
	Exergy Balance	$\dot{E}x_{dest} = \dot{m}_{h,i}(ex_{h,i} - ex_{h,e}) - \dot{m}_{c,i}(ex_{c,e} - ex_{c,i})$
Water Cooled Condenser	Conservation of Mass	$\dot{m}_{cool.i} = \dot{m}_{cool.e} \quad \dot{m}_i = \dot{m}_e$
	Energy Balance	$\dot{m}_{cool.i}(h_{cool,e} - h_{cool,i}) = \dot{m}_i(h_i - h_e)$
	Exergy Balance	$\dot{E}x_{dest} = \dot{m}_{cool.i}(ex_{cool.e} - ex_{cool.i}) - \dot{m}_i(ex_i - ex_e)$
PTC	Conservation of Mass	$\dot{m}_i = \dot{m}_e$
	Energy Balance	$\dot{Q}_{solar,g} = N.I.A_{col}$ $\eta_{solar} = \frac{\dot{Q}_u}{\dot{Q}_{solar,g}}$
	Exergy Balance	$\dot{E}x_{solar,in} = \dot{Q}_{solar,g}\left[1 + 0.33\left(\frac{T_0}{T_{solar}}\right)^4 - \frac{4}{3}\left(\frac{T_0}{T_{solar}}\right)\right]$ $\dot{E}x_{dest} = \dot{E}x_{solar,in} - \dot{m}_i(ex_e - ex_i)$
Electrolyzer	Conservation of Mass	$\dot{m}_{H_2O} = \dot{m}_{H_2} + \dot{m}_{O_2}$
	Energy Balance	$\eta_{Electrolyzer} = \frac{LHV_{H_2}.\dot{m}_{H_2}}{\dot{W}_{in,Electrolyzer}}$
	Exergy Balance	$\dot{E}x_{dest} = \dot{W}_{in} - E\dot{x}_{H_2}$
Fuel Cell	Conservation of Mass	$\dot{m}_{H_2} + \dot{m}_{O_2(Air)} = \dot{m}_{H_2O}$
	Energy Balance	$\eta_{FC} = \frac{\dot{W}_{out,FC}}{LHV_{H_2}.\dot{m}_{H_2}}$
	Exergy Balance	$\dot{E}x_{dest} = E\dot{x}_{H_2} - \dot{W}_{out}$

2.6 Multi-objective Optimization

Optimization plays a crucial role in many engineering applications [31,32]. In this study, optimization is performed based on cost, net work output, and exergy efficiency. To integrate these objectives, a multi-objective optimization algorithm was developed, allowing the simultaneous optimization of multiple variables[33]. A graphical approach was employed to facilitate this process, allowing different functions to be represented on a common graph. Initially, the variation range of the cost function was plotted. The minimum point on this graph, representing the optimal cost, was assigned a value of 1. Conversely, the maximum cost, representing the worst-case scenario, was assigned a value of 0. This normalization process is mathematically expressed using the normalization algorithm provided in Eq. (21).

$$1-\frac{C_n - C_{min}}{Cmin_{max}} \quad (21)$$

The same process was applied to net work output and efficiency term, aiming for maximization. Values within the selected range were calculated, with the highest marked as "1" and the lowest as "0." Normalization was performed accordingly in Eq. (22) and Eq. (23).

$$1-\frac{W_{\max}-W_n}{W_{\max}-W_{min}} \quad (22)$$

$$1-\frac{\eta_{ex,\max}-\eta_{ex,n}}{\eta_{ex,\max}-\eta_{ex,min}} \quad (23)$$

After completing these operations, the net work output, cost, and efficiency were transformed into three normalized functions ranging between 0 and 1. A common objective function was then created graphically. Since this study involves three objectives, a weight coefficient was assigned to each, with their sum equaling 1. If all objectives are equally important, the weights are set to 1/3, 1/3, 1/3. However, if cost is prioritized over net work output, its coefficient is assigned a value greater than 1/3, while the other coefficients adjust to maintain the total sum of 1 (e.g., 0.4, 0.3, and 0.3, or 0.2, 0.3, and 0.5). Similarly, if net work output or efficiency is prioritized, their respective coefficients are increased. The resulting combined objective function is expressed in Eq. (24).

$$A_0 = a_1\left(1-\frac{W_{\max}-W_n}{W_{\max}-W_{min}}\right)+a_2\left(1-\frac{C_n-C_{\min}}{C_{\max}-C_{\min}}\right) +a_3\left(1-\frac{\eta_{ex,\max}-\eta_{ex,n}}{\eta_{ex,\max}-\eta_{ex,min}}\right) \quad (24)$$

$$a_1+a_2+a_3=1$$

3. Results

Performing an energy analysis of the system reveals the amount of net power it can generate. Net power production depends on various parameters of the system. Some of these factors are external, such as the amount of solar energy, which cannot be altered by operators. However, there are also operating and design variables that affect the performance of the system. Particularly in the case of the ORC cycle, altering system parameters significantly affects energy efficiency. The T-s diagram of the ORC cycle for the base case scenario is provided in Figure 2. The turbine inlet pressure is 3500 kPa, and the condenser inlet pressure is 780 kPa. The critical pressure is 4000 kPa, which has been set as the upper limit for optimization. At a solar irradiation level of 800 W/m², the solar energy system reaches a maximum temperature of 441 K. When this thermal energy is transferred to R-134a through the heat exchanger, the ORC system achieves a maximum temperature of 417 K. The minimum temperature in the ORC system is evaluated at the condenser outlet, calculated as 303 K. The turbine inlet pressure and the mass flow rate of the working fluid are significant variables influencing the system's outputs, making them the selected parameters for optimization.

First parameter is the turbine inlet pressure. Increasing this pressure at certain rates can increase system performance. Again, the mass flow rate of the fluid in the system is also effective on system performance. These two variables also influence the system's costs. The variations in mass flow rate and net energy output in the ORC were analyzed at a constant pressure, as shown in Figure 3. In this graph, the net energy output reaches its maximum at a mass flow rate of 42 kg/s. This represents the optimal point where the energy transferred in the heat exchanger is most effectively absorbed by the working fluid.

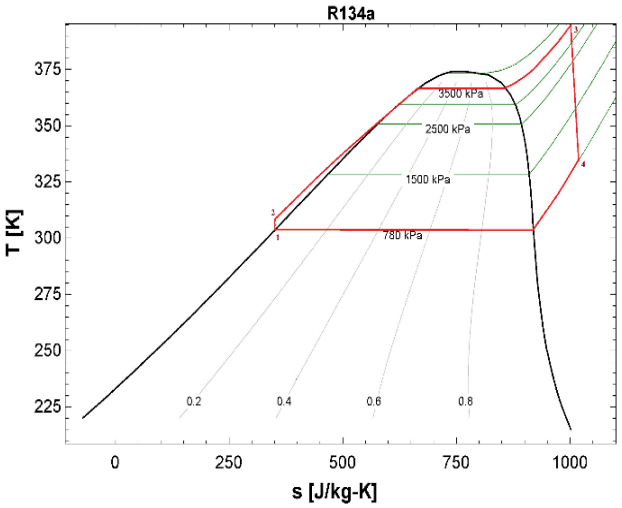

Figure 2. ORC diagram on the T-s graph of R134-a

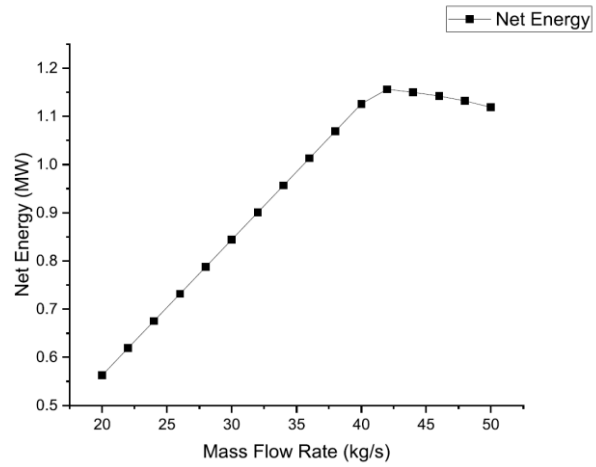

Figure 3. Produced net energy vs. mass flow rate

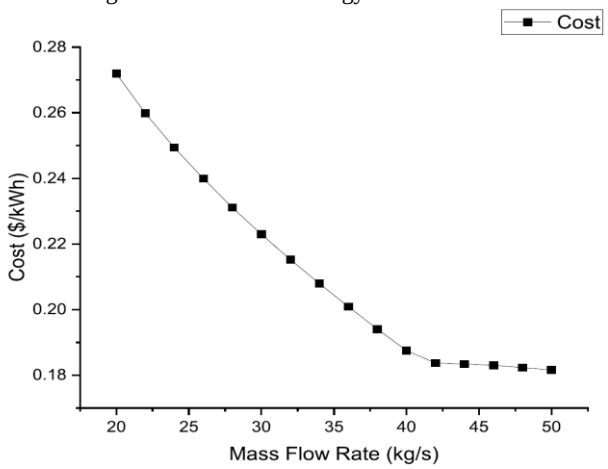

Figure 4. Unit cost of energy vs. mass flow rate

Similarly, when mass flow rate and cost are examined alone, there is a cost that decreases with increasing mass flow rate in Figure 4. However, this decrease is not linear. After the value of 42 kg/s the decreasing trend is getting lower. The lowest cost is at 50 kg/s.

In the previous graphs, the pressure was held constant. Comparable results were observed when varying the pressure while maintaining a constant mass flow rate, aligned with the base case scenario. Figure 5. illustrates how changes in pressure affect the net energy output. The net energy exhibits a polynomial trend, with diminishing growth as pressure increases. It peaks at 4000 kPa, the upper limit of the studied range. Although the curve might reach a maximum beyond 4000 kPa, such values were excluded from the study due to the onset of supercritical conditions. While systems operating above critical pressure do exist, a more detailed analysis of the system would be required for such scenarios.

An economic analysis was conducted with a base case system flow rate of 30 kg/s, as depicted in Figure 6. A unit energy cost curve was generated by varying the mass flow rate. The results indicate that unit energy cost decreases as the pressure increases.

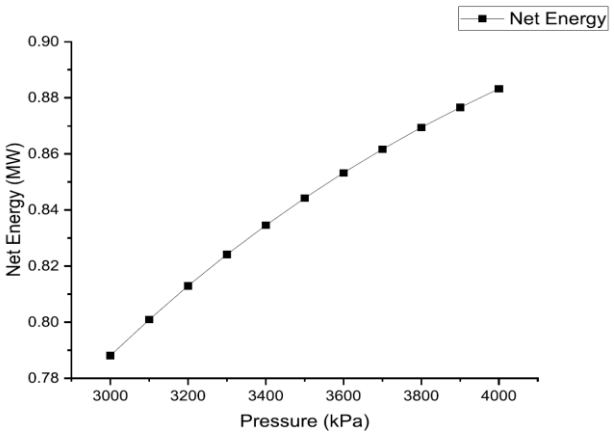

Figure 5. Produced net energy vs. turbine pressure

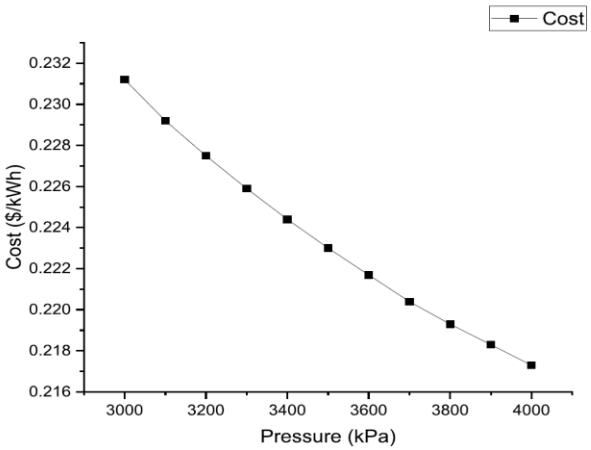

Figure 6. Unit cost of energy vs. turbine pressure

There are two variables, and the system responds differently to changes in each. To analyze their effects, it is crucial to present all outcomes in a single graph. The net work produced by the system was selected as the evaluation criterion, and a graph was created accordingly. This variation is displayed in a three-dimensional graph in Figure 7. The maximum net work was achieved when the mass flow rate approached 42 kg/s, and the turbine inlet pressure reached 4000 kPa.

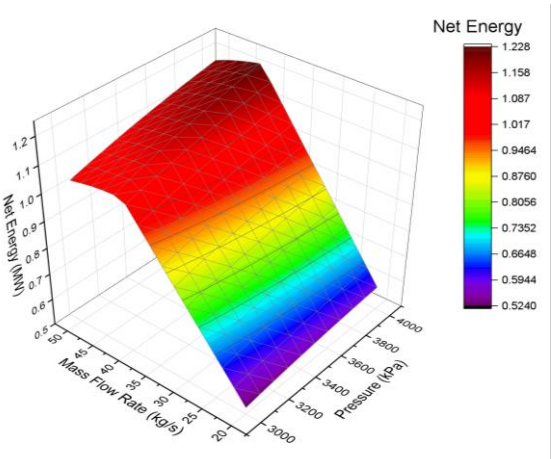

Figure 7. Net energy vs. pressure and mass flow rate

Similarly, the cost function can be represented with two parameters, as shown in Figure 8. The lowest cost is observed at 50 kg/s and 4000 kPa. It is important to note that the parameters minimizing cost differ from those maximizing work output. Therefore, it would be more appropriate to evaluate these values using a multi-objective optimization algorithm.

Additionally, when examining exergy efficiency, it can be observed that it follows a trend parallel to the net work output, as shown in Figure 9. The maximum efficiency was again calculated at 42 kg/s and 4000 kPa. Since the system's sole work output is derived from the ORC, it is logical for these values to align. However, in more complex systems that may be designed in the future, these values could differ.

Finally, the system is optimized, and values generated using a unified objective function are obtained (Figure 10.). These values range between zero and one. The expected optimum point lies between the parameters that directly maximize work output and those that minimize cost.

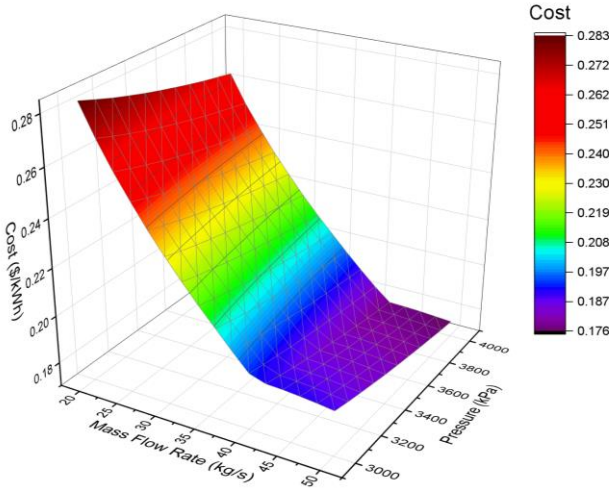

Figure 8. Unit cost vs. pressure and mass flow rate

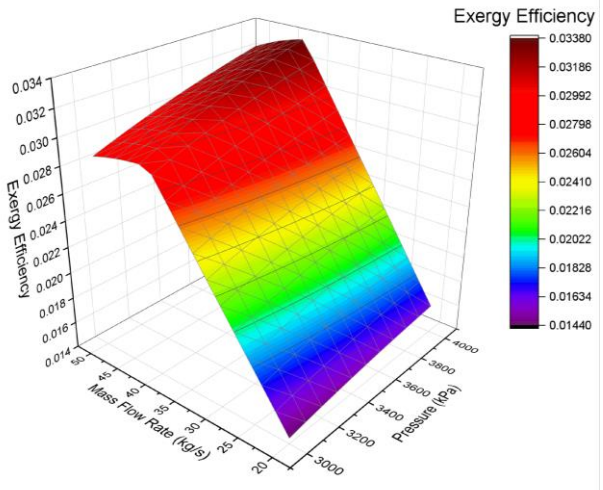

Figure 9. Exergy efficiency vs. pressure and mass flow rate

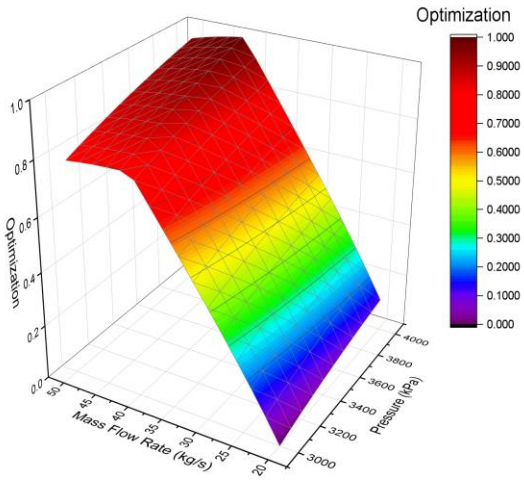

Figure 10. Optimization function vs. pressure and mass flow rate

However, the most accurate result is achieved through weighted and normalized multi-objective optimization. Interestingly, the optimum point aligns with the one that maximizes work output. This is because, upon examining the cost graph independently, although the lowest cost is observed at 50 kg/s, the change beyond 42 kg/s is negligible. Therefore, the optimum point is determined as 42 kg/s and 4000 kPa through the multi-objective optimization algorithm.

The optimum point was compared with the base case scenario used in the initial calculation. In the first calculation, the mass flow rate and pressure were assumed constant at 30 kg/s and 3500 kPa, respectively. Following the optimization, the most optimum values were determined to be 42 kg/s and 4000 kPa. A comparison of these values is presented in Table 2. Additionally, the energy storage capacity of the system was evaluated. The table illustrates the amount of hydrogen produced when the electrolyzer and fuel cell storage are utilized, as well as the amount of energy released when this hydrogen is reconverted into energy. The hydrogen produced can be used for various purposes. These purposes are also shown in Figure 1. These could include industrial facilities or hydrogen-powered vehicles, which are expected to become more widespread in the future. The purpose here is to explain the production cost and quantity of hydrogen from PTC solar energy plant. Hydrogen is an important tool in energy storage and storage is important for renewable sources. Also in this table, the unit energy cost for the optimum case is calculated as 0.1781 $/kWh. This value may be considered high in terms of cost, but it is consistent with the scope of this study, which focuses solely on electricity generation. The energy obtained from solar energy systems is generally more costly compared to other sources. Similar figures have also been found in the literature. In a similar study, Desai and Bandyopadhyay [10] reached a value of 0.188 $/kWh. One way to reduce this value is by transforming the system into a multigeneration system with different aims and functions (such as heating ,cooling etc.).

Table 2. Base case and optimum case results

	Base Case	Optimum Case	Difference	% Change
Solar Irradiation	800 W/m²	800 W/m²	-	-
Area	5000 m²	5000 m²	-	-
High Pressure	3500 kPa	4000 kPa	500 kPa	14.30%
Mass Flow Rate in ORC	30 kg/s	42 kg/s	12 kg/s	40%
Net Energy	0.8443 MW	1.2280 MW	0.3837MW	45.45%
Exergy Efficiency	2.32%	3.37%	1.02	45.45%
Unit Cost of Energy	0.2230 $/kWh	0.1781 $/kWh	0.0449$/kWh	20.13%
Hydrogen Production Rate	0.005023 kg/s	0.007307 kg/s	0.002284	45.45%
Fuel Cell Electric Rate	0.42 MW	0.61 MW	0.19 MW	45.45%

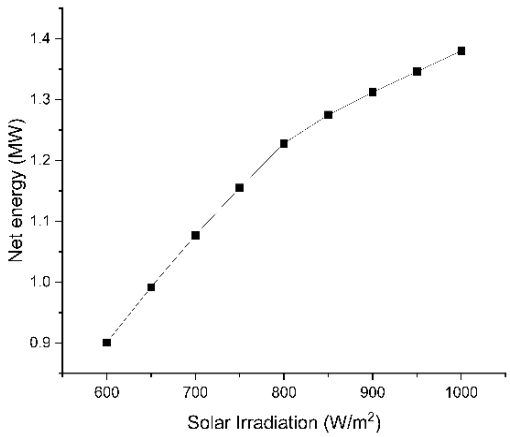

Figure 9. Graph of net energy change with varying solar irradiation

The solar irradiation value fluctuates throughout the day and cannot be controlled or optimized by operators. While a detailed discussion on this topic is beyond the scope of this work, the effect of solar irradiation in the final optimized case is briefly presented as a parametric result to guide researchers. As expected, net energy production increases with the rise in solar irradiation. This increase follows a parabolic curve with diminishing returns, suggesting that not all of the intense solar energy can be utilized efficiently. As the irradiation value increases, temperatures also rise, leading to greater temperature differences and, as a result, higher heat losses.

3. Conclusions

In conclusion, it is crucial to design renewable energy systems that can meet the rapidly growing energy demand. However, it is not enough to simply increase the number of renewable plants; ensuring that they operate efficiently is also essential. Each system has its own dynamics, and it is not feasible to model and optimize all systems using a single equation. The energies entering and exiting the system, along with other variables, significantly impact the results. In this study, two key variables mass flow rate and turbine inlet pressure were altered, and various system outputs were examined. These common outputs were then optimized using a single function. As a result of the optimization, both efficiency and net work increased by approximately 45%, while unit energy cost decreased by about 20%.

Another important point to address is the cost of energy. A value of 0.22 $/kWh, or even 0.18 $/kWh when optimized, is quite high. The reason for the high cost is that the study is designed solely for electricity generation. Additionally, energy efficiency is quite low. Integrating functions such as heating, cooling, and other multigeneration applications would enhance system efficiency. This, in turn, could also lead to a reduction in costs. For example, a portion of the system's waste heat can be used for heating during the winter months. Alternatively, the system can be adjusted to operate more efficiently by integrating with other sources. However, the aim of the current study is to increase the system's efficiency by changing parameters within the system itself, rather than through external interventions. A simple system design has been used to observe the results and confirm the efficiency of the optimization method. Of course, in later stages and future studies, this method can be applied to more complex systems, and additional sources can be integrated into the existing PTC. Energy can also be used for different purposes.

The importance of multi-objective optimization studies in these systems is growing. This study demonstrated that this method is a reliable optimization algorithm that provides useful results. In future research, more complex systems can be optimized, leading to higher efficiencies and lower costs.

Declaration

The author declared no potential conflicts of interest with respect to the research, authorship, and/or publication of this article. The author also declared that this article is original, was prepared in accordance with international publication and research ethics, and ethical committee permission or any special permission is not required.

Author Contributions

Ömer Faruk Güler developed the model, performed calculations, optimized the system and wrote the manuscript.

Nomenclature

A : Area
a : Weight of parameter
An : Annual
C : Cost
CRF : Cost Recovery Factor

D : Diameter
F : Future value
HTF : Heat transfer fluid
h_n : Enthalpy
h : Convection coefficient
I : Solar irradiation
i : Inflation rate
LHV : Lower Heating Value
$\dot{m}$: Mass flow rate
N : Number of collectors
Nu : Nusselt Number
ORC : Organic Rankine cycle
P : Present value
Pr : Prandtl Number
PTC : Parabolic trough collector
Q : Heat
Re : Reynolds Number
SPECO : Specific exergy cost
T : Temperature
$\dot{W}$: Work
Z : Total cost rate
ε : Emittance
σ : Stefan-Boltzman Number
τ : Annual operating time
amb : Ambient
c : Component
co : Cover Outlet
col : Collector
cool : Cooling water
dest : Destruction
e : Exit
eff : Effective
H_2 : Hydrogen
htf : Heat Transfer Fluid
in : Inlet
max : Maximum
min : Minimum
n : Number
out : Outlet
p : Pump
r : Receiver
sky : Sky
tot : Total
turb : Turbine
u : Useful
IC : Investment cost
M : Maintenance

References

1. Teevan, C., Medinilla, A., & Sergejeff, K., The Green Deal in EU foreign and development policy, 2021. ECDPM Briefing Note, p. 131.
2. Gharat, P. V., Bhalekar, S. S., Dalvi, V. H., Panse, S. V., Deshmukh, S. P., & Joshi, J. B., Chronological development of innovations in reflector systems of parabolic trough solar collector (PTC)-A review. Renewable and Sustainable Energy Reviews, 2021. **145**: p. 111002.
3. Ghazouani, M., Bouya, M., & Benaissa, M., Thermo-economic and exergy analysis and optimization of small PTC collectors for solar heat integration in industrial processes. Renewable Energy, 2020. **152**: p. 984-998.
4. Park, J., Kang, S., Kim, S., Cho, H. S., Heo, S., & Lee, J. H., Techno-economic analysis of solar powered green hydrogen system based on multi-objective optimization of economics and productivity. *Energy Conversion and Management*, 2024. **299**: p. 117823.
5. Liu, L., Zhai, R., Xu, Y., Hu, Y., Liu, S., & Yang, L., Comprehensive sustainability assessment and multi-objective optimization of a novel renewable energy driven multi-energy supply system. *Applied Thermal Engineering*, 2024. **236**: p. 121461.
6. Fu, L., Fan, J., Yuanchun, L., Yantao, T., & Yisong, D, Study and application of a constrained multi-objective optimization algorithm. In Proceedings of the IEEE International Vehicle Electronics Conference, 1999. (IVEC'99)(Cat. No. 99EX257) p. 305-307
7. Yilmaz, F., An innovative study on a geothermal based multigeneration plant with transcritical CO2 cycle: Thermodynamic evaluation and multi-objective optimization. *Process Safety and Environmental Protection*, 2024. **185**: p. 127-142.
8. Li, C., & Zhai, R., A novel solar tower assisted pulverized coal power system considering solar energy cascade utilization: Performance analysis and multi-objective optimization. *Renewable Energy*, 2024. **222**:119891.
9. Tian, Y., Cheng, R., Zhang, X., & Jin, Y., PlatEMO: A MATLAB platform for evolutionary multi-objective optimization [educational forum]. IEEE Computational Intelligence Magazine, 2017. **12**(4): p. 73-87.
10. Desai, N. B., & Bandyopadhyay, S., Optimization of concentrating solar thermal power plant based on parabolic trough collector. Journal of Cleaner Production, 2015. **89**: p. 262-271.
11. Babaelahi, M., Mofidipour, E., & Rafat, E., Combined Energy-Exergy-Control (CEEC) analysis and multi-objective optimization of parabolic trough solar collector powered steam power plant. Energy, 2020. **201**: p. 117641.
12. Colakoglu, M., & Durmayaz, A., Energy, exergy and environmental-based design and multiobjective optimization of a novel solar-driven multi-generation system. Energy Conversion and Management, 2021. **227**: p. 113603.
13. Georgousis, N., Lykas, P., Bellos, E., & Tzivanidis, C., Multi-objective optimization of a solar-driven polygeneration system based on CO2 working fluid. Energy Conversion and Management, 2022. **252**: p. 115136.
14. Modabber, H. V., & Manesh, M. H. K., Optimal exergetic, exergoeconomic and exergoenvironmental design of polygeneration system based on gas Turbine-Absorption Chiller-Solar parabolic trough collector units integrated with multi-effect desalination-thermal vapor compressor-reverse osmosis desalination systems. Renewable Energy, 2021. **165**: p. 533-552.
15. Esfahani, M. N., Aghdam, A. H., & Refahi, A., Energy, exergy, exergoeconomic, exergoenvironmental (4E) assesment, sensitivity analysis and multi-objective optimization of a PTC–tehran climate data case study. Journal of Cleaner Production, 2023. **415**: p. 137821.
16. Adun, H., Adedeji, M., Adebayo, V., Shefik, A., Bamisile, O., Kavaz, D., & Dagbasi, M., Multi-objective optimization and energy/exergy analysis of a ternary nanofluid based parabolic trough solar collector integrated with kalina cycle. *Solar Energy Materials and Solar Cells*, 2021. ***231***: p. 111322.

17. Hocaoglu, F. O., & Serttas, F., A novel hybrid (Mycielski-Markov) model for hourly solar radiation forecasting. Renewable Energy, 2017. **108**: p. 635-643.
18. Guler, O. F., Sen, O., Yilmaz, C., & Kanoglu, M., Performance evaluation of a geothermal and solar-based multigeneration system and comparison with alternative case studies: Energy, exergy, and exergoeconomic aspects. Renewable Energy, 2022. **200**: p. 1517-1532.
19. Bellos, E., & Tzivanidis, C., A detailed exergetic analysis of parabolic trough collectors. *Energy Conversion and Management*, 2017. ***149***: p. 275-292.
20. Behar, O., Khellaf, A., & Mohammedi, K., A novel parabolic trough solar collector model–Validation with experimental data and comparison to Engineering Equation Solver (EES). *Energy Conversion and Management*, 2015. ***106***: p 268-281.
21. Ferraro, V., Imineo, F., & Marinelli, V., An improved model to evaluate thermodynamic solar plants with cylindrical parabolic collectors and air turbine engines in open Joule–Brayton cycle. *Energy*, 2013. ***53***: p. 323-331.
22. Swinbank, W. C., Long-wave radiation from clear skies. *Quarterly Journal of the Royal Meteorological Society*, 2013. **89**(381): p. 339-348.
23. Kakaç, S., Liu, H., & Pramuanjaroenkij, A., *Heat exchangers: selection, rating, and thermal design*. CRC press, 2012. p. 81-128
24. Bellos, E., Tzivanidis, C., & Antonopoulos, K. A., A detailed working fluid investigation for solar parabolic trough collectors. *Applied Thermal Engineering*, 2017. ***114***: p. 374-386.
25. Sen, O., Guler, O. F., Yilmaz, C., & Kanoglu, M., Thermodynamic modeling and analysis of a solar and geothermal assisted multi-generation energy system. Energy Conversion and Management, 2021. **239**: p. 114186.
26. Bejan, A., Tsatsaronis, G., & Moran, M. J., *Thermal design and optimization*. 1995, USA: John Wiley & Sons.
27. Miri, M., Tolj, I., & Barbir, F., Review of Proton Exchange Membrane Fuel Cell-Powered Systems for Stationary Applications Using Renewable Energy Sources. *Energies*, 2024. **17**(15): p. 3814.
28. Alkhaldi, S. A., & Prasad, A. K., Strategies for gas management in the PEM water electrolyzer anode. *Journal of Power Sources*, 2025. **626**: p. 235747.
29. Astriani, Y., Tushar, W., & Nadarajah, M., Optimal planning of renewable energy park for green hydrogen production using detailed cost and efficiency curves of PEM electrolyzer. *International Journal of Hydrogen Energy*, 2024. **79**: p. 1331-1346.
30. Larminie, J., & Dicks, A., *Fuel cell systems explained* (2nd ed.). 2003, England: John Wiley & Sons.
31. Yılmaz, C., Cengiz, E., & Kahraman, H. T., A new evolutionary optimization algorithm with hybrid guidance mechanism for truck-multi drone delivery system. Expert Systems with Applications, 2024. **245**: p. 123115.
32. Şeker, M., Mutlu, İ., Aysal, F. E., Atli, I. S., Yavuz, I., & Ergün, Y. A., The ANN analysis and Taguchi method optimisation of the brake pad composition. *Emerging Materials Research*, 2021. **10**(3): p. 314-320.
33. Li, L., Liu, P., Li, Z., & Wang, X., A multi-objective optimization approach for selection of energy storage systems. Computers & Chemical Engineering, 2018. **115**: p. 213-225.

Available online at www.dergipark.org.tr/en

INTERNATIONAL ADVANCED RESEARCHES and ENGINEERING JOURNAL

Journal homepage: www.dergipark.org.tr/en/pub/iarej

e-ISSN: 2618-575X

International Open Access

Volume 09
Issue 01

April, 2025

Research Article

Thermodynamic and technoeconomic feasibility assessment on liquefaction of CO_2 by-product of Afyon biogas power plant

Muhammed Arslan*, [a]

[a] *Afyon Kocatepe University, Çay Vocational High School, Afyon, 03700, Turkey*

ARTICLE INFO

Article history:
Received 02 October 2024
Accepted 16 February 2025
Published 23 April 2025

Keywords:
Biogas
CO_2 liquefaction
Thermodynamic analysis
Technoeconomic analysis.

ABSTRACT

The composition of the biogas produced in Afyon biogas power plant is approximately as follows: 55% CH_4 (methane) - 40% CO_2 (carbon dioxide)- 4.5% H_2O (water) and trace amounts of other components. The methane produced is used in gas engines to generate electricity. Carbon dioxide, however, increases greenhouse gas emissions when released into the atmosphere. The model designed in this study includes the liquefaction and storage of CO_2 and the technoeconomic analysis of this process. The analysis was performed in the Aspen Plus software, which is widely used in the analysis of complex processes involving numerious chemical reactions. According to the results of the thermodynamic analysis, the energy efficiency, exergy efficiency, net electrical power and liquid CO_2 production rate of the plant were determined as 14.92%, 13.08%, 4,000 kW and 99 kg/h, respectively. According to the results of the technoeconomic analysis, unit electricity cost, liquid CO_2 flow cost and TCC (total capital cost) are 77.5 $/MWh, 993.68 $/h and 47,548,200 $ respectively. The designed model has the potential to prevent the release of CO_2 into the atmosphere at reasonable prices.

1. Introduction

With the depletion of fossil fuels and the acceleration of climate change, the need for and opportunities in renewable energy are increasing. Biomass-based energy is becoming an important way to generate sustainable power, reduce greenhouse gas emissions, improve energy security, contribute to development, increase the use of green energy and alleviate dependence on limited resources [1-3]. Anaerobic digestion technology, a widely used method for utilizing biomass energy, is recognized as highly effective and promising. The anaerobic digestion process, which involves a series of biochemical reactions, results in biogas production [1, 4, 5].

Biogas from anaerobic digestion of organic waste is a renewable energy source with great potential to reduce global dependence on fossil fuels. As an environmentally friendly and sustainable energy source, biogas can be used for heat and electricity generation. Moreover, the digestion product can be used to produce fertilizers [6, 7].

On the other hand, societies today face severe weather events, rising sea levels and natural disasters. An important cause of these problems is carbon emissions that cause greenhouse gases and these emissions need to be reduced [8]. One of the important components of biogas in the biogas production process is carbon dioxide, which constitutes about 40% of the gas. Releasing carbon dioxide into the atmosphere, whether directly from gas engines or after separation from methane, significantly contributes to greenhouse gas emissions. However, liquefaction and storage of carbon dioxide after separation from methane can solve this problem. Such biogas separation is also necessary for the utilization of carbon dioxide, a valuable molecule in the food and beverage industries, chemical synthesis and greenhouses and other industrial activities [6].

Many studies on electricity generation from biogas and carbon dioxide liquefaction have been conducted in the literature and some of them are summarized below.

Rostamzadeh et al. (2018) proposed a hybrid model powered by biogas and geothermal energy source and analyzed the model thermodynamically. According to the results of the analysis, the model has 62.28% thermal efficiency and 74.9% exergy efficiency and generates 443.4 kW of electricity [9].

Sun et al. (2024) proposed a multigeneration system for heating, cooling, clean water and power generation and

* Corresponding author. Tel.: +0 272 218 35 35
E-mail addresses: muarslan@aku.edu.tr *(M.Arslan)*
ORCID: 0000-0001-8387-7008 *(M.Arslan)*
DOI: 10.35860/iarej.1560048

analyzed the system from thermodynamic and thermoeconomic perspectives. According to the thermodynamic analysis results, the multigeneration system has 58.06% energy efficiency, 36% exergy efficiency and 9,775.5 kW electrical power generation capacity. According to the results of the thermoeconomic analysis, the multigeneration system has 59,536 k$ total equipment cost and 29 $/MWh levelized cost of products [10].

Zhao et al. (2024) developed a hybrid model that efficiently utilizes exhaust gas (after turbine) from biogas combustion and flue gas from silicon production and analyzed the model from thermodynamic and economic perspectives. According to the results of the thermodynamic analysis, the model has an energy efficiency of 43.61%, an exergy efficiency of 51.07% and an annual power generation capacity of 293 GWh. According to the economic analysis results, the initial investment requirement, dynamic payback period and net present value are 50,132.47 k$, 4.09 and 136,864.14 k$, respectively [11].

Cao et al. (2022) modeled a cogeneration system generating electrical and cooling power and analyzed the system from a thermodynamic point of view by optimizing. The analysis revealed that the system has an electricity generation capacity of 1,140 kW, an energy efficiency of 57.11%, and an exergy efficiency of 36.68% [12].

Gholizadeh et al. (2019) modeled a biogas-fired gas turbine assisted by an ORC (Organic Rankine Cycle) and a modified-ORC, and analyzed the model from thermodynamic and thermoeconomic aspects. According to the results of the analysis, the energy efficiency, exergy efficiency, power generated and average product cost of the gas turbine assisted by modified-ORC are calculated as 41.83%, 38.91%, 1,368 kW and $17.2/GJ, respectively [13].

Ghorbani et al. (2021) developed an integrated system for liquid bio-CO_2 production by cryogenic separation, CO_2 capture and liquefaction and evaluated the system from thermodynamic and thermoeconomic perspectives. According to the evaluation results, 0.2102 kg/h liquid bio-CO_2 production, 73.11% thermal efficiency and 72.58% exergy efficiency were obtained [14].

Jung et al. (2021) conducted a technoeconomic analysis of four different CCL (carbon dioxide compression and liquefaction) processes with high purity and recovery using a distillation column. As a result of the analysis, the cost of CO_2 liquefaction with 99.9% purity and 93% recovery at 80 bar pressure was 22 $/$CO_2$ [15].

Yousef et al. (2017) proposed a model to separate carbon dioxide from methane at low temperatures for biogas upgrading with HYSYS software. The model liquefies CO2 at 110 bar pressure and 99.9% purity, increasing the methane purity from 60% to 97.1% by mol. [16].

Øi et al. (2016) developed different models for liquefaction of 1 million tons of CO_2 per year with HYSYS software. The models are focused on two points as external refrigeration and integrated refrigeration. According to the analysis results, the model with the optimum cost is the one based on external refrigeration and has an 23 M€ investment and an operating cost of 4 M€/ton [17].

Liu et al. (2024) designed four different models on CO_2 liquefaction and storage and analyzed the models from thermodynamic and economic perspectives. According to the thermodynamic analysis results, the best model has 71.54% round-trip efficiency and 40.61 kWh/m^3 energy density, and 37.86 kg/s CO_2 is liquefied. According to the thermoeconomic analysis results, levelized cost of electricity and net present value are 110.9 $/MWh and 3.03 M$, respectively [18].

Khosravi et al. (2023) modeled a cogeneration system that produces electrical power, CO_2 liquefaction, solid waste gasification and steam production and analyzed the system from thermodynamic and thermoeconomic perspectives. According to the thermodynamic analysis results, the system has 11.9% electrical energy efficiency, 19.48 MW electrical power capacity and 1.9 CO_2 liquefaction-COP (coefficient of performance). According to the thermoeconomic analysis results, the electricity cost was determined as 60.1 $/MWh [19].

In this study, biogas produced in Afyon biogas power plant is purified from carbon dioxide and other undesired components before being sent to gas engines. While electricity is generated from pure methane in the engines, carbon dioxide is sent to the cooling unit for liquefaction. In this way, 95% of the biogas is utilized, and carbon dioxide emissions to the atmosphere are prevented. In addition, electricity and liquid carbon dioxide can be used to meet many needs. The model proposed in this study represents the process from biomass digestion to electricity and liquid carbon dioxide production. It is designed using Aspen Plus software and analyzed from thermodynamic and technoeconomic point of view. The originality of this study lies in the technoeconomic analysis of the process from the release to the liquefaction of by-product carbon dioxide, conducted using Aspen Plus software. Aspen Plus is a complex software that realistically simulates physical and chemical processes while incorporating up-to-date economic data. A realistic analysis of such a process using Aspen Plus has not been encountered in the literature. Figure 1 illustrates the Afyon biogas power plant.

Figure 1. Afyon Biogas Power Plant [20].

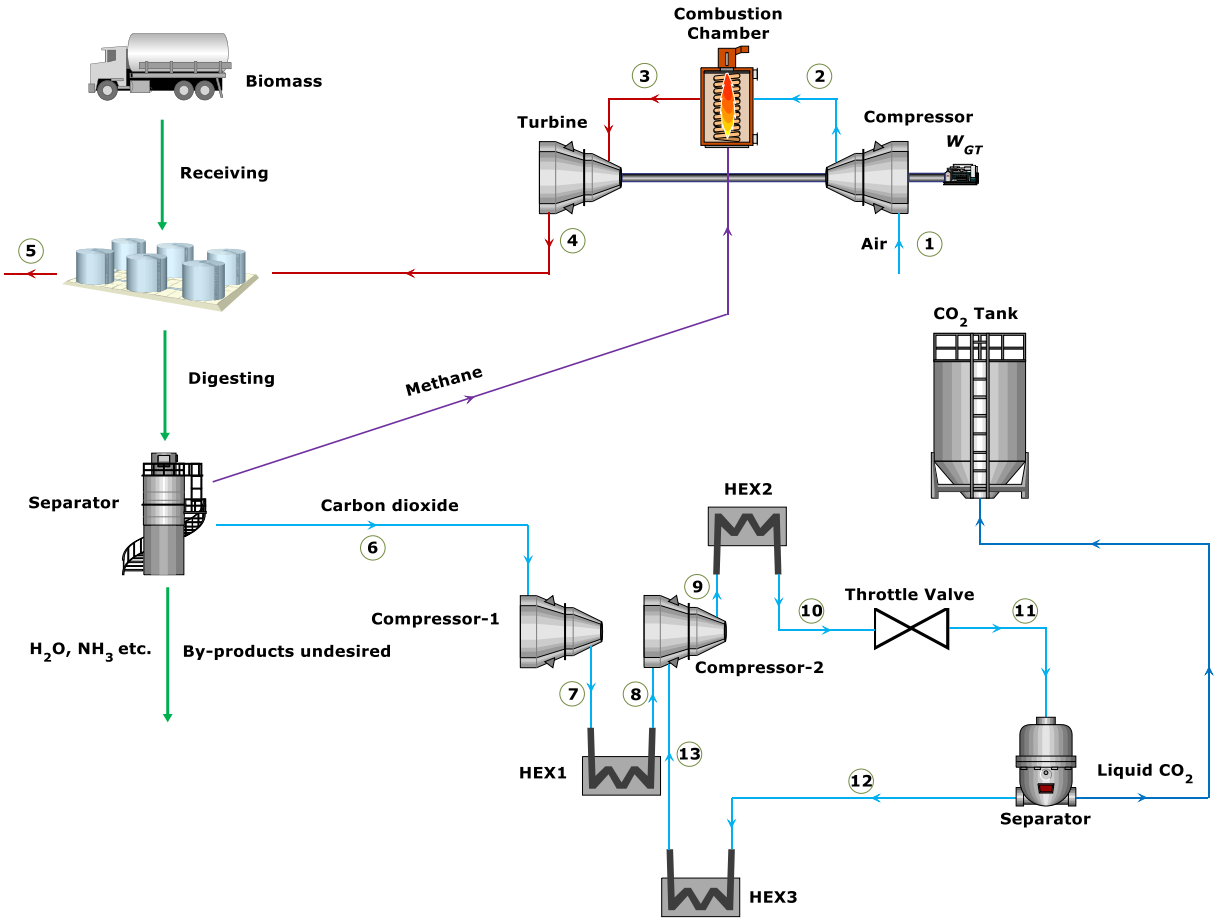

Figure 2. The operation flow of designed model.

In Fig. 2, the operation flow of the designed model is shown. Biogas is produced in the reactor and methane, carbon dioxide and other components are separated from each other. Methane is then sent to the combustion chamber. The exhaust gas, exiting the turbine, is sent to the reactor to increase reactor's temperature and is then released into the atmosphere. Meanwhile, carbon dioxide is liquefied using the Linde-Hampson process.

2. Analysis and Aspen Plus

This section presents the methodology of the study, including the main equations and the software used for the analysis.

2.1 Analysis

The analysis consists of two steps: thermodynamic and technoeconomic analysis. The first step is thermodynamic analysis and the designed model is analyzed in terms of energy and exergy at both equipment and plant levels. In this

way, the thermodynamic performance and flow data of the plant and equipment can be measured. The exergy data obtained from the thermodynamic analysis, along with the economic data, form the basis of the technoeconomic analysis. The logic of the technoeconomic analysis is to assign costs to each flow in the process using various up-to-date data such as equipment purchase costs, interest rate, capital recovery factor, operation and maintenance factor. In this way, product costs and total capital cost can be calculated. The main equations used in the analysis are as follows:

The net power of the power plant is the difference between the power produced in the turbine and the power consumed by the compressor.

$$\dot{W}_{net\ electricity} = \dot{W}_{Turbine} - \dot{W}_{Compressor} \quad (1)$$

The energy efficiency is the ratio of the net power produced by the plant to the fuel power entering the plant.

$$\eta_{energy} = \frac{W_{net\ electricity}}{\dot{m}_{methane} \cdot HV_{methane}} \quad (2)$$

The exergy efficiency is the ratio of the net power produced by the plant to the fuel exergy entering the plant.

$$\eta_{exergy} = \frac{\dot{W}_{net\ electricity}}{\dot{m}_{methane} \cdot ex^{ch}_{methane}} \quad (3)$$

The exergy cost rate is calculated by multiplying the unit flow cost rate by the flow exergy. *k* represents flow number.

$$\dot{C}_k = c_k . \dot{E}_k \quad (4)$$

The cost balance for an equipment with power and heat inputs and outputs is expressed as follows. $\dot{Z}_k$ and subscripts *q, w, i and o* represent total cost rate, heat, power, input and output, respectively.

$$\sum_i \dot{C}_{i,k} + \dot{C}_q + \dot{Z}_k = \sum_o \dot{C}_{o,k} + \dot{C_W} \quad (5)$$

2.2 Aspen Plus

Aspen Plus is a software that is very well known for chemical processes and presents the most realistic results in a simple way. Designers can design complex models with Aspen Plus and simulate by solving them with mathematical methods. They can also make designed models better. It can instantly display thermodynamic data (pressure, temperature, mass flow rate, vapor fraction, heat/work etc.) for each flow and show areas open to development. It evaluates chemical and physical events in processes with thermodynamic laws and equations. If there is a thermodynamically impossible situation in the designed model, the error is explained to the designer by Aspen Plus. In addition, all equations required for economic and technoeconomic analysis are available in the Aspen Plus database. Aspen Plus automatically selects the equipment that is most suitable for thermodynamic conditions in a designed model by sizing and includes that equipment in the economic analysis. Therefore, there is no need for manual sizing and costing. For example, when the air flow rate entering a compressor in the current design is changed, Aspen Plus assigns a new compressor suitable for the current conditions instead of the current compressor and the economic data changes. When the economic analysis tab is activated, data such as total capital cost, equipment purchase cost, installed cost, unit flow cost are displayed [21].

Since this study involves biogas production from biomass, combustion of methane and liquefaction of carbon dioxide, thermodynamic analysis and technoeconomic analysis, Aspen Plus is an indispensable software for the study.

3. Numerical Results

Figure 3 shows the model designed in Aspen Plus. The process starts with anaerobic digestion of biomass in the reactor and as a result of gasification, 3523 kg/h of biogas is released at 308 K temperature and 101 kPa pressure. Methane, carbon dioxide and other unwanted components are separated in the biocleaner unit. Methane is sent to the combustion chamber and reacts with compressed air supplied by compressor. The exhaust gas generated from combustion drives the turbine. The 10,800 kW power required by the compressor is met by the 14,800 kW power produced by the turbine. Thus, the net electrical power is 4,000 kW. The exhaust gas exiting the turbine heats the reactor before being released into the atmosphere to increase the reactor temperature. On the other hand, the separated carbon dioxide is liquefied and stored instead of being released into the atmosphere. With the Linde Hampson process, carbon dioxide is compressed and cooled in two stages in the compressor. Finally, liquid carbon dioxide is separated from gaseous carbon dioxide by throttling in the throttle valve. The gaseous form of carbon dioxide is recirculated to the second compressor. In this way, 99 kg/h of liquid carbon dioxide at 253 K and 1970 kPa is obtained.

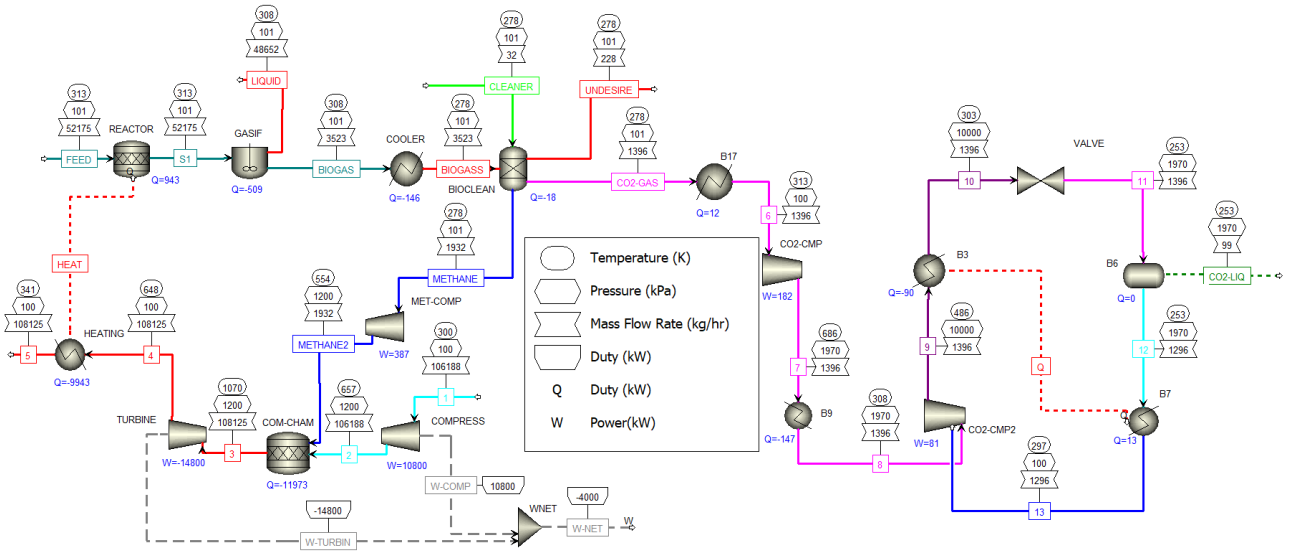

Figure 3. The designed model in Aspen Plus.

Table 1. The thermodynamic analysis results of the designed model.

	Value
Produced methane	1932 kg/h
η_{energy}	14.92%
η_{exergy}	13.08%
Net electrical power	4,000 kW
Produced liquid CO_2	99 kg/h

The technoeconomic analysis results of the model are given in Table 2.

Table 2. The technoeconomic analysis results of the designed model.

	Value
The unit cost of electricity	77.5 $/MWh
The cost of liquid CO_2	10.1 $/kg
The flow cost of liquid CO_2	993.68 $/h
Total installed cost	37,156,100 $
TCC	47,548,200 $

The thermodynamic analysis results of the model are given in Table 1.

4. Conclusions

In this study, a model representing the process of electricity production and liquefaction of by-product carbon dioxide in Afyon biogas power plant was developed. Carbon dioxide released to the atmosphere in the existing plant is liquefied and stored with the designed model. This has a positive impact on reducing greenhouse gas emissions. The liquid carbon dioxide obtained can be used for various purposes such as food and beverage production, chemical production, welding and metal fabrication, fire extinguishers, medical applications, and environmental applications. In this way, approximately 95% of the biogas produced from biomass in the plant is utilized effectively. The key numerical results of the study are as follows:

- The plant produces 4,000 kW net electrical power and 99 kg/h liquid CO_2.
- The energy and exergy efficiency of the plant are 14.92% and 13.08%, respectively.
- The unit cost of the produced electricity and the flow cost of carbon dioxide are 77.5 $/MWh and 993.68 $/h, respectively.
- TCC is 47,548,200 $.

The proposals of the study are as follows:

- Thermodynamic optimization of the plant will increase energy and exergy efficiency and therefore reduce electricity cost.
- The equipment involved in the liquefaction process of carbon dioxide operates with the electricity produced by the plant. Therefore, reducing the cost of electricity produced in the plant will reduce the flow cost of liquid carbon dioxide.
- The type and amount of raw material used in biogas production and the reactor temperature determine the composition of the biogas. These key parameters should be investigated to improve methane production efficiency.
- Other components released during the production of biogas can be utilized beneficially, and technoeconomic analysis should be conducted on this matter.
- To improve the process from a technoeconomic perspective, studies can be carried out on the liquefaction of CO_2 using different thermodynamic cycles.
- The effects of the analysis on emission values can be investigated.
- A more comprehensive technoeconomic analysis can be conducted to see the effects of different operating conditions and costs.

Declaration

The author declared no potential conflicts of interest with respect to the research, authorship, and/or publication of this article. The author also declared that this article is original, was prepared in accordance with international publication and research ethics, and ethical committee permission or any special permission is not required.

Nomenclature

CCL	Carbon dioxide compression and liquefaction
CH_4	Methane
CO_2	Carbon dioxide
COP	Coefficient of performance
H_2O	Water
ORC	Organic Rankine Cycle
TCC	Total capital cost ($)
HV	Heating Value (kJ/kg)
$\dot{E}$	Exergy (kW)
c	Unit flow cost rate ($/kWh)
$\dot{C}$	Exergy cost rate ($/h)
ex^{ch}	Chemical exergy (kJ/kg)
η	Efficiency
$\dot{m}$	Mass flow rate (kg/s)
$\dot{W}$	Power (kW)
$\dot{Z}_k$	Total cost rate ($/h)

References

1. Prasad, R. K., A. Sharma, P. B. Mazumder, and A. Dhussa, *A comprehensive pre-treatment strategy evaluation of ligno-hemicellulosic biomass to enhance biogas potential in the anaerobic digestion process*. RCS Sustainability, 2024. **2**: p. 2444-2467.
2. Tjutju, N. A. S., J. Ammenberg, and A. Lindfors, *Biogas potential studies: A review of their scope, approach, and relevance*. Renewable and Sustainable Energy Reviews, 2024. **201**: p. 114631.
3. Aigbe, U. O., K. E. Ukhurebor, A. O. Osibote, M. A. Hassaan, and A. E. Nemr, *Optimization and prediction of biogas yield from pretreated Ulva Intestinalis Linnaeus applying statistical-based regression approach and machine learning algorithms*. Renewable Energy, 2024. **235**: p. 121347.
4. Joshi, J., P. Bhatt, P. Kandel, M. Khadka, S. Kathariya, S. Thapa, S. Jha, S. Phaiju, S. Bajracharya, and A. P. Yadav, *Integrating microbial electrochemical cell in anaerobic digestion of vegetable wastes to enhance biogas production*. Bioresource Technology Reports, 2024. **27**: p. 101940.
5. Shen, R., P. Sun, J. Liu, J. Luo, Z. Yao, R. Zhang, J. Yu, and L. Zhao, *Robust prediction for characteristics of digestion products in an industrial-scale biogas project via typical non-time series and time-series machine learning algorithms*. Chemical Engineering Journal, 2024. **498**: p. 155582.
6. Rodero, M. D. R., R. Muñoz, A. G. Sánchez, H. A. Ruiz, and G. Quijano, *Membrane materials for biogas purification and upgrading: Fundamentals, recent advances and challenges*. Journal of Environmental Chemical Engineering, 2024. Available online 14 September 2024, p. 114106.
7. Alharbi, R. M., *Anaerobic co-digestion of cow manure and microalgae to increase biogas production: A sustainable bioenergy source*. Journal of King Saud University-Science, 2024. **36**(9): p. 103380.
8. Ma, C., H. Yu, G. Monticone, S. Ma, J. V. Herle, and L. Wang, *Techno-economic evaluation of biogas-fed SOFC systems with novel biogas purification and carbon capture technologies*. Renewable Energy, 2024. **235**: p. 121302.
9. Rostamzadeh, H., S. G. Gargari, A. S. Namin, and H. Ghaebi, *A novel multigeneration system driven by a hybrid biogas-geothermal heat source, Part I: Thermodynamic modeling*. Energy Conversion and Management, 2018. **177**: p. 535–562.
10. Sun, K., W. Zhang, R. Li, D. Liu, X. Gao, H. Song, X. Chen, and L. Zhou, *Thermodynamic feasibility evaluation of an innovative multigeneration system using biogas dry reforming integrated with a CCHP-desalination process*. Desalination, 2024. **580**: p. 117526.
11. Zhao, X., H. Chen, J. Li, P. Pan, F. Gui, and G. Xu, *Thermodynamic and economic analysis of a novel design for combined waste heat recovery of biogas power generation and silicon production*. Energy, 2024. **290**: p. 130272.
12. Cao, Y., H. A. Dhahad, H. M. Hussen, and T. Parikhani, *Proposal and evaluation of two innovative combined gas turbine and ejector refrigeration cycles fueled by biogas: Thermodynamic and optimization analysis*. Renewable Energy, 2022. **181**: p. 749-764.
13. Gholizadeh, T., M. Vajdi, and F. Mohammadkhani, *Thermodynamic and thermoeconomic analysis of basic and modified power generation systems fueled by biogas*. Energy Conversion and Management, 2019. **181**: p. 463–475.
14. Ghorbani, B., A. Ebrahimi, and M. Ziabasharhagh, *Thermodynamic and economic evaluation of biomethane and carbon dioxide liquefaction process in a hybridized system of biogas upgrading process and mixed fluid cascade liquefaction cycle*. Process Safety and Environmental Protection, 2021. **151**: p. 222–243.
15. Jung, P. G., S. Kim, Y. I. Lim, H. Kim, and H. M. Moon, *Techno-economic comparisons of CO_2 compression and liquefaction processes with distillation columns for high purity and recovery*. International Journal of Greenhouse Gas Control, 2024. **134**: p. 104113.
16. Yousef, A. M., Y. A. Eldrainy, W. M. El-Maghlany, and A. Attia, *Biogas upgrading process via low-temperature CO_2 liquefaction and separation*. Journal of Natural Gas Science and Engineering, 2017. **45**: p. 812-824.
17. Øi, L. E., N. Eldrup, U. Adhikari, M. H. Bentsen, J. L. Badalge, and S. Yang, *Simulation and cost comparison of CO_2 liquefaction*. Energy Procedia, 2016. **86**: p. 500–510.
18. Liu, Z. X. Yan, S. Wang, X. Wei, Y. Zhang, J. Ding, and C. Su, *Performance of compressed CO_2 energy storage systems with different liquefaction and storage scenarios*. Fuel, 2024. **359**: p. 130527.
19. Khosravi, S., R. K. Saray, E. Neshat, and A.

Arabkoohsar, *Towards an environmentally friendly power and hydrogen co-generation system: Integration of solar-based sorption enhanced gasification with in-situ CO_2 capture and liquefaction process*. Chemosphere, 2023. **343**: p. 140226.

20. Afyon Energy, [access date 09.15.2024], https://afyonenerji.com.tr/
21. Aspen Plus, *Engineering Analysis Database*. 2024.

Available online at www.dergipark.org.tr/en

INTERNATIONAL ADVANCED RESEARCHES and ENGINEERING JOURNAL

Journal homepage: www.dergipark.org.tr/en/pub/iarej

e-ISSN: 2618-575X

International Open Access

Volume 09
Issue 01

April, 2025

Research Article

An investigation into the effect of temperature on the performance of magnetorheological fluid dampers

Muaz Kemerli*, [a]

[a]*Department of Mechanical Engineering, Faculty of Engineering, Sakarya University, 54050, Turkiye.*

ARTICLE INFO

Article history:
Received 11 November 2024
Accepted 21 April 2025
Published 23 April 2025

Keywords:
Bingham plastic model
Frequency
Heating
Magnetorheological damper
Magnetorheological fluid
MR damper
MR fluid
Temperature

ABSTRACT

Magnetorheological (MR) dampers are semi-actively controlled smart damping devices. MR dampers have been the focus of intense research for the past few decades and have been used in various practical applications. Many studies have been conducted on control applications of MR dampers along with dynamic, numerical, and analytical models for predicting the force response. Nevertheless, many problems still limit the widespread use of MR dampers. One of these challenges is the performance loss due to the elevated temperatures inside the MR damper body, which is induced by viscous heating and electrical resistance. This is a common problem for many types of MR dampers, reducing the performance of the control algorithms. Thus, it is important to predict the effect of the temperature on the force response under different conditions. In this study, an experimental test setup was used to monitor the effect of the temperature on the performance of a commercial LORD RD-8041-1MR damper. Experiments were conducted under different current and frequency settings. The results showed that the force loss due to the temperature difference could reach up to 50% at the highest frequency and lowest current condition. According to the results, both current and frequency play a critical role in predicting the force loss, as they significantly influence the damper's sensitivity to temperature changes.

1. Introduction

Magnetorheological (MR) fluid and MR dampers have recently become an attractive research area in engineering. The invention of MR fluid goes back to the 1940s [20]. After the 1980s, studies started to gain pace. Many theoretical models [10, 13, 18] are presented, and different MR devices have been proposed until now, such as clutches [14], bearings [4], brakes [15] and dampers. However, with the widespread usage of MR dampers, different problems are encountered, such as sedimentation [27], agglomeration [24], leakage, and viscosity drop of the MR fluid by temperature [29]. These problems restrict the performance of MR dampers. While sedimentation, agglomeration, and leakage affect the performance of the MR damper over the long term, the performance loss due to the temperature increase is present as long as the MR damper is in operation [9]. Temperature also plays a role in increasing these problems, particularly by promoting sedimentation [11]. Another issue is that the presence of such defects makes the damper's performance more sensitive to temperature increases [28].

In practical use, MR dampers need an appropriate controller for practical applications. However, the response generated by the controller cannot predict the correct signal due to the performance loss of the MR damper caused by the temperature increase [1]. Therefore, it is a critical issue to be considered in the design and control of MR dampers.

The structure of an MR damper is shown in Figure 1. Two heat sources are present in MR dampers; the viscous dissipation during the damping of the vibration and the electrical resistance in the coil inside the MR damper [9]. The heat generated by the viscous dissipation is distributed within the MR fluid by the motion of the piston. However, the removal of this heat from the damper body to the surrounding air is limited, as it primarily relies on natural convection.

On the other hand, the heat generated by the coil also contributes significantly to the temperature rise. Unlike viscous heating, this heat cannot be effectively distributed throughout the MR fluid. Since the coil is typically embedded within the piston head, it further limits heat

* Corresponding author. Tel: +90 264 295 7077.
E-mail addresses: mkemerli@sakarya.edu.tr
ORCID: 0000-0001-5643-8835 *(Muaz Kemerli)*
DOI: 10.35860/iarej.1583116

dissipation from the outer cylinder of the MR damper to the surrounding air. Besides, as the required resistance force increases, the required current increases, accompanied by a larger viscous dissipation, eventually leading to cumulative heat generation. A substantial temperature rise can occur within a few minutes of operation under elevated current levels [9]. As a result of the rise in temperature, the viscosity decreases, which can dramatically affect the performance of the MR damper.

In early studies, the effect of temperature on the viscosity of the MR fluid has been clearly demonstrated [30]. Batterbee and Sims reported a viscosity drop of 34% with a yield stress drop down to 22% with a range between 15°C to 75°C [1]. Conversely, the operation of MR fluid at low temperatures also changes the damping force of MR damper. For instance, at -40°C and 3 A of applied current, the damping force was observed to increase by 219.2% [16]. That said, the influence of temperature remains an active topic of discussion as it is used across various applications [22]. The effects of temperature on MR damper performance are well presented in McKee's work [17], and these effects are also evident across different operational modes of MR fluids [8]. Different studies have also investigated transient heat transfer in the MR damper [9]. It has been shown that within 5 minutes of operation, the viscosity of MR fluid decreases, resulting in a reduction of the damper's resistance force. This change in the resistance force significantly affects the controller's efficiency [1]. To address this issue, a temperature compensation method for controlling the damping force of MR dampers is proposed as a patent [23]. Additional control strategies are offered to better assess the temperature-induced performance variations [1, 16, 26]. Some studies also suggest adapting existing models such as the Bouc-Wen model or developing new dynamic models that explicitly account for temperature effects [21, 25].

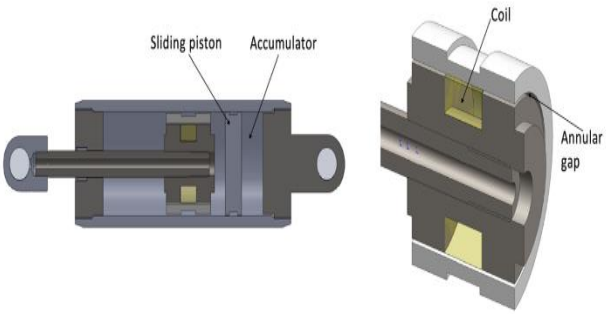

Figure 1. Schematic view of the MR damper [19]

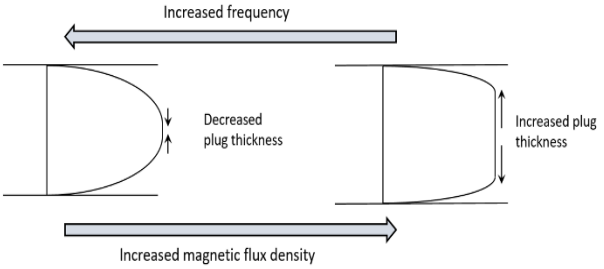

Figure 2. The plug formation inside the annular gap of the MR damper

In a recent study by Delijani et. al. [5], a force loss of up to 14% was calculated at 1 A current within a frequency range of 2–4 Hz. Another study reported a 22% reduction in maximum force and a corresponding 26% decrease in energy dissipation at 1 A and 3 Hz, caused by a temperature difference of just 10°C [2]. Similarly, it was found that even a 7°C increase could lead to a 20% reduction in energy dissipation [3]. Between 20°C and 40°C, a 20% decrease in maximum force was also observed in another study [7]. At elevated temperatures as high as 125°C from the ambient temperature, force losses were reported to reach up to 66.32% [12]. These results vary significantly depending on factors such as excitation frequency, MR damper type, and applied current. Therefore, each study must be evaluated independently, and only a general assessment can be made across literature.

The frequency is another parameter that affects the performance of the MR damper, and the effect of frequency on the temperature increase is pointed out in later studies [2]. However, to the authors' knowledge, no study directly focused on the frequency and current effect on the force loss due to the temperature increase. These effects are of paramount importance when designing a control algorithm to deal with these shortcomings.

In this study, the MR damper's force loss regarding the applied current and frequency is investigated, and the underlying reasons are discussed. It is shown that these two parameters have a key role in prediction of the force loss due to the temperature rise.

2. Problem Definition and the Experimental Setup

MR fluid flow in MR dampers is mainly considered the valve mode of the MR fluid flow [24]. Valve mode expresses that the MR fluid flows through a channel driven by a pressure gradient, which is created by the motion of the MR damper. The apparent viscosity of the MR fluid is generally expressed by the Bingham plastic fluid model in valve mode. Regarding the Bingham plastic fluid model, the shear stress can be expressed in Eq. (1) as:

$$\tau = \tau_y + \mu\dot{\gamma} \quad (1)$$

where τ is the shear stress, τ_y is the yield stress, μ is the viscosity, and $\dot{\gamma}$ is the shear rate of the flow. In order to directly obtain the apparent viscosity, all terms of the equation can be divided with shear rate, $\dot{\gamma}$, as shown in Eq. (2) below:

$$\mu_{app} = \frac{\tau_y}{\dot{\gamma}} + \mu \quad (2)$$

In the Bingham fluid flow, plug flow region is observed, which is shown in Figure 2, and the plug thickness, δ can be expressed in Eq. (3) as follows [18]:

$$\delta = -\frac{2\tau_y}{\Delta P/L} \quad (3)$$

It is well known that as the applied magnetic flux increases, yield stress τ_y increases and leads to an increased plug thickness. On the other hand, as the frequency increases, the pressure drop per length increases and leads to a decreased plug thickness. At high frequencies and under low magnetic flux conditions (e.g., at 0 A), the plug thickness approaches zero, and the velocity profile does not change further with the increase in frequency.

To investigate the effect of temperature on the resistance force of the MR damper, an experimental analysis was conducted in Sakarya University Mechanical Engineering Fracture Mechanics Laboratory, as shown in Figure 3. A commercial LORD RD-8041-1 MR damper was tested using an MTS 890 axial-torsional test system. The uncertainty of the load cell in axial load is measured as 3.15% between 0 and 2kN [6]. The tests were conducted at 4 different frequencies, 8 different current and 7 different temperatures which make 224 individual tests in total. The operating temperature ranged from 10 °C to 70 °C, with an increment of 10 °C. The current varied from 0 A to 1 A with an increment of 0.1 A and from 1 A to 2 A with an increment of 0.5 A. A temperature-controlled bath and a surrounding water jacket were used to maintain a constant temperature during testing. Water temperature was regulated with a precision of ±0.1 °C. To eliminate transient thermal effects, each test began after the damper temperature stabilized for at least one minute. Each test consisted of 10 loading cycles, and the average of 4th, 5th and 6th cycle was considered as the test data.

A sinusoidal motion was applied to the MR damper, and the displacement of the MR damper d is shown below:

$$d = A \cdot sin(\omega t) \quad (3)$$

Where ω is the frequency, A is the maximum displacement, and t is the time. The frequency values were set to 0.4 Hz, 0.8 Hz, 1.2 Hz and 1.6 Hz. The amplitude was chosen as 20 mm, corresponding to a total stroke of 40 mm.

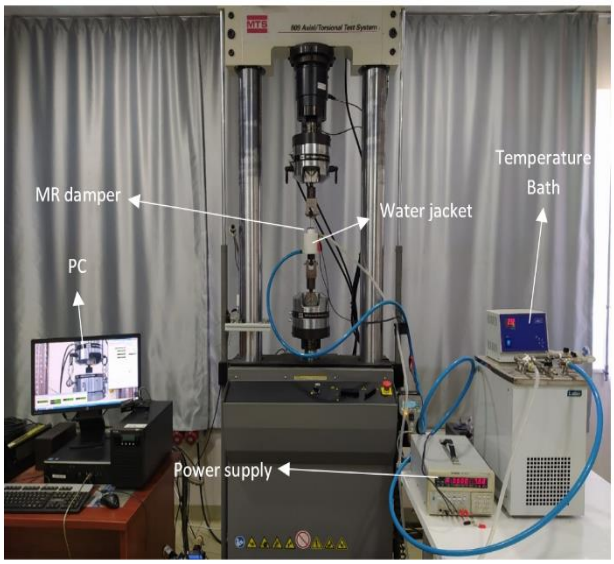

Figure 3. General view of the test setup.

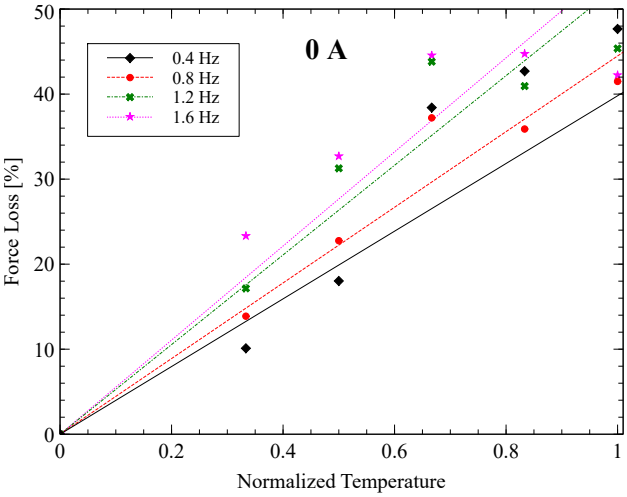

Figure 4. The variation of force loss ratio at 0 A with the normalized temperature.

3. Results and Discussion

In order to evaluate the experimental results, the minimum temperature was taken as the reference, and the percentage of force loss was calculated regarding the reference temperature. The normalized temperature θ was calculated using Eq. (4) below:

$$\theta = \frac{T - T_0}{T_h - T_0} \quad (4)$$

where T is the MR damper operating temperature, T_0 is the minimum temperature and T_h is the maximum temperature. T_0 was selected as 10°C and T_h was selected as 70°C. The force loss ratio was calculated from the Eq. (5) below:

$$Force\ loss\ [\%] = \frac{F}{F_a} \times 100 \quad (5)$$

Where F is the maximum force at the operating temperature and F_a is the maximum force at the minimum temperature, 10°C, during the sinusoidal motion cycles.

In Figure 4, the variation of the force loss ratio with the normalized temperature is illustrated at 0 A, which corresponds to the conventional viscous damping. A force loss of approximately 50% was observed when the operating temperature increased from 10°C to 70°C at a frequency of 0.4 Hz. This dramatic decrease at 0 A is also supported with the experiments in the literature where the force loss was reported to be 2.5 times greater at 0 A to that of observed at 3 A [16]. Considering the frequency, similar trends were observed. With the increasing frequency, the temperature effect tends to be slightly more significant. As the shear rate increases with the increasing frequency, the velocity profile does not change considerably at 0 A, as stated before, and the change in the apparent viscosity becomes marginal. Thus, the insignificant change in the force loss ratio with frequency can be attributed to the trivial difference in the apparent viscosity.

The variation of the force loss ratio at 1 A with the normalized temperature is shown in Figure 5. It can be seen that as the MR fluid is exposed to a magnetic field, the force loss becomes one-third of the value observed at 0 A. This indicates that the resistance force is less sensitive to the temperature variations when a magnetic field is applied (on-state). On the other hand, with increasing frequency, the force loss shows a significant change, unlike in the case without a magnetic field (off-state). This observation is consistent with findings in the literature, which report a 22% reduction in force loss at a frequency of 3 Hz and a current of 1 A [2]. This aligns with the 17.5% reduction observed in the present study at 1.6 Hz.

The variation of the force loss ratio at 2 A with the normalized temperature is shown in Figure 6. The difference in force loss ratios across various frequencies becomes more pronounced at elevated temperatures. This behavior can be attributed to the larger plug thickness under high magnetic fields, tending to shrink further with increasing frequency. As a result, varying velocity profiles are observed at different frequencies, leading to more significant variations in force loss.

A summary of the three plots is presented in Figure 7, illustrating the variation of force loss with frequency for different current levels. As previously discussed, force loss is largely independent of frequency at 0 A, corresponding to the off-state of the MR damper. In contrast, when the MR damper is in the on-state, the force loss is clearly influenced by frequency.

The variation of the force loss ratio with the current is shown for different frequencies in Figure 8. The curves were obtained using the moving average method. The force loss ratio was calculated based on the minimum and maximum temperature conditions for each current and frequency.

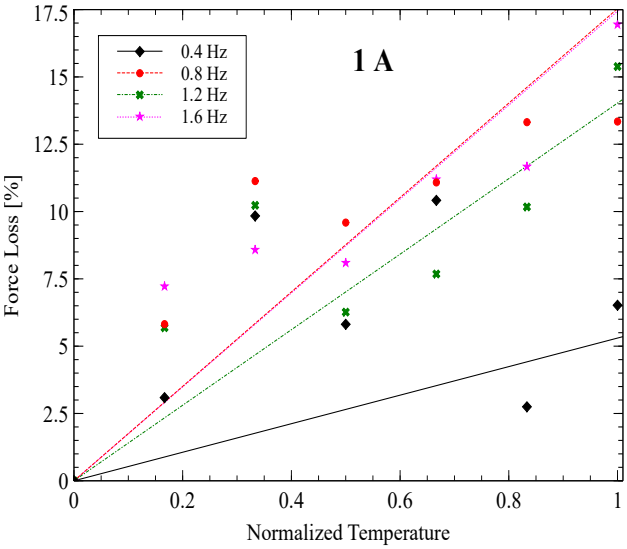

Figure 5. The variation of force loss ratio at 1 A with the normalized temperature.

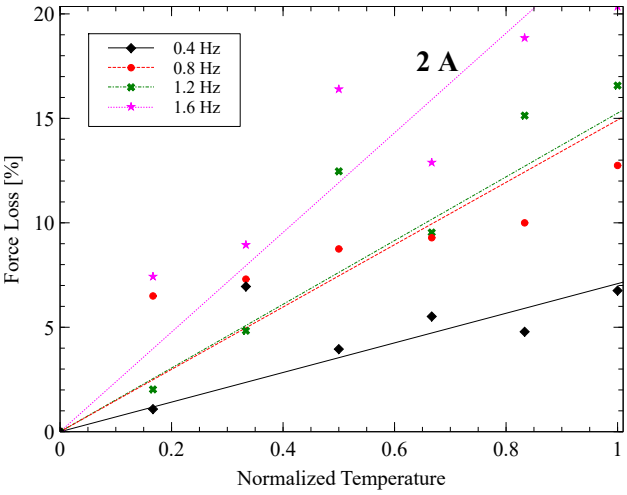

Figure 6. The variation of force loss ratio at 2 A with the normalized temperature.

The force loss ratio decreases with increasing current, indicating that the MR damper becomes less sensitive to temperature variations under the magnetic effect, as expected. Eventually, when the MR fluid saturates at the magnetic field around 1 A, the force loss ratio becomes nearly constant and independent of the current. The results also highlight frequency as a significant parameter in predicting force loss at higher current values. This is primarily due to the increase in plug thickness under strong magnetic fields. Consequently, higher frequencies are required to reduce or eliminate the plug region, as illustrated in Figure 2.

The variation of the force loss ratio with frequency at different current values is presented in Figure 8. The force loss ratio was calculated considering the minimum and maximum operating temperatures. It can be inferred that, in the absence of the magnetic field, the force loss ratio remains nearly constant with increasing frequency. On the contrary, at higher current levels, the force loss ratio varies significantly with frequency, indicating that the influence of

temperature becomes more frequency-dependent when a magnetic field is applied. As discussed before, this dependency of the temperature effect might be associated with the changes in the velocity profile. The plug starts to grow proportional to the applied field, and increasing frequencies become capable of reducing the thickness of the plug further, leading the force loss ratio increase continuously. On the other hand, under zero applied field, the flow is nearly Newtonian, and the plug region becomes minimal. In such cases, increasing the frequency has little to no further effect on plug thickness, resulting in a relatively stable force loss ratio. The slight decrease observed in Figure 8 at higher frequencies may be attributed to experimental uncertainty.

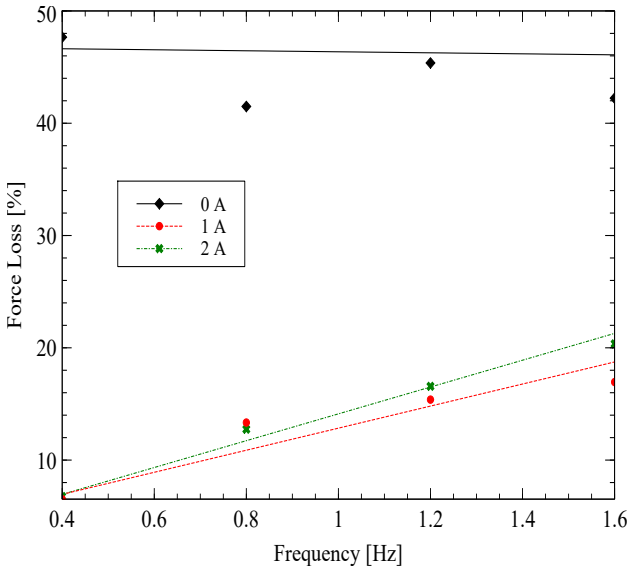

Figure 7. The variation of force loss ration with the frequency for different current levels.

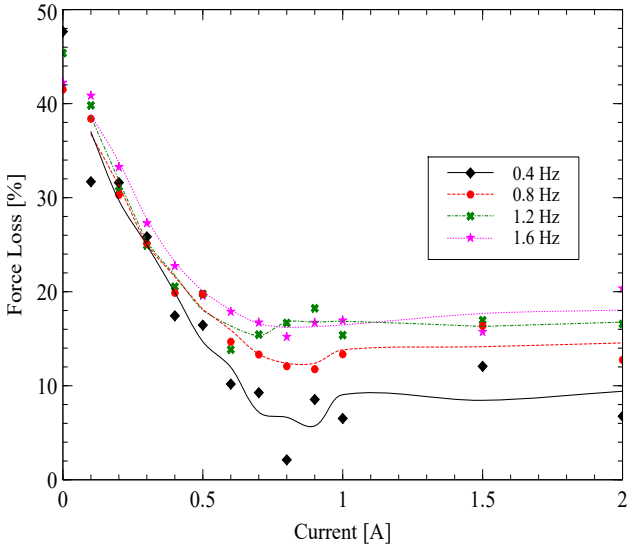

Figure 8. The variation of the force loss ratio with the current for different frequencies.

4. Conclusion

In this study, the effect of the temperature on the force loss of an MR damper was investigated under varying current and frequency conditions. Based on the findings, the following concluding remarks can be drawn.

- The results demonstrated that the temperature effect is most prominent in the absence of magnetic field, with up to 50% reduction in force observed across the experimental temperature range. Furthermore, the effect has still remained with a force loss of around 12% even when the magnetic field is applied.
- The study revealed a clear dependency of the force loss ratio on frequency, highlighting its critical role in the design of MR damper control algorithms.
- It was observed that the influence of frequency on the force loss becomes more significant under higher magnetic flux densities. This behavior is strongly associated with the variation in plug thickness of the velocity profile.

In conclusion, force loss must be considered in the design of the control algorithm under all operating conditions. While the results offer valuable insights, several limitations remain. Most notably, the temperature effect should be explored further at higher operating temperatures. Additionally, uncertainties in the experimental data limited deeper analytical interpretation such as generating an analytical correlation between viscosity and force loss. As future work, a comprehensive analytical framework can be developed to examine these interdependencies more rigorously and incorporate them into dynamic models of MR dampers.

Declaration

The author declared no potential conflicts of interest with respect to the research, authorship, and/or publication of this article. The author also declared that this article is original and was prepared in accordance with international publication and research ethics, and ethical committee permission or any special permission is not required.

Author Contributions

The author solely conducted all aspects of the study, including conceptualization, methodology, visualization, analysis, and manuscript preparation.

Acknowledgment

The author gratefully acknowledges The Scientific and Technological Research Council of Turkey (TÜBİTAK) for providing funding under Grant No. 115M363, which enabled the purchase of the MR damper used in this study. The author also extends special thanks to Tahsin Engin, the Principal

Investigator of the project, for his essential support in the project's development, management, and resource facilitation. Additionally, the author sincerely thanks Mehmet Faruk Yaren for his valuable support during the experimental tests.

Nomenclature

τ	: Shear stress
τ_y	: Yield stress
μ	: Viscosity
μ_{app}	: Apparent viscosity
ΔP	: Pressure loss
L	: Length
d	: Displacement
A	: Maximum displacement
ω	: Frequency
t	: time
θ	: Normalized temperature
T	: Temperature
T_0	: Minimum temperature
T_h	: Maximum temperature
F	: Force
F_a	: Maximum force

References

1. Batterbee, D.and Sims, N.D. *Temperature sensitive controller performance of MR dampers*. Journal of Intelligent Material Systems and Structures, 2009, ***20*** (3): p. 297–309.
2. Bharathi Priya, C.and Gopalakrishnan, N. Experimental Investigations of the Effect of Temperature on the Characteristics of MR Damper. 2019, pp. 435–443.
3. Bharathi Priya, C.and Gopalakrishnan, N. *Temperature dependent modelling of magnetorheological (MR) dampers using support vector regression*. Smart Materials and Structures, 2019, ***28*** (2).
4. Bompos, D.A.and Nikolakopoulos, P.G. *CFD simulation of magnetorheological fluid journal bearings*. Simulation Modelling Practice and Theory, 2011, ***19*** (4): p. 1035–1060.
5. Delijani, Y.M.Cheng, S.and Gherib, F. *Operational temperature effect on the behavior of magnetorheological dampers*. Engineering Structures, 2025, ***330*** p. 119940.
6. Demir, O.Ayhan, A.O.and İriç, S. *A novel test system for mixed mode-I/II/III fracture tests – Part 2: Experiments and criterion development*. Engineering Fracture Mechanics, 2019, ***220***.
7. Fu, Z.Gan, X.Liu, X.Jian, Z.and Hu, H. *Effect of temperature on the mechanics of magnetorheological fluid damper*. Journal of the Chinese Institute of Engineers, Transactions of the Chinese Institute of Engineers,Series A, 2022, ***45*** (2).
8. Goldasz, J.and Sapinski, B. Influence of temperature on the MR squeeze-mode damper. *Proceedings of the 2019 20th International Carpathian Control Conference, ICCC 2019*. 2019.
9. Gordaninejad, Faramarz Breese, D.G. *Heating of Magnetorheological Fluid Dampers*. Journal of Intelligent Material Systems and Structures, 1999, ***10*** (8): p. 634–645.
10. Kamath, G.M.Hurt, M.K.and Wereley, N.M. *Analysis and testing of Bingham plastic behavior in semi-active electrorheological fluid dampers*. Smart Materials and Structures, 1996, ***5*** (5): p. 576–590.
11. Kumar Kariganaur, A.Kumar, H.and Arun, M. *Effect of temperature on sedimentation stability and flow characteristics of magnetorheological fluids with damper as the performance analyser*. Journal of Magnetism and Magnetic Materials, 2022, ***555***.
12. Kumar Kariganaur, A.Kumar, H.and Arun, M. *Influence of temperature on magnetorheological fluid properties and damping performance*. Smart Materials and Structures, 2022, ***31*** (5).
13. Lee, D.-Y.and Wereley, N.M. *Quasi-Steady Herschel-Bulkley Analysis of Electroand Magneto-Rheological Flow Mode Dampers*. Journal of Intelligent Material Systems and Structures, 1999, ***10*** (10): p. 761–769.
14. Lee, U.Kim, D.Hur, N.and Jeon, D. *Design Analysis and Experimental Evaluation of an MR Fluid Clutch*. Journal of Intelligent Material Systems and Structures, 1999, ***10*** (9): p. 701–707.
15. Li, W.H.and Du, H. *Design and Experimental Evaluation of a Magnetorheological Brake*. The International Journal of Advanced Manufacturing Technology, 2003, ***21*** (7): p. 508–515.
16. Liang, G.Zhao, T.Li, N.Wei, Y.and Savaresi, S.M. *Magnetorheological damper temperature characteristics and control-oriented temperature-revised model*. Smart Materials and Structures, 2021, ***30*** (12).
17. McKee, M.Wang, X.and Gordaninejad, F. *Effects of temperature on performance of a compressible magnetorheological fluid damper-liquid spring suspension system*. Active and Passive Smart Structures and Integrated Systems 2011, ***7977:*** p. 797712.
18. Pang, N.M.W.and Li. *Nondimensional analysis of semi-active electrorheological and magnetorheological dampers using approximate parallel plate models*. Smart Materials and Structures, 1998, ***7*** (5): p. 732.
19. Parlak, Z.and Engin, T. *Optimal Magnetorheological Damper Configuration Using the Taguchi Experimental Design Method*. Journal of Mechanical Design, 2013, ***135*** (August): p. 08100/-8–1.
20. Rabinow, J. *The Magnetic Fluid Clutch*. Transactions of the American Institute of Electrical Engineers, 1948, ***67*** (2): p. 1308–1315.
21. Sahin, I.Cesmeci, S.and Wereley, N.M. Sensitivity of magnetorheological damper behavior to perturbations in temperature via Bouc - Wen model. *Electro-Rheological Fluids and Magneto-Rheological*

Suspensions - Proceedings of the 12th International Conference. 2011.

22. Sherman, S.G.Powell, L.A.Becnel, A.C.and Wereley, N.M. *Scaling temperature dependent rheology of magnetorheological fluids*. Journal of Applied Physics, 2015, ***117*** (17).
23. Tallman, M.J.Santner, C.and Miller, R.B. *US Patent - Temperature Compensation for Magnetorheological Fluid Dampers*. 2006, ***1*** (12).
24. de Vicente, J.Klingenberg, D.J.and Hidalgo-Alvarez, R. *Magnetorheological fluids: a review*. Soft Matter, 2011, ***7*** (8): p. 3701.
25. Wilson, N.L.and Wereley, N.M. *Analysis of a magnetorheological fluid damper incorporating temperature dependence*. Collection of Technical Papers - AIAA/ASME/ASCE/AHS/ASC Structures, Structural Dynamics and Materials Conference, 2010, (April).
26. Yu, J.Dong, X.Wang, X.Pan, C.and Zhou, Y. *Asymmetric Dynamic Model of Temperature-Dependent Magnetorheological Damper and Application for Semi-active System*. Frontiers in Materials, 2019, ***6***.
27. Zhang, X.Li, W.and Gong, X. *Thixotropy of MR shear-thickening fluids*. Smart Materials and Structures, 2010, ***19*** (12).
28. Zhu, H.Rui, X.Yang, F.Zhu, W.and Jiang, M. *Influence of temperature and internal leakage on magnetorheological damper*. International Journal of Mechanical System Dynamics, 2024, ***4*** (4): p. 487–496.
29. Zhu, X.Jing, X.and Cheng, L. *Magnetorheological fluid dampers: A review on structure design and analysis*. Journal of Intelligent Material Systems and Structures, 2012, ***23*** (8): p. 839–873.
30. Zschunke, F.Rivas, R.and Brunn, P.O. *Temperature Behavior of Magnetorheological Fluids*. Applied Rheology, 2005, ***15*** (2): p. 116–121.

Available online at www.dergipark.org.tr/en

INTERNATIONAL ADVANCED RESEARCHES and ENGINEERING JOURNAL

Journal homepage: www.dergipark.org.tr/en/pub/iarej

e-ISSN: 2618-575X

International Open Access

Volume 09
Issue 01

April, 2025

Research Article

Prediction of rolling force and spread in hot rolling process by artificial neural network and multiple linear regression

Fatih Yılmaz [a], ***Mehmet Ali Güvenç*** [b] ***and Selçuk Mıstıkoğlu*** [a]

[a]*Department of Mechanical Engineering, Faculty of Engineering and Natural Sciences, Iskenderun Technical University, Iskenderun, Hatay, 31200, Turkey*

[b]*Department of Aerospace Engineering, Faculty of Aeronautics and Astronautics, Iskenderun Technical University, Iskenderun, Hatay, 31200, Turkey*

ARTICLE INFO

Article history:
Received 23 October 2024
Accepted 16 January 2025
Published 23 April 2025

Keywords:
Artificial neural networks (ANN)
Hot rolling
Multiple linear regression (MLR)
Prediction performance
Rolling force
Spreading amount

ABSTRACT

The aim of this study is to compare the performance of multiple linear regression (MLR) and artificial neural network (ANN) models in predicting rolling force and spread during free rolling in the hot rolling process. Accurate prediction of rolling force and spread in hot rolling is critical for ensuring homogeneous load distribution across rolling stands, enhancing energy efficiency, reducing failure stops, and achieving dimensional accuracy and high-quality final products. The data used in this study were generated through FEM analysis, with a portion of the results verified experimentally. The dataset includes variables such as material temperature, rolled material dimensions, reduction amount, and rolling speed, all of which influence rolling force and spread. A maximum acceptable error rate of 2.9% for spread and 6.7% for rolling force was determined. Both MLR and ANN models were applied to the dataset, and their prediction performances were compared using the mean square error (MSE). For rolling force estimation, the ANN model achieved a training R value of 0.9888 and a test R value of 0.9844, while the MLR model obtained an R^2 value of 0.9651 and an adjusted R^2 value of 0.9829. In spread estimation, the ANN model achieved a training R value of 0.9947 and a test R value of 0.9844, compared to the MLR model's R^2 value of 0.9871 and adjusted R^2 value of 0.9863. The results indicate that both models perform comparably well in estimating rolling force and spread. However, the artificial neural network model demonstrates a slight advantage, offering marginally superior prediction performance.

1. Introduction

In recent years, reducing carbon emissions and dependency on oil for energy has become a priority. Increasing energy efficiency and optimizing production processes to produce the same quality products at lower costs have gained significant importance. Particularly in the steel sector, where energy consumption is high, the rolling process remains one of the most widely used production methods. In hot bar rolling mills, the number of passes and their design are critical parameters for ensuring product quality and energy efficiency. A correct pass design not only enhances energy efficiency but also reduces initial investment costs by enabling the selection of an optimal number of rolling stands and appropriately powered motors during the investment phase [1, 2].

During the rolling pass design process, the accurate calculation of rolling loads and spread is crucial. These calculations are essential to achieving the desired product properties and ensuring correct pass design. Rolling loads refer to the forces exerted on the material during rolling and depend on numerous factors, such as the dimensions, temperature, chemical composition, and section reduction of the rolled material. Accurate calculations of these loads are vital to controlling deformations and stresses during bar shaping. For instance, Houpping Hong (2019) calculated material sections and rolling loads in a six-pass design [3].

Material deformation at high temperatures plays a significant role in determining product quality and productivity. Specifically, the rolling force and spread of the material during rolling influence several parameters, including the dimensional accuracy of the final product, the power requirements of the rolling stands, roll wear, and energy consumption. In a study by D.H. Kim et al. (2002), roll wear was measured based on pass shapes, and its impact on the product cross-section was evaluated [4, 5].

The spread of the material determines how its dimensions change during shaping, ultimately affecting

* Corresponding author. Tel.: *+90 533 248 6916.*
E-mail addresses: *fatihfy@hotmail.com (F. Yilmaz), mali.guvenc@iste.edu.tr (M. Guvenc), selcuk.mistikoglu@iste.edu.tr (S. Mistikoglu)*
ORCID: *0009-0008-5438-1634 (F. Yilmaz), 0000-0002-4652-3048 (M. Guvenc), 0000-0003-2985-8310 (S. Mistikoglu)*
DOI: 10.35860/iarej.1564911

the rod's final shape. Accurate spread calculations are critical for achieving the desired product dimensions and shapes. In 1961, L.G.M. Sparling and B. Eng developed an empirical model to calculate the spread [6].

Numerous empirical formulas have been developed to calculate rolling forces and spread. While some provide accurate results under specific conditions, others are more reliable in particular scenarios [6]. With advancements in computer technology, the finite element method (FEM) has emerged as a powerful tool for calculating rolling forces and spread. FEM offers advantages over empirical formulas, such as the ability to handle a broader range of parameters and geometries. In 2014, J. Bartnicki modeled the rolling of hollow round materials using FEM and demonstrated its agreement with experimental results. More recently, Ana Claudia González-Castillo et al. (2021) utilized FEM analysis to predict mechanical properties in thermomechanical rolling, while Shafaa Al-Maqdi et al. (2020) performed FEM analyses under various rolling conditions for hot billet rolling processes [7–11].

Despite its accuracy, FEM faces limitations in industrial applications due to its computational complexity, long processing times, and the high cost of software licenses. However, it remains a flexible tool for studying parameters affecting rolling force by allowing the simulation of different experimental scenarios and adjustments to hot rolling models. For example, Zhenhua Wang et al. (2019) established a regression model of rolling force using FEM data for hot sheet rolling [12, 13].

Traditional approaches such as multiple linear regression (MLR) have been widely used to estimate critical process parameters. MLR models analyze linear relationships between input and output variables. However, the nonlinear and complex relationships inherent in hot rolling processes limit the performance of MLR models. In 2005, D.M. Jones et al. developed an MLR model based on data from a hot rolling mill and reported its performance metrics [12, 14].

In contrast, data-driven modeling techniques like artificial neural networks (ANN) have shown superior performance in modeling nonlinear systems. ANN models can effectively learn and predict input-output relationships, outperforming traditional methods like MLR. For instance, Mahdi Bagheripoor and Hosein Bisadi (2013) developed an ANN model for estimating rolling parameters in hot rolling processes, utilizing FEM analysis results for training. Ruihua Jiao et al. (2021) further advanced the field by introducing a deep learning model based on regenerative neural networks to predict roll wear in hot rolling processes [14–22]. ANN methods have also been applied successfully in optimizing production times and predicting diesel engine performance and emission parameters [23, 24].

The literature highlights FEM as a powerful approach for calculating rolling parameters, offering precise results. However, its application to rolling pass design is time-intensive and costly. Recent research has extensively examined MLR and ANN methods for estimating rolling parameters, yet studies focusing on the hot billet rolling process remain insufficient.

This study aims to comprehensively compare the performances of multiple linear regression (MLR) and artificial neural network (ANN) models in predicting rolling force and spread during the hot billet rolling process. By analyzing experimentally verified data generated through FEM, this research provides valuable insights for optimizing hot rolling processes and serves as a key resource for industry professionals. Unlike existing studies, which primarily examine these methods separately, this study fills a gap in the literature by directly comparing the two methods. Furthermore, the findings contribute to improving production efficiency and reducing costs by guiding the development of optimization strategies for multi-pass hot rolling.

2. Materials and Method

2.1 Hot Rolling Process and Obtaining Experimental Data

In the steel industry, hot rolling plays a critical role in producing high-quality products. In the hot rolling process used for manufacturing rebar and coils, steel billets are heated in annealing furnaces at temperatures ranging from 1000 to 1250 °C and subsequently rolled in rolling mills to achieve the desired section and shape. The length of the steel billets used in the continuous rolling process typically ranges from 6 to 12 meters.

In this study, experimental results obtained from the rolling mill of a rebar manufacturing company were utilized. Free rolling with uncalibrated flat rolls was examined. Steel billets measuring 150 mm × 150 mm and 12 meters in length were rolled under the parameters specified in Table 1.

The results of six experiments carried out on hot rolling processes are presented in Table 1. The column headings in the table explain the basic parameters and results of each experiment. The dimensional measurements of the rolled material are given in the first, second and third columns as shown in Figure 1, the material speed in meters/second in the fourth column, and the temperature of the rolled material in °C in the fifth column. The experimental results are given as the spread (width) of the rolled material in column six and the rolling force in kilonewton in column seven.

The spread of material was obtained by measuring the width of the material coming out of the rolling mill with the measuring caliper shown in Figure 2. In the measuring caliper, the material is squeezed between the two ends of the tongs to measure the width and height, and the thickness of the material is found by measuring the tongs distance with a caliper. The rolling forces were obtained from the rolling mill automation. The material chemical analysis results are given in Table 2.

Table 1. Experimental parameters and results

Input Height H1 (mm)	Input Width W1 (mm)	Output Height H2 (mm)	Rolling Speed U (m/sec)	Material Temp. T (°C)	Output Width W2 (mm)	Rolling Force F (kN)
150	150	100	0.31	1100	175	1120
150	150	110	0.31	1100	170	1000
150	150	120	0.31	1100	163	850
150	150	100	0.31	1050	176	1200
150	150	100	0.31	1150	177	950
150	150	100	0.21	1100	172	1000

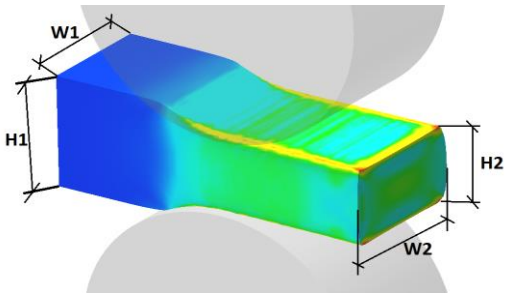

Figure 1. Rolled material measurement

Figure 2. Rolling stand and measuring caliper

Table 2. Chemical composition

%C	%Si	%Mn	%P	%S	%Cr	%Ni	%Mo
0.2028	0.1796	0.5651	0.024	0.0161	0.1257	0.1035	0.0172

2.2 Finite Element Method And Obtaining Results

Experiments in hot rolling processes are extremely costly and difficult to conduct. On the other hand, the finite element method gives very good results in the simulation of hot rolling processes.

In this study, SIMUFACT program was used for FEM analysis and in this program St32-2, which is the material closest to the chemical properties of rebar quality according to DIN 1700 standard, was used. It was defined with the code St37-2_h in Simufact forming software. Table 3 shows the chemical structure of St37-2 material according to DIN 1700 standard.

Table 3. St37-2 chemical composition according to DIN 1700 standard

%C	%Mn	%P	%S	%N	%Cu	CEV
Max. 0.2	Max. 1.4	Max. 0.04	Max. 0.04	Max. 0.012	Max. 0.55	Max. 0.38

The workpiece dimensions, rolling amount, rolling speed and rolling temperature minimum and maximum values are shown in Table 4. The workpiece length was taken as 400 mm in each analysis. A total of 87 different FEM analyses were performed in these intervals. Since the diameter of the roller used in the experiments was Ø420 mm, the same diameter roller was used in the FEM analysis.

In literature studies, it has been observed that the friction coefficient depends on the rolling speed and material temperature and is used between 0.30 and 0.45 [25-27]. In this study, the friction between the rolls and the workpiece during modeling in the FEM software was defined as 0.4 according to the Coulomb model.

In the modeling, the heat transfer coefficient between the workpieces was defined as 50 W/(m^2.K) and the heat radiation emission coefficient as 0.25. The initial temperature of the rolls was determined as 50 °C in accordance with industrial applications [28].

Hexahedral mesh was used for the analysis and the mesh spacing was determined as 2.6, and elements between 44,800 and 62,890 were used according to the workpiece dimensions.

The spread as a result of the simulation was obtained by measuring the material with a measuring tool in the result display window, as seen in Figure 3. The rolling force was taken with a 10% average from the graphic drawing window. The rolling force graph is shown in Figure 4.

Table 4. Value ranges in which the experiments were performed

	Input Height H1 (mm)	Input Width W1 (mm)	Output Height H2 (mm)	Rolling Speed u (m/sn)	Material Temperature T (°C)
Minimum	120	120	80	0.22	900
Maximum	150	150	145	1.1	1200

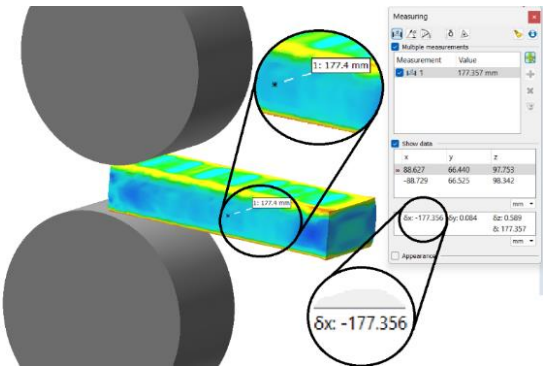

Figure 3. Measurement of the spread

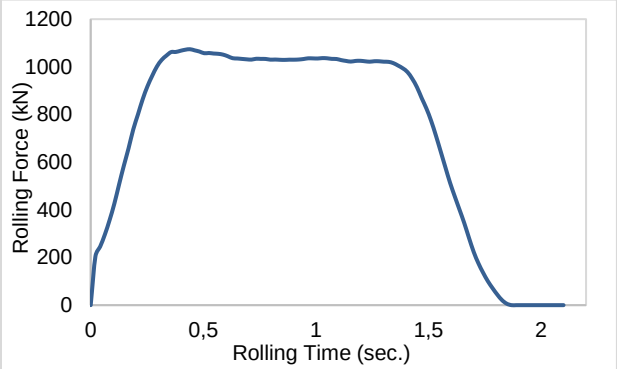

Figure 4. Rolling force graph

2.2 MLR and ANN Training

MLR analysis can be defined as a statistical technique in which the dependent variable is explained by more than one independent variable. This analysis allows determining how the dependent variable is affected by more than one independent variable and the relative effects of these variables on the dependent variable. In the analysis, the linear relationship between the dependent variable and the independent variables is modeled and the coefficients of the independent variables are calculated. Thus, it can be determined how much change a unit change in the independent variables causes in the dependent variable. MLR is a powerful tool for examining complex relationships between variables and making predictions. Multiple linear regression is as follows:

$$Y = a_1 + b_1x_1 + b_2x_2 + b_3x_3 + \cdots + b_ix_i \qquad (1)$$

Here Y is the dependent variable to be determined; x_1, x_2, x_3 … x_i are known variables for which estimates will be made and a, b_1, b_2, b_3 … bi are coefficients and the values are determined by the least squares method. MLR analysis was used to determine the relationship between the crushing force and the material dimensions of the spread, the rolling amount, the rolling speed. The MLR analysis was performed using Minitab version 18.

Artificial neural networks are a machine learning algorithm inspired by the working principle of the human brain. Its basic structure includes an architecture consisting of interconnected artificial neurons and input, hidden and output layers, as shown in Figure 5. Artificial neurons receive inputs, apply an activation function and transfer them to other neurons in a weighted manner. The network learns the relationship between input and output by working iteratively on training data. During this learning process, the weights are constantly updated and the most appropriate weight values are determined. Artificial neural networks have powerful features such as being able to model complex nonlinear relationships, make high-accuracy predictions and solve classification problems.

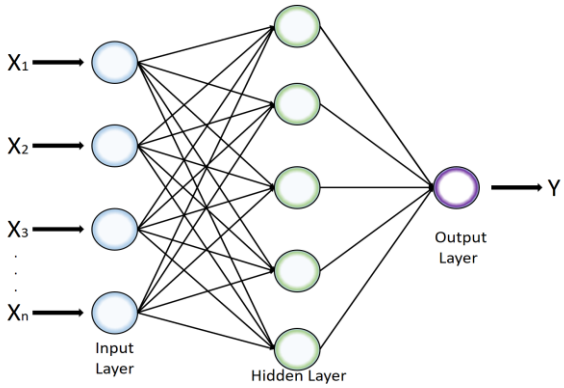

Figure 5. Schematic representation of artificial neural network

In this study, a 2-layer, 10-neuron neural network architecture was used to effectively model both the rolling force and the spread processes. The neural network, thanks to its ability to learn relationships between complex data, allows us to deeply analyze the interactions of these two critical parameters.

Various parameters were carefully determined in order to increase the effectiveness of the neural network training process. The model was trained for a total of 1000 epochs to provide an in-depth analysis of the learning process. During the iterations, the minimum gradient value was set to 10^{-7}, thus increasing the sensitivity of the network during the learning phase. The maximum error limit was set to 1000, thus clearly defining the acceptable error range of the model. The architecture used was determined as Feed-forward backpropagation type. Thanks to this structure, the weight ratios are updated backwards while the data is processed in the forward direction, thus optimizing the learning process for the network to produce more accurate results. During training, the Levenberg-Marquardt algorithm was preferred to provide fast and efficient learning; this algorithm provides high-speed convergence, allowing the model to reach optimal results in a shorter time. In addition, Gradient Descent with Momentum was used as the adaptation learning function. This method makes the learning process more stable, while a faster convergence is provided with the momentum contribution. Hyperbolic tangent sigmoid function is preferred as the transfer function; this function helps the model to learn non-linear relationships more effectively. As a result, the performance of the neural network will be evaluated with the mean square error criterion and thus the learning success will be revealed quantitatively [16].

3. Results and Discussion

Two different modeling approaches were used to estimate the spread and rolling force in the rolling process. First, numerical analysis was performed using the finite element method (FEM). In the FEM model, material spread and rolling forces were calculated. Then, FEM analyses were verified with experimental measurements and two different

prediction models were developed using the obtained data.

3.1 Comparison of FEM Results with Experimental Results

The aim of the study was to verify the analysis results performed using the finite element method (FEM) with experimental data. In this context, experimental measurements were performed on six different samples. The material dimensions used in the experiment, rolling speeds, and the spreading amounts and crushing forces obtained as a result of the experiments are shown in Table 5. The experimental results were compared with the results obtained with the FEM analysis and the differences between them were examined. As a result of the analyses, it was seen that the FEM model was compatible with the experimental data and represented the behavior of the real system with high accuracy. The comparison graphs of the spreading amount are shown in Figure 7 and the crushing force are shown in Figure 8.

When the experimental results are compared with the FEM results, an error between 0.6% and 2.9% in the spread and 1.7% and 6.7% in the rolling force is observed. These error rates can be considered at an acceptable level for rough rolling. Y. Mahmoodkhani calculated the error rate as less than 10% in his study in 2016, stated that this error rate is negligible in the calculation of crushing forces and developed an adjustment tool with this error margin [29].

3.2 MLR Results

MLR analysis was conducted using a total of 87 data points to better understand the relationship between rolling force and various influencing factors. The results are presented through various tables and graphs. Specifically, the variance analysis performed for rolling force is detailed in Table 6, which highlights the explanatory power of the model and the interactions between variables. Table 7 presents the coefficients related to rolling force, providing insights into the model's accuracy and functionality.

In MLR analysis, coefficients play a critical role in quantifying the effects of independent variables on the dependent variable. Each coefficient indicates the extent of change in the dependent variable resulting from a one-unit change in the corresponding independent variable. This allows for a clear interpretation of the variables' effects. The signs of the coefficients determine the direction of the effect, while their magnitudes indicate the relative importance of these effects. Properly determined coefficients enhance the predictive capability of the model and ensure more reliable results. As such, the coefficients serve as an essential reference point for evaluating the model's performance and identifying which factors have a more substantial impact on the dependent variable.

Additionally, Table 8 provides the error rates calculated for rolling force, offering valuable information about the model's performance. Figure 9 visualizes the error term distributions for rolling force, presenting the error distribution and statistical properties of the model through graphical representations. These findings form a crucial basis for assessing and validating the effectiveness of the MLR model.

Table 5. Comparison of FEM and experimental results

					FEM Results		Experimental Results	
Input Height H1 (mm)	**Input Width W1 (mm)**	**Output Height H2 (mm)**	**Rolling Speed u (m/s)**	**Material Temp. T (°C)**	**Output Width W2 (mm)**	**Rolling Force F (kN)**	**Output Width W2 (mm)**	**Rolling Force F (kN)**
150	150	100	0.33	1100	177	1045	175	1120
150	150	110	0.33	1100	172.9	955	170	1000
150	150	120	0.33	1100	165	810	163	850
150	150	100	0.33	1050	177.5	1180	176	1200
150	150	100	0.33	1100	178	925	177	950
150	150	100	0.22	1100	177	951	172	1000

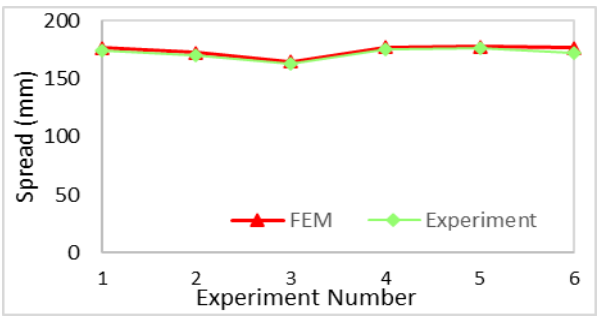

Figure 7. Comparison of spread FEM and experimental results

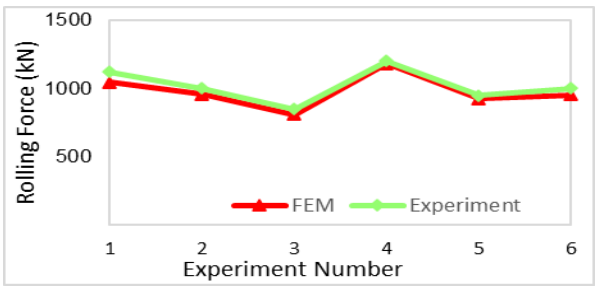

Figure 8. Comparison of rolling force FEM and experimental results

MLR analysis was performed according to the results of the spread for 87 analyses. This analysis was performed to better understand the relationship between the spread and various factors. The obtained data is presented with various tables and graphs. Table 9 presents the variance analysis for spread, while Table 10 includes the coefficients for spread. In addition, Table 11 includes the error rates calculated for spread, and these data help evaluate the performance of the model. Finally, the residual plots for spread are given in Figure 10. These graphs provide a better understanding of the results by visualizing the error distribution.

Table 6. Variance analysis for rolling force

Source	DF	Adj SS	Adj MS	F-Value	P-Value
Regression	5	6703984	1340797	447.91	0
Input Height	1	1137677	1137677	380.05	0
Input With	1	208485	208485	69.65	0
Output Height	1	3801779	3801779	1270.02	0
Rolling Speed	1	293421	293421	98.02	0
Material Temp.	1	789004	789004	263.57	0
Error	81	242471	2993		
Lack-of-Fit	79	231068	2925	0.51	0.851
Pure Error	2	11403	5701		
Total	86	6946455			

Table 7. Coefficients for rolling force

Term	Coef	SE Coef	T-Value	P-Value	VIF
Constant	1768	265	6.68	0	
Input Height	16,868	0.865	19.49	0	1.04
Input With	7.42	0.889	8.35	0	1.04
Output Height	-16.419	0.461	-35.64	0	1.05
Rolling Speed	311,3	31.4	9.9	0	1.06
Material Temp.	-2.502	0.154	-16.23	0	1.03

Table 8. Model summary for rolling force

S	R-sq	R-sq(adj)	R-sq(pred)
54.7126	0.9651	0.9629	0.9615

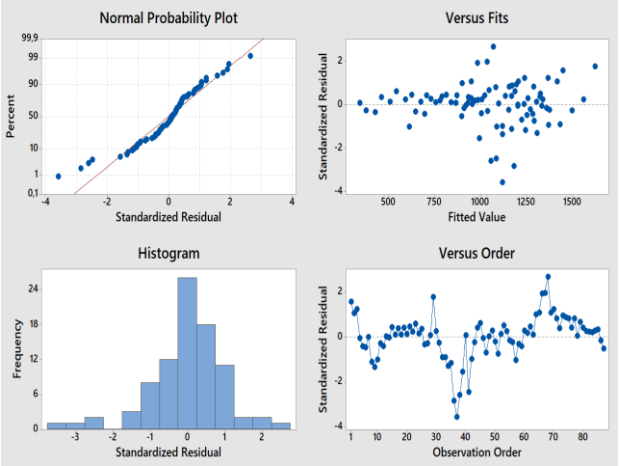

Figure 9. Residual Plots for Rolling Force

Table 9. Variance analysis for spread

Source	DF	Adj SS	Adj MS	F-Value	P-Value
Regression	5	13397.3	2679.46	1238.46	0
Input Height	1	1526.6	1526.65	705.63	0
Input Width	1	4558	4557.96	2106.72	0
Output Height	1	6506.4	6506.36	3007.28	0
Rolling Speed	1	920.3	920.3	425.37	0
Material Temp.	1	13.7	13.66	6.31	0.014
Error	81	175.2	2.16		
Lack-of-Fit	79	174.1	2.2	3.78	0.232
Pure Error	2	1,2	0.58		
Total	86	13572.5			

Table 10. Coefficients for spread

Term	Coef	SE Coef	T-Value	P-Value	VIF
Constant	-27.49	7.12	-3.86	0	
Input Height	0.6179	0.0233	26.56	0	1.04
Input Width	1.0972	0.0239	45.9	0	1.04
Output Height	-0.6793	0.0124	-54.84	0	1.05
Rolling Speed	17.435	0.845	20.62	0	1.06
Material Temp.	0.01041	0.0041	2.51	0.014	1.03

Table 11. Model summary for spread

S	R-sq	R-sq(adj)	R-sq(pred)
1.4709	0.9871	0.9863	0.9857

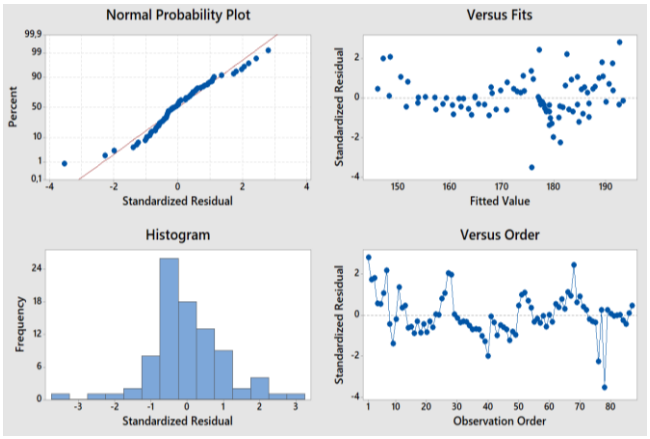

Figure 10. Residual Plots for Spread

3.3 ANN Results

A two-layer, ten-neuron artificial neural network model was developed to accurately predict the spread and rolling force of the material during the rolling process. This model allows us to better understand material behaviors thanks to its capacity to learn relationships between complex data. The learning performance of the rolling force is shown in detail in Figure 11. This visual reflects the results obtained during the training process of the neural network and the accuracy of the model. In addition, the error rates for the rolling force prediction are presented graphically in Figure 12.

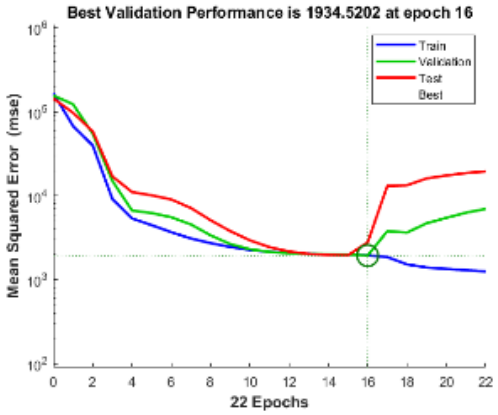

Figure 11. Training performance for rolling force

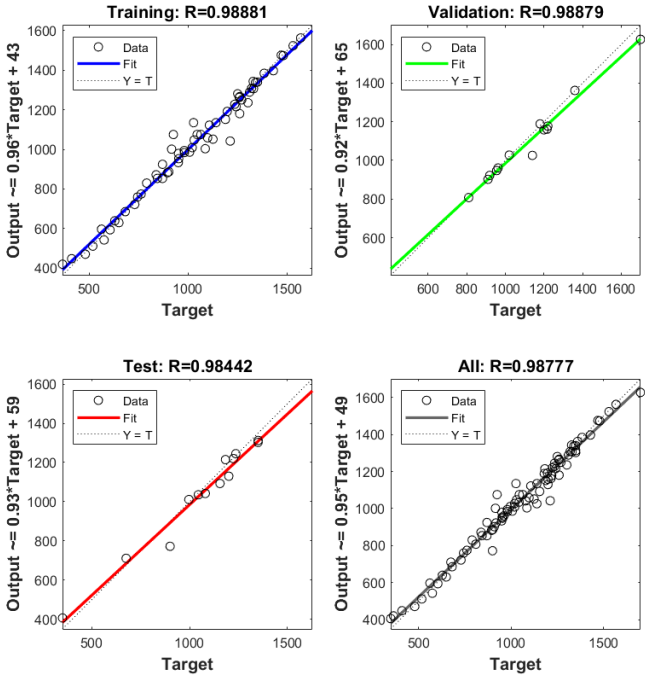

Figure 12. Regression results for rolling force

These graphics constitute an important source for evaluating the prediction performance of the model and visualizing the error distribution. These findings reveal the effectiveness of the neural network and provide valuable information for optimizing material processing processes.

The performance results obtained in the prediction of rolling force provide an important basis for evaluating the effectiveness and accuracy of the model. In the training phase, the R value of the model was calculated as 0,9888, which shows the high fit between the training data and the model. This high value reveals that the model successfully learned the data during the training process and has a strong ability to make predictions. In the validation phase, the R value was determined as 0,9887. This result shows that the model exhibits consistent performance with data other than training and has high generalization ability. The R value obtained in the testing phase was calculated as 0,9844, which shows that the model achieves successful results with data it has not used before. Finally, when all data are taken into account, the total R value was determined as 0,9877. This high value shows that the overall performance of the model is quite satisfactory and provides quite reliable results in the prediction of rolling force.

The learning performance for the prediction of the spread is presented in detail in Figure 13. This visual shows how effectively the model predicted the amount of spread during the training process and reflects the learning curve of the model. Figure 13 compares the results obtained during different iterations, showing the development and performance of the model over time. In addition, this graphic provides the opportunity to analyze the potential improvements in the learning process of the model and at which stages it is more successful. On the other hand, the regression results of the spread are shown graphically in Figure 14. These graphics clearly show the differences between the model's predictions and the actual values, visualizing the error distribution. The analysis of the error rates helps us understand under which conditions the model makes more errors and which factors affect the accuracy of the predictions. These two visuals provide a critical reference point for evaluating the prediction performance of the amount of spread and analyzing the effectiveness of the model.

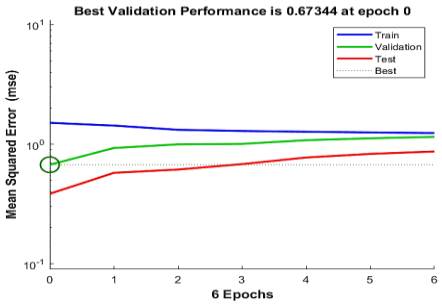

Figure 13. Training performance for spread

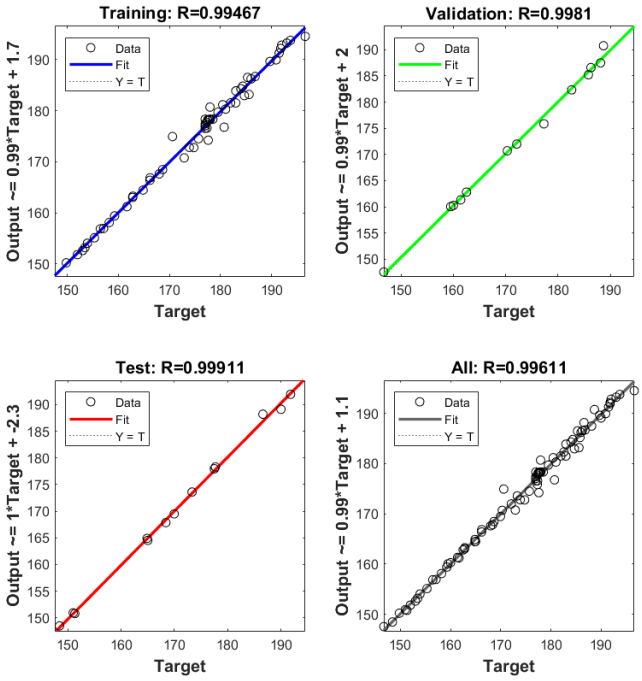

Figure 14. Regression results for spread

Table 12. MLR and ANN performance comparison

	Multi Liner Regression (MLR)			Artificial Neural Network (ANN)			
	R-sq	R-sq(adj)	R-sq(pred)	R (train.)	R (valid.)	R (test)	R (all)
Rolling Force	0.9651	0.9629	0.9615	0.9888	0.9887	0.9844	0.9878
Spread	0.9871	0.9863	0.9857	0.9947	0.9981	0.9991	0.9961

The results obtained in estimating the spread show a very good performance. The R value was calculated as 0,9946 in the training phase, which shows that the model provides excellent compatibility with the training data. The R value was determined as 0.9881 in the validation process, which shows that the model also shows consistent performance with new data. The R value obtained in the testing phase was calculated as 0.9991, which shows that the model achieved very successful results with data it had not seen before. The total R value was determined as 0.9961, which indicates that the results of the artificial neural network model showed a very high correlation with the data. These findings reveal that the model's ability to estimate the spread is extremely strong.

3.4 Comparison of MLR and ANN Results

MLR analysis is a traditional method often used to describe linear relationships between dependent and independent variables. The model is relatively simple to construct and interpret, but its ability to capture complex, nonlinear relationships is limited. On the other hand, artificial neural networks are capable of learning complex, nonlinear relationships between input and output data. In particular, artificial neural networks may be a more suitable option for understanding how small changes in input parameters affect outputs.

In this study, both modeling approaches were trained and tested using experimental and finite element analysis data. The R values for both models are shown in Table 12.

4. Conclusions

The prediction of material spread and rolling force in the hot rolling process is critically important for process control and optimization. In this study, two different modeling approaches, namely multiple linear regression (MLR) and artificial neural networks (ANN), were utilized and compared for predicting these parameters.

The maximum error rate in spread was observed to be 2.9%, with the FEM result recorded as 177 mm and the experimental result as 172 mm. The minimum error rate was found to be 0.6%, with the FEM result recorded as 178 mm and the experimental result as 177 mm. For rolling force, the maximum error rate was determined to be 6.7%, with the FEM result recorded as 1045 kN and the experimental result as 1120 kN, while the minimum error rate was 1.7%, with the FEM result recorded as 1180 kN and the experimental result as 1200 kN. The FEM and empirical results were found to be closely aligned and highly consistent.

In rolling force prediction, the training R value of the ANN model was 0.9888, and the test R value was 0.9844. In contrast, the R^2 value for the MLR model was 0.9651, with an adjusted R^2 value of 0.9829. For spread prediction, the ANN model achieved a training R value of 0.9947 and a test R value of 0.9844, while the R^2 value for the MLR model was 0.9871, with an adjusted R^2 value of 0.9863. Both models provided closely aligned predictions for rolling force and spread in the hot rolling process. However, the ANN model demonstrated slightly superior performance in rolling force prediction.

This study systematically compares the performance of MLR and ANN models, offering a novel contribution to both academic literature and industrial applications, thereby addressing a significant gap in this field. The findings have the potential to enhance production efficiency and reduce costs, facilitating the development of optimization strategies for multi-pass hot rolling processes.

Declaration

The authors declared no potential conflicts of interest with respect to the research, authorship, and/or publication of this article. The authors also declared that this article is original, was prepared in accordance with international publication and research ethics, and ethical committee permission or any special permission is not required.

Author Contributions

Fatih Yilmaz: Conceptualization, Methodology, Software, Visualization, Investigation. Mehmet Ali Guvenc: Investigation, Resources, Data curation, Writing - original draft and supervision. Selcuk Mistikoglu: Supervision.

Acknowledgment

This study is derived from Fatih Yılmaz's doctoral thesis. I would like to extend my sincere gratitude to Fatih Yılmaz for his significant academic contributions and foundational work, which have greatly influenced and enriched the scope of this study. I would like to thank Ekinciler Iron and Steel Ind. Inc. for their support and contributions to this study. I am especially grateful to the team members for their professionalism and helpfulness in carrying out the experiments.

References

1. Kun He and Li Wang, A review of energy use and energy-efficient technologies for the iron and steel industry, Renewable and Sustainable Energy Reviews,

2016, **70**: p. 1022-1038.

2. Viktoriya Chubenko, Alla Khinotskaya, Tatiana Yarosh, and Levan Saithareiev, Sustainable development of the steel plate hot rolling technologydue to energy-power process parameters justification, ICSF 2020, **166**(06009).
3. Huipping Hong, Roll Pass Design and Simulation on Continuous Rolling of Alloy Steel Round Bar, 9th International Conference on Physical and Numerical Simulation of Materials Processing, 2019, **37**: p. 127-131.
4. D.H. Kim, Y. Lee, B.M. Kim, Application of ANN for the dimensional accuracy of workpiece in hot rod rolling process, Journal of Materials Processing Technology, 2002, **130-131**: p. 214-218.
5. Jingyi Liu, Xinxin Liu and Ba Tuan Le, Rolling force prediction of hot rolling based on GA-MELM, Hindawi Complexity 2019, Volume 2019(3476521).
6. L. G. M. Sparling, B.Eng., Formhla For 'Spread' In Hot Flat Rollıng, Applıed Mechanıcs Group, 1961, **175**(1): p.604-640.
7. J. Bartnıckı, Fem Analysıs Of Hollow Hub Formıng In Rollıng Extrusıon Process, Metabk, 2014, **53**(4): p. 641-644.
8. Ana Claudia González-Castillo, José de Jesús Cruz-Rivera, Mitsuo Osvaldo Ramos-Azpeitia, Pedro Garnica-González, Carlos Gamaliel Garay-Reyes, José Sergio Pacheco-Cedeño ve José Luis Hernández-Rivera, 3D-FEMSimulation of Hot Rolling Process and Characterization of the Resultant Microstructure of a Light-Weight Mn Steel, Crystals, 2021, **11**(5):569.
9. Shafaa Al-Maqdi, Jaber Abu Qudeiri and Aiman Ziout, Optimization of flat rolling process through a simulation approach using simufact forming, Proceedings of the International Conference on Industrial Engineering and Operations Management, 2020. Dubai: p. 2031-2044.
10. X. Wanga, K. Chandrashekhara, M.F. Buchely, S. Lekakh, D.C. Van Aken, R.J. O'Malley, G.W. Ridenour, E. Scheid, Experiment and simulation of static softening behavior of alloyed steel during round bar hot rolling, Journal of Manufacturing Processes, 2020, **52**:p 281-288.
11. Mehmet Akkaş, Burak Onder, Ezgi Sevgi, Osman Çulha, Computer Aided Design, Analysis and Manufacturing of Hot Rolled Bulb Flat Steel Profiles, ECJSE , 2020, **7**(1): p. 9-19.
12. Zhenhua Wang, Dianhua Zhang, Dianyao Gong And Wen Peng, A new data-driven roll force and roll torque model based onfem and hybrid pso-elm for hot strip rolling, ISIJ International, 2019, **59**(9): p. 1604–1613.
13. U. Hanoglu, B. Šarler, Multi-pass hot-rolling simulation using a meshless method, Computers and Structures, 2017, **194**: p. 1-14.
14. Emre Alan, İ. İrfan Ayhan, Bilgehan Ögel and Deniz Uzunsoy, A comparative assessment of artificial neural network and regression models to predict mechanical properties of continuously cooled low carbon steels: an external data analysis approach, Journal of Innovative Engineering and Natural Science, 2024, **4**(2): p. 495-513.
15. D. M. Jones, J. Watton and K. J. Brown, Comparison of hot rolled steel mechanical property prediction models using linear multiple regression, non-linear multiple regression and non-linear artificial neural networks, Ironmaking and Steelmaking, 2005, **32**(5): p. 435-442.
16. Mahdi Bagheripoor, Hosein Bisadi, Application of artificial neural networks for the prediction of roll force and roll torque in hot strip rolling process, Applied Mathematical Modelling, 2013, **37**(7): p. 4593-4607.
17. Muhammad Asif Zahoor Raja, Muhammad Anwaar Manzar, Raza Samar, An efficient computational intelligence approach for solving fractional order Riccati equations using ANN and SQP, Applied Mathematical Modelling, 2015, **39**(10-11): p. 3075-3093.
18. Ruihua Jiao, Kaixiang Peng, Member, IEEE, and Jie Dong, Remaining useful life prediction for a roller in a hot strip mill based on deep recurrent neural networks, IEEE/CAA Journal Of Automatica Sinica, 2021, **8**(7): p. 1345-1354.
19. Rakhoon Hwang, Hyeontae Jo, Kyung Seok Kim, and Hyung Ju Hwang, Hybrid model of mathematical and neural network formulations for rolling force and temperature prediction in hot rolling processes, IEEE Access, 2017, **8**: p. 153123 - 153133.
20. Zhen-Hua Wang, Dian-Yao Gong, Xu Li & Guang-Tao Li, Dian-Hua Zhang, Prediction of bending force in the hot strip rolling process using artificial neural network and genetic algorithm (ANN-GA), Int J Adv Manuf Technol, 2017, **93**: p. 3325-3338.
21. Jifei Deng, Jie Sun, Wen Peng, Yaohui Hu, Dianhua Zhang, Application of neural networks for predicting hot-rolled strip crown, Applied Soft Computing Journal, 2019, **78**: p. 119-131.
22. F. Capece Minutolo, M. Durante, L. Giorleo, and A. Langella, Specific pressure in steel rod rolling with grooves, JMEPEG, 2005, **14**: p. 378-382.
23. Yusuf Karabacak, Doğan Şimşek and Nuri Atik, Combined application of ANN prediction and RSM optimization of performance and emission parameters of A Diesel Engine Using Diesel-Biodiesel-Propanol Fuel Blends, International Advanced Researches And Engineering Journal, 2023, **7**(3): p. 165-177.
24. Burcu Ozcan, Pınar Yıldız Kumru and Alpaslan Fığlalı, Forecasting operation times by using Artificial Intelligence, International Advanced Researches And Engineering Journal, 2018, **2**(2): p. 109-116.
25. Francesco Lambiase, Prediction of geometrical profile in slit rolling pass, Int J Adv Manuf Technol, 2014, **71**: p. 1285-1293.
26. Xingdong Li, Rolling force prediction of hot strip based on combined friction, Materials Science and Engineering, 2017. 4th AMMSE 2017 **269**(012053).
27. Matruprasad Rout, Surjya K. Pal, Shiv B. Singh, Finite element modeling of hot rolling: Steady- and unsteady-state analyses, Computational Methods and Production Engineering, 2017, p. 83-124.
28. Zhenhua Wang, Gengsheng Ma, Dianyao Gong, Jie Sun, Dianhua Zhang, Application of mind evolutionary algorithm and artificial neural networks for prediction of profile and flatness in hot strip rolling process, Neural Processing Letters, 2019, **50**: p. 2455-2479.
29. Y. Mahmoodkhani, M. A. Wells, G. Song, Prediction of roll force in skin pass rolling using numerical and artificial neural network methods, Ironmaking & Steelmaking, 2016, **44**(4): p.281-286.

Available online at www.dergipark.org.tr/en

INTERNATIONAL ADVANCED RESEARCHES and ENGINEERING JOURNAL

Journal homepage: www.dergipark.org.tr/en/pub/iarej

e-ISSN: 2618-575X

International Open Access

Volume 09
Issue 01

April, 2025

Research Article

Investigation of UV aging influence on low velocity impact behavior of interply hybrid composites

Zeynal Abidin Oğuz [a,b*]

[a*]*Department of Mechanical Engineering, Adıyaman University, Adıyaman 02040, Turkey*
[b]*Besni Ali Erdemoğlu Vocational School, Department of Mechatronic, Adıyaman University, Adıyaman 02040, Turkey*

ARTICLE INFO

Article history:
Received 18 October 2024
Accepted 16 January 2025
Published 23 April 2025

Keywords:
Hybrid composites
Low-velocity impact test
Polymer
UV aging

ABSTRACT

This study investigates the effects of UV aging on the low-velocity impact behavior of hybrid and non-hybrid polymer composites, focusing on configurations using glass and aramid fibers. Composite samples were exposed to UV radiation for 0, 450, and 900 hours, and their impact properties were measured through flatwise and notchwise Charpy impact tests. Results showed significant degradation after 450 hours, with the glass/epoxy composite (P1) exhibiting a 35.37% reduction in flatwise impact strength from 65.77 kJ/m² to 42.51 kJ/m². Hybrid composites, such as the glass-aramid-glass configuration (H1), demonstrated improved resilience, with a smaller 29% decrease to 77.04 kJ/m². After 900 hours of exposure, all configurations showed partial recovery in impact properties, attributed to possible matrix reorganization; however, the overall impact strength remained lower than in non-aged samples. For instance, flatwise impact strength in P1 was reduced by 17.87% compared to control, while H1 and H2 hybrids experienced 17.07% and 21.75% reductions, respectively. These findings underscore that hybridization, especially with aramid, enhances resistance to UV-induced degradation, suggesting hybrid composites as superior candidates for applications in UV-intensive environments.

1. Introduction

Polymer based composite materials are preferred in engineering studies and research for several key reasons, primarily due to their superior properties and performance advantages over traditional materials like metals or pure polymers. Composites, especially those made from carbon, glass, aramid offer high strength while being much lighter than metals like steel or aluminum. This makes them ideal for aerospace, automotive, and marine applications where weight reduction is crucial for efficiency. Despite being lightweight, composites can offer excellent mechanical strength, often outperforming traditional materials in specific applications [1].

Unlike metals, composites can be engineered to provide strength and stiffness in particular directions, based on how the fibers are oriented. This allows optimization of performance in areas of high stress. One of the most convenient ways to do this is to hybridize different fabric types with different arrangements, such as layer-by-layer or interlayer [2-4]. Hybridization in composite materials refers to the combination of two or more different types of fibers (e.g., glass, carbon, aramid) or matrices within a single composite structure. The purpose of this approach is to capitalize on the distinct advantages of each material, creating a composite that offers a balanced combination of properties that no single material could provide on its own. Hybrid composites are designed to meet specific engineering requirements more effectively than traditional composites [5]. Furthermore, hybridization can enhance the material's ability to absorb energy during impact (e.g., by including tough fibers like aramid), while still maintaining high tensile strength and stiffness from fibers like carbon or glass.

Composites, especially hybrid ones (combining materials like glass and aramid fibers), can offer better impact resistance than metals in certain configurations, which is important for safety-critical applications like automotive crash structures or protective gear. Impact testing is crucial in composite materials for several reasons, as it helps determine the material's behavior under sudden loads or forces. These insights are critical for

* Corresponding author. Tel.: *+90 554 845 42 05*.
E-mail addresses: zoguz@adiyaman.edu.tr *(Z. A. Oğuz)*
ORCID: 0000-0002-8566-2331 *(Z. A. Oğuz)*
DOI: 10.35860/iarej.1570089

ensuring the reliability, safety, and performance of composite structures in real-world applications. Impact resistance is a measure of how well a material can absorb energy and resist damage when subjected to a sudden force [6,7]. Composite materials, especially in industries like aerospace, automotive, and sports, are often exposed to impact forces (e.g., crashes, collisions, falling objects). Impact testing provides essential data on how well the material can handle these conditions without suffering catastrophic failure. Impact testing is used to compare how composite materials perform under different conditions, such as varying temperatures, environmental exposure (e.g., UV aging, moisture), and different fiber arrangements or hybrid combinations. This is especially important in determining how composites will react to impacts in different environments or after long-term exposure to elements that could degrade the material. Environmental conditioning is critical for composite materials because they are often exposed to various environmental factors-such as temperature fluctuations, humidity, UV radiation, and chemical exposure-that can significantly affect their performance, durability, and long-term reliability. These factors can degrade the mechanical and physical properties of composites, influencing their behavior in real-world applications. Understanding how composites respond to environmental conditions is essential for accurate material selection, design, and maintenance [8-11].

Fiore et al. [12] evaluated the aging resistance of jute-basalt hybrid composites, which are proposed as novel multilayer structures for cladding. The study compares the aging performance of jute-reinforced laminates with two different hybrid laminates, which use a combination of jute and basalt fibers arranged in different stacking configurations (sandwich and intercalated). The composites were subjected to accelerated aging cycles involving hygrothermal stress and UV radiation over 84 days. Samples were tested after 14, 28, 56, and 84 days. Mechanical tests, including flexural tests, impact tests, and dynamic mechanical analysis (DMA), were performed on the aged and unaged samples to evaluate their mechanical behavior and aging resistance. The results showed that the hybrid laminates (both sandwich and intercalated) exhibited better impact energy absorption and flexural properties than the jute-only laminates. The sandwich configuration showed superior aging resistance due to the barrier effect of the outer basalt layers, which protected the internal jute layers from degradation. Post-curing reactions in the early aging stages enhanced the matrix stiffness and improved fiber-matrix adhesion, but long-term exposure led to degradation from UV radiation and moisture, reducing mechanical properties over time.

Mayandi et al. [13] investigated the durability and degradation of fiber-reinforced polymer (FRP) hybrid composites when exposed to different environmental conditions (thermal aging, hydrothermal conditions, UV radiation, seawater, and acidic environments). It was found that elevated temperatures and moisture exposure lead to rapid degradation, reducing strength and stiffness. Further, UV exposure causes surface degradation, resulting in matrix cracking and fiber weakening. The researchers reported that UV exposure results in surface cracking, discoloration, and embrittlement of the polymer matrix. This degradation weakens the interfacial bonding between fibers and the matrix, leading to a reduction in mechanical performance, especially in terms of impact resistance. Also, it was observed that The UV radiation causes cracks in the matrix, reducing the durability and strength of the composites.

Silva et al., [14] researched the impact properties of curaua/aramid hybrid composites under UV B radiation. Samples were exposed to UV-B radiation for 300 and 600 hours. The effects of UV radiation led to changes in the macromolecular structure of curaua fibers. UV exposure increased the degree of cross-linking in the polyester matrix, resulting in a stiffer material but reduced its capacity to absorb impact energy. The ballistic performance decreased after UV exposure; however, samples exposed for 600 hours performed better than those exposed for 300 hours. Ballistic tests showed that absorbed energy was approximately 14% lower in UV-exposed samples compared to non-irradiated ones

Gualberto et al. [15] researched the ultraviolet radiation impact on the mechanical behavior of glass fiber reinforced polymers (GFRP). GFRP subjected to UV radiation for up to 180 days and expose to test at the end of each 30-day period. It was reported from results that the tensile strength of the composites decreased by 3.4% after 30 days and by 18.7% after 90 days of UV exposure. However, an improvement in strength was observed after 120 days, likely due to post-curing effects from elevated temperatures. When bending test results are examined it was found that an initial increase in flexural strength of 54.1% was noted after 30 days. However, starting from 60 days, a decrease in strength began, with the strength remaining 18.9% higher than the unaged composite after 180 days.

Nicholas et al. [16] examined the effects of accelerated environmental aging on glass fiber-reinforced thermoset polyurethane composites, specifically focusing on microstructure and impact behavior. The researchers used a combination of hygrothermal and UV exposure to simulate environmental conditions and conducted tests at intervals of 250, 500, 750, and 1000 hours. It was found that no significant change in the bulk impact properties of the composites. The materials demonstrated strong resistance to environmental aging, with only minimal variation (less than 10%) in maximum load and absorbed

energy across different impact energies (10 J, 20 J, and 30 J). Further, researchers revealed that the accelerated environmental aging caused surface-level deterioration, particularly in color and fiber exposure. However, the bulk mechanical properties, such as impact resistance, remained largely unaffected due to the protective effect of the glass fiber reinforcement.

Uddin et al. [17] investigated the effects of UV light and moisture on the low-velocity impact resistance of three different carbon fiber-reinforced composites: unidirectional, plain weave woven, and non-crimp fiber (NCF) laminates. At the end of study, it was reported that after UV and moisture exposure, all laminates showed a decrease in impact performance, but NCF laminates showed the least degradation compared to unidirectional and woven laminates. The results showed that the absorbed energy by the unidirectional laminate, woven laminate, NCF-symmetric laminate and NCF-a symmetric laminate reduced 20.98, 17.7, 1.06 and 1.39% respectively, after UV aging.

Barvarz et al. [18] assessed the mechanical, water absorption, and aging properties of polypropylene (PP) hybrid composites reinforced with flax and glass fibers. The aim was to assess the impact of glass fiber hybridization on the performance of these composites, focusing on water, thermal, and UV aging. It was revealed that Glass fibers accelerated the UV degradation of PP, with G40 (40 volume% glass) showing a 56% reduction in tensile strength after 400 hours of UV exposure. Conversely, flax fibers provided UV protection due to the lignin content, which absorbs UV radiation, leading to less degradation.

This study is important and original in its focus on the effects of UV aging on hybrid composites, specifically glass-aramid configurations, under impact conditions-a topic that has seen limited exploration in the existing literature. While previous research has addressed the impact resistance of various fiber-reinforced composites and the degradation effects of environmental exposure, few studies provide a comprehensive comparison between hybrid and non-hybrid configurations under prolonged UV exposure. Additionally, this research uniquely employs both flatwise and notchwise Charpy impact tests, offering a dual approach to evaluating impact performance under different orientations. By examining the differences in impact strength and energy absorption over extended UV aging periods (450 and 900 hours), the study reveals crucial insights into the long-term durability and mechanical resilience of hybrid composites. Unlike earlier work, this investigation also highlights the specific structural advantages of layered glass-aramid configurations, which are shown to enhance impact resistance and UV stability compared to pure composites. These findings contribute novel information to the field, supporting the development of more resilient composite materials for UV-intensive environments, such as aerospace and automotive applications, where material integrity under prolonged environmental stress is critical.

2. Materials and Procedures

2.1 Materials

For this study, woven glass and aramid fabrics with densities of 202 and 170 g/m^2 and fabric thicknesses of 0.15 and 0.27 mm, respectively, were used. Additionally, MGS 285 series epoxy and hardener were used as the resin system. All materials were sourced from Dostkimya Company in Istanbul. Representations of aramid and glass fabrics are depicted in Figure 1 a) and b), respectively.

2.2 Manufacturing Process

The hand lay-up method was used to create composite plates at the ambient temperature of 25°C. All of the fabrics, hardener, and epoxy were provided by the Dostkimya Company in Istanbul. Hexion MGS-L285 epoxy and Hexion MGS-H285 hardener were combined in a 100:40 ratio. Epoxy resin and hardener were combined using a mechanical stirrer set at 8000 rpm for 10 minutes. For this study, composite plates were produced in four configurations, two of which were pure and two were hybrid with the sandwich model. The group consisting of 12 glass fabrics was named P1, and the group consisting of 12 aramid fabrics was named P2. In addition, the hybrid model created with three glass fabrics outside and six aramid fabrics inside was named H1, and the hybrid model created with three aramid fabrics outside and six glass fabrics inside was named H2. All layers are stacked in 0-90° orientation angles. The samples were cured for an hour at 80°C using a hot mold press (Figure 2 a)) fitted with flat molds and pressurized to 0.4 MPa. The laminates were not finished until they were at room temperature. Figure 2 b) shows a flow chart for a production process. The thickness of the samples is given in Table 1.

2.3 Accelerated UV Aging

In this study, accelerated UV testing was performed using OSRAM brand ultraviolet lamp in accordance with the relevant ASTM standard [19].

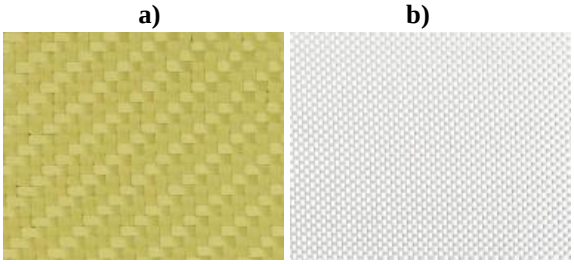

Figure 1. a) Aramid fabric b) Glass fabric

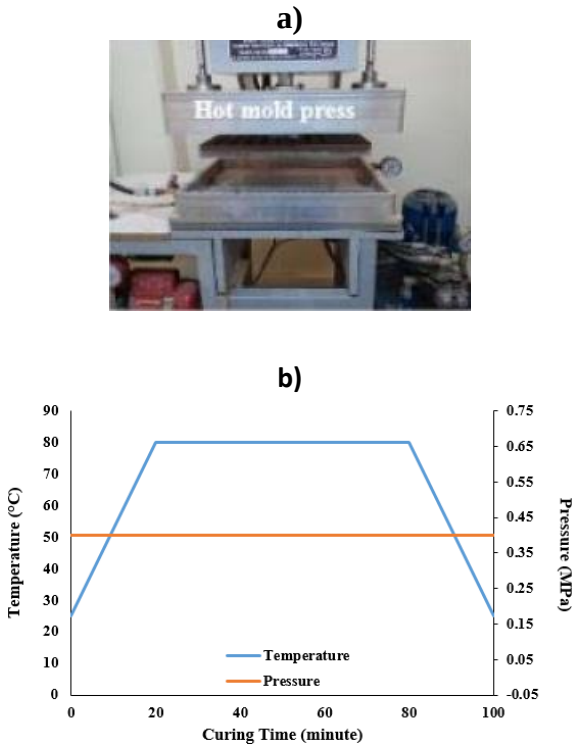

Figure 2. a) Hot mold press machine b) Production process

Table 1. Thickness of samples

Thickness (mm)			
P1	**H1**	**H2**	**P2**
2.41±0.03	2.45±0.02	2.82±0.05	2.91±0.07

Three groups of composite materials were produced for each configuration. One part of these was the control group (not exposed to UV aging), the other part was subjected to 450 hours of UV aging and the other part was subjected to 900 hours of UV aging. Five samples were tested for each group.

2.4 Low Velocity Charpy Impact Test

The 55 mm by 10 mm Charpy impact test specimens were created and examined in accordance with ISO 179/92 standards. The Charpy impact tests were performed on flatwise samples and edgewise samples using a pendulum impact machine with 15 J (Köger 3/70 Germany) (Figure 2). Equations (1) and (2) were used to compute the energy that was absorbed and impact toughness values, which were as follows:

$$E = E_i - E_f \quad (1)$$

$$K = \frac{E}{h\,x\,b} \quad (2)$$

Where E, E_i and E_f are the absorbed energy, initial energy and final energy, respectively. In addition, K, h and b symbolize toughness, sample thickness and width of the sample, respectively. The schematic illustration of flatwise and notchwise Charpy impact test is shown in Figure 3 a) and b), respectively.

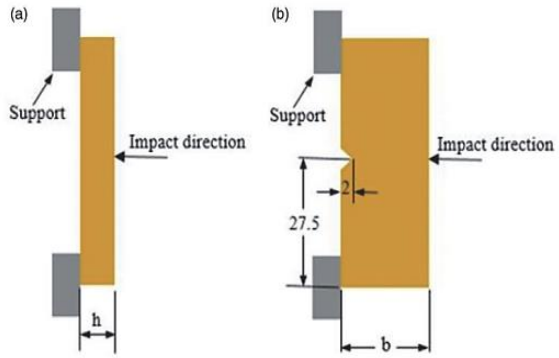

Figure 3. Schematic illustration of a) flatwise and b) notchwise Charpy impact test

3. Results and Discussions

The effects of UV aging duration and hybridization on the impact properties of the composite plates were systematically evaluated using both flatwise and notchwise Charpy impact tests. The results provide critical insights into how UV exposure influences the impact strength and energy absorption of different composite configurations. The impact strength and absorbed energy amounts for the flatwise Charpy impact test of the composite materials are presented in Figure 4 a) and b). In addition, the impact strength and absorbed energy amounts for the notchwise Charpy impact test are presented in Figure 5 a) and b).

It is clear that the composite fabric alignments have an effect on the impact properties of the materials for both the UV aging and control groups. The flatwise Charpy impact test results indicate that both UV aging and hybridization have significant effects on the impact strength and energy absorption of the composites.

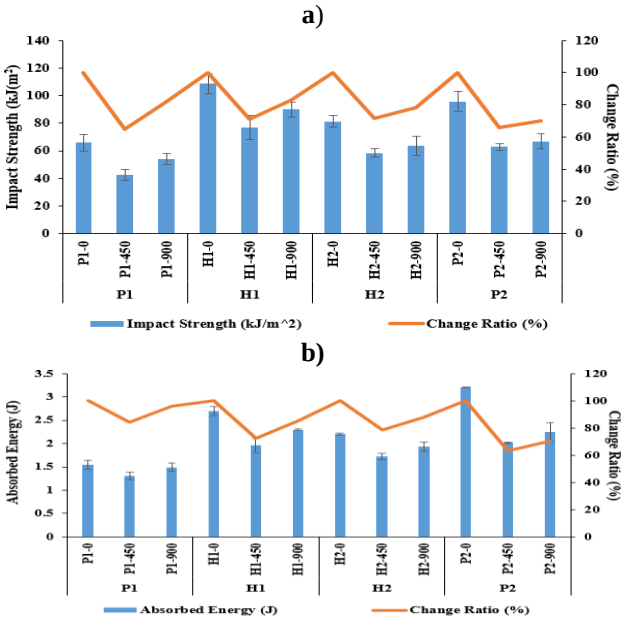

Figure 4. Flatwise Charpy Impact Test Graph a) Impact Strength b) Absorbed Energy

The flatwise Charpy impact test results of unaged samples showed that the highest flatwise impact strength was achieved by the H1 hybrid configuration (108.54 kJ/m²), followed by P2 (95.63 kJ/m²), H2 (81.26 kJ/m²), and the lowest for the non-hybrid P1 (65.77 kJ/m²). This suggests that hybridization, especially the glass-aramid-glass combination (H1), significantly improves the impact performance compared to pure configurations. Similarly, in terms of energy absorption, the P2 composite, composed entirely of aramid fabric, showed the highest energy absorption (3.2 J), whereas P1 absorbed the least (1.55 J). Both hybrid composites, H1 (2.7 J) and H2 (2.2 J), demonstrated intermediate values, confirming the effectiveness of hybridization in enhancing energy absorption. Flatwise impact test results are given numerically in Table 2.

When the results of the samples subjected to impact testing after 450 hours of UV aging were examined, there is a noticeable reduction in flatwise impact strength across all configurations after 450 hours of UV aging. P1 exhibited the most significant decrease (from 65.77 kJ/m² to 42.51 kJ/m², a 35.37% drop), highlighting the vulnerability of pure glass/epoxy to UV degradation.

Hybrid configurations again demonstrated superior durability under UV exposure. The impact strength for H1 dropped by approximately 29% to 77.04 kJ/m², while H2 saw a 28.18% decrease to 58.36 kJ/m². This shows that the hybrid composites, particularly H1, offer better UV resistance than the non-hybrid groups.

Energy absorption also followed a similar trend, with reductions observed for all configurations. P1 retained 1.31 J of absorbed energy (a 15.48% reduction), while H1 (1.96 J) and H2 (1.73 J) showed smaller relative decreases, confirming the protective role of aramid fibers against UV-induced degradation.

When the long-term (900 hours) accelerated UV aging results are carefully examined, after 900 hours, the impact strength of all composites showed signs of recovery or stabilization compared to the 450-hour results. For instance, P1 recovered slightly to 54.02 kJ/m², but this still represents an 17.87% reduction compared to the control group.

The hybrid configurations maintained their advantage, with H1 (90.01 kJ/m²) and H2 (63.59 kJ/m²) demonstrating improved resistance to UV exposure over time. This could be attributed to the redistribution of stress and better fiber-matrix interaction in hybrid systems, which helps mitigate further UV-induced damage [20].

Energy absorption values followed a similar pattern of recovery. P1 showed slight improvement to 1.49 J, while the hybrids H1 and H2 absorbed 2.3 J and 1.93 J, respectively. This suggests that the aramid layers within the hybrid configurations slow down the degradation process caused by prolonged UV exposure.

The notchwise Charpy impact test results provide a more detailed understanding of the fracture resistance of the composites under UV aging. These results further highlight the protective effects of hybridization. Notchwise impact test results are given numerically in Table 3.

Table 2. Flatwise Impact Properties of Samples

FLATWISE IMPACT TEST (Impact Strength kJ/m2)											
P1			**H1**			**H2**			**P2**		
P1-0	P1-450	P1-900	H1-0	H1-450	H1-900	H2-0	H2-450	H2-900	P2-0	P2-450	P2-900
65.77	42.51	54.02	108.54	77.04	90.01	81.26	58.36	63.59	95.63	62.97	66.82
FLATWISE IMPACT TEST (Absorbed Energy (J)											
P1			**H1**			**H2**			**P2**		
P1-0	P1-450	P1-900	H1-0	H1-450	H1-900	H2-0	H2-450	H2-900	P2-0	P2-450	P2-900
1.55	1.31	1.49	2.7	1.96	2.3	2.2	1.73	1.93	3.2	2.02	2.25

Table 3. Notchwise Impact Properties of Samples

NOTCHWISE IMPACT TEST (Impact Strength kJ/m^2)											
P1			**H1**			**H2**			**P2**		
P1-0	P1-450	P1-900	H1-0	H1-450	H1-900	H2-0	H2-450	H2-900	P2-0	P2-450	P2-900
115.69	64.08	71.8	127.95	102.68	114.44	148.56	88.4	93.65	155.04	119.07	141.39
NOTCHWISE IMPACT TEST (Absorbed Energy (J)											
P1			**H1**			**H2**			**P2**		
P1-0	P1-450	P1-900	H1-0	H1-450	H1-900	H2-0	H2-450	H2-900	P2-0	P2-450	P2-900
2.9	2.3	2.52	3.1	2.9	2.95	3.6	2.37	3	4.8	3.57	4.07

The control group results for notchwise impact strength were significantly higher than flatwise, with P2 (entirely aramid) achieving the highest value (155.04 kJ/m²), followed by H2 (148.56 kJ/m²), H1 (127.95 kJ/m²), and P1 (115.69 kJ/m²). This indicates that both aramid-based composites (P2 and H2) excel in notchwise impact resistance due to the superior toughness of aramid fibers. In terms of energy absorption, P2 once again demonstrated the highest energy absorption (4.8 J), followed by H2 (3.6 J) and H1 (3.1 J). These results suggest that aramid layers in hybrid or pure form are critical in enhancing impact toughness. Similar to the flatwise results, notchwise impact strength decreased across all configurations after 450 hours of UV exposure. P1 exhibited the sharpest decline (from 115.69 kJ/m² to 64.08 kJ/m², a 44.61% reduction), indicating significant UV-induced degradation in glass-based composites. H1 and H2 showed better retention of notchwise impact strength, with reductions to 102.68 kJ/m² and 88.4 kJ/m², respectively. The smaller reductions in the hybrid configurations emphasize their better durability under UV exposure.

Energy absorption also dropped, with P1 absorbing 2.3 J after 450 hours of UV aging (a 20.69% decrease). H1 (2.9 J) and H2 (2.37 J) displayed greater resilience, confirming that hybrid composites exhibit better energy absorption retention under UV aging.

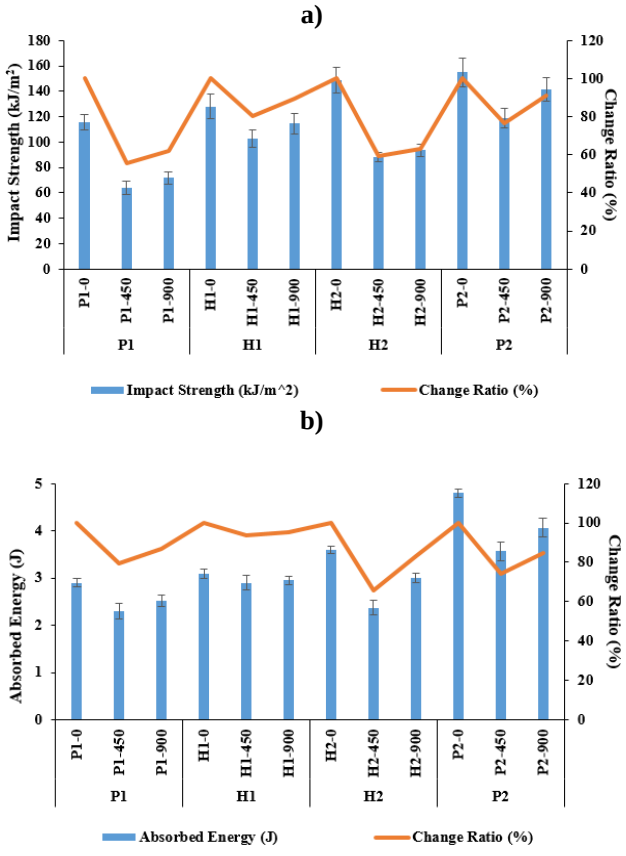

Figure 5. Notchwise Charpy Impact Test Graph a) Impact Strength b) Absorbed Energy

After 900 hours, the notchwise impact strengths showed slight improvements compared to the 450-hour results. P1 increased to 71.8 kJ/m², indicating some recovery, but this value still reflects significant UV-induced damage. Both hybrid composites, H1 (114.44 kJ/m²) and H2 (93.65 kJ/m²), demonstrated relatively stable performance, showing that the incorporation of aramid and glass layers helps reduce the long-term effects of UV exposure.

Energy absorption similarly recovered, with P1 absorbing 2.52 J, while H1 and H2 absorbed 2.95 J and 3.0 J, respectively. This trend suggests that hybridization offers not only better mechanical stability but also enhanced energy absorption capabilities over prolonged UV exposure [15,25].

In interpreting the observed changes in impact properties after 450 and 900 hours of UV aging, it is important to carefully consider the complex degradation and recovery mechanisms at play, while also acknowledging the overall decline in impact performance relative to the initial (0 hours) condition.

The significant decrease in impact strength and energy absorption after 450 hours of UV exposure can be primarily attributed to photooxidation [21,22] of the matrix and fibers, especially in the composites containing glass fibers (P1 and the hybrid groups). Prolonged exposure to UV radiation causes the breakdown of polymer chains in the epoxy matrix, leading to embrittlement and micro-cracking on the surface. These cracks weaken the matrix's ability to effectively transfer stress to the reinforcing fibers during impact, resulting in reduced impact strength.

Additionally, during the initial stages of UV exposure, fiber-matrix interface degradation occurs [23]. The epoxy matrix begins to lose its ability to bond with the reinforcing fibers, especially in glass fiber-dominant composites like P1, where this interface weakening leads to higher vulnerability to UV degradation. This effect was particularly pronounced in the notchwise tests, where the introduction of stress concentrators like notches can exacerbate the impact of UV-induced surface degradation, leading to sharp reductions in impact strength.

Interestingly, after 900 hours of UV aging, there is a partial recovery or stabilization in impact properties compared to the 450-hour results. This recovery can be attributed to reorientation of the matrix and fibers [14,15]. As the UV exposure continues, the surface degradation might slow down, and the material could experience some internal reorganization, such as localized stress relaxation or improved fiber-matrix bonding in areas that have been less affected by surface-level damage [21,24]. This may allow the material to better distribute impact loads, temporarily improving its impact properties.

Despite the partial recovery observed after 900 hours, it is crucial to recognize that the impact properties of all composite groups still show an overall decline compared to the 0-hour condition. This general decrease is indicative of permanent damage caused by UV exposure that cannot be fully reversed by internal reorganization or crystallization. The UV-induced breakdown of the matrix, combined with the weakening of the fiber-matrix interface, results in long-term degradation that reduces the material's ability to withstand impact loads effectively.

4. Conclusion

In this study the effects of UV aging and hybridization on the impact properties of composite plates manufactured using glass and aramid fabrics in four different configurations: pure glass/epoxy (P1), pure aramid/epoxy (P2), glass/aramid/glass (H1), and aramid/glass/aramid (H2) was investigated experimentally. The composites were subjected to UV aging for 0, 450, and 900 hours, and their impact properties were evaluated through flatwise and notchwise Charpy impact tests. The results revealed significant insights into how UV exposure and hybridization influence the durability of these composites. UV aging resulted in a notable reduction in both impact strength and energy absorption across all configurations, particularly after 450 hours of exposure. This decrease was attributed to photooxidation of the epoxy matrix, leading to surface embrittlement and weakened fiber-matrix interactions. After 900 hours of UV exposure, a partial recovery in impact properties was observed, likely due to internal matrix reorganization. However, despite this recovery, the overall impact properties remained lower than the initial (0 hours) condition, indicating permanent UV-induced damage. Despite the partial recovery after 900 hours, all composites showed an overall decline in impact properties compared to their unaged (0 hours) state. Based on the results and analysis in this study, UV aging significantly impacts the impact properties of both hybrid and non-hybrid polymer-based composite materials. Exposure to UV radiation for both 450 and 900 hours led to measurable declines in impact strength and energy absorption, with more pronounced degradation observed after 450 hours. Specifically, non-hybrid samples, such as the glass/epoxy (P1), exhibited the highest susceptibility to UV-induced damage, with flatwise impact strength decreasing by 35.37% after 450 hours. Hybrid composites, especially those with aramid fibers (H1 and H2), demonstrated greater resilience, showing reductions in flatwise impact strength of only 29% and 28.18%, respectively, highlighting the protective role of aramid fibers against UV degradation.

After 900 hours of UV exposure, a slight recovery in impact properties was observed across all configurations, potentially due to matrix reorganization and stress relaxation within the composites. Despite this partial recovery, all UV-aged samples maintained lower impact strength and energy absorption values than their non-aged counterparts, underscoring the irreversible effects of UV exposure. For example, the flatwise impact strength of the glass/epoxy configuration (P1) declined by 17.87% relative to the control, whereas the glass-aramid-glass hybrid (H1) and the aramid-glass-aramid hybrid (H2) configurations showed reductions of 17.07% and 21.75%, respectively. These findings emphasize the durability limitations imposed by UV aging on epoxy-based composites and support the conclusion that hybridization, particularly with aramid fibers, enhances UV resistance. This study provides valuable insights for applications requiring long-term UV exposure, highlighting hybrid composites as more robust options for impact-resistant applications in UV-intensive environments.

Declaration

The author(s) declared no potential conflicts of interest with respect to the research, authorship, and/or publication of this article. The author(s) also declared that this article is original, was prepared in accordance with international publication and research ethics, and ethical committee permission or any special permission is not required.

Author Contributions

Zeynal Abidin OĞUZ: Investigation, Methodology, Writing- Original draft preparation, Reviewing and Editing.

Acknowledgement

This study did not receive any funding or support from any institution or organization.

References

1. Oğuz, Z.A., A. Erkliğ, *Water absorption parameters of glass/epoxy composites based on dimension effect.* International Advanced Research and Engineering Journal, 2021. **5**(2): p. 202-208.
2. Erkek, B., E. Kösedağ, H. Adin, *Hybridization effect on energy absorption capacity of composite crash boxes.* Polymer Composites, 2024. **45**(3): p. 12349-12361.
3. Özbek, Ö., *Axial and lateral buckling analysis of kevlar/epoxy fiber-reinforced composite laminates incorporating silica nanoparticles.* Polymer Composites, 2021. **42**(3): p. 1109-1122.
4. Özbek, Ö., M. Bulut, A. Erkliğ, Ö.Y. Bozkurt, *Interlaminar shear strength and failure analysis of composite laminates with double and triple hybrid configurations.* Engineering Structures, 2022. **265**: 114498.
5. Demircan, G., M. Kısa, M. Özen, B. Aktaş, *Surface-modified alumina nanoparticles-filled aramid fiber-*

reinforced epoxy nanocomposites: preparation and mechanical properties. Iranian Polymer Journal, 2020. **29**(3): p. 253-264.

6. Ni, K., Q. Chen, J. Wen, Y. Cai, Z. Zhu, X. Li, *Low-velocity impact and post-impact compression properties of carbon/glass hybrid yacht composite materials.* Ocean Engineering, 2024. **292**, 116448.
7. Thirugnanasamabandam, A., R. Nallamuthu, *Characteristic investigation of carbon/ceramic-based functionally graded multilayered composite materials.* Journal of Materials Research, 2024. **39**: p. 2176-2187.
8. Özbek, Ö., Z.A. Oğuz, Ö.Y. Bozkurt, A. Erkliğ, *Crashworthiness characteristics of hydrothermally aged intraply glass/basalt composite pipes.* Marine Structures, 2024. **97**: 103656.
9. Oğuz, Z.A., Ö. Özbek, A. Erkliğ, Ö.Y. Bozkurt, *Hydrothermal aging effect on crushing characteristics of intraply hybrid composite pipes.* Engineering Structures, 2023. **297**: 117011.
10. Demirbaş, M.D., Z. Erdoğan, *Effect of UV aging on the thermo-mechanical properties of C-B-A and G-B-A hybrid composites: A study using TMA.* Mechanics of Advanced Materials and Structures, 2024. **31**(1): p. 202-209.
11. Ovalı, S., E. Sancak, *Investigating the effect of the aging process on LDPE composites with UV protective additives.* Journal of Thermoplastic Composite Materials. 2022. **35**(11): 1921-1939.
12. Fiore, V., D. Scalici, D. Basagliacco, D. Enea, G. Alamio, A. Valanza, *Aging resistance of bio-epoxy jute-basalt hybrid composites as novel multilayer structures for cladding.* Composite Structures, 2017. **160**: p. 1379-1328.
13. Mayandi, K., N. Rajini, Nadir Ayrilmis, M.P. Indira Devi, Suchart Siengchin, Faruq Mohammad, Hamad A. Al-Lohedan, *An overview of endurance and ageing performance under various environmental conditions of hybrid polymer composites.* Journal of Materials Research and Technology, 2020. **9**(6): 15962-15988.
14. Silva, A.O., K.G.C. Monsores, S.S.A Oliveira, R.P. Weber, S.N. Monteiro, *Ballistic behavior of a hybrid composite reinforced with curaua and aramid fabric subjected to ultraviolet radiation.* Journal of Materials Research and Technology, 2018. **7**(4): 584-591.
15. Gualberto, H.R., J.M.L. Resis, M.C. Andrade, H.R.M. Costa, F.C. Amorim, J.D. Hunt, *Effect of Exposure Time to UV Radiation on Mechanical Properties of Glass/Epoxy Composites.* Applied Composite Materials, 2024. **31**: 447-465.
16. Nicholas, J., M. Mohamed, G.S. Dhaliwal, S. Anandan, K. Chandrashekhara, *Effects of accelerated environmental aging on glass fiber reinforced thermoset polyurethane composites.* Composites Part B, 2016. **94**: 370-378.
17. Uddin, M.N., J. M. George, V. R. Patlolla, R. Asmatulu, *Investigating the effects of UV light and moisture ingression on low-impact resistance of three different carbon fiber-reinforced composites.* Advanced Composites and Hybrid Materials, 2019. **2**: 701-710.
18. Barvarz, M.G., C. Duchesne and D. Rodrigue, *Mechanical, water absorption, and aging properties of polypropylene/flax/glass fiber hybrid composites.* Journal of Composite Materials, 2015. **49**(30): 3781-3798.
19. ASTM G154 Standard Practice for Operating Fluorescent Light Apparatus for UV Exposure of Nonmetallic Materials.
20. Silva, A.O., K.G.C. Monsores, S.S.A Oliveira, R.P. Weber, S.N. Monteiro, *Influence of gamma and ultraviolet radiation on the mechanical behavior of a hybrid polyester composite reinforced with curaua mat and aramid fabric.* Journal of Materials Research and Technology, 2020. **9**(1): p. 394-403
21. Goliszek, M., B. Podkoscielna, O. Sevastyanova, *Investigation of accelerated aging of lignin-containing polymer materials.* International Journal of Biological Macromolecules, 2019. **123**: p. 910-922.
22. Lu, T., E. Solis-Ramos, Y. Yi, *Synergistic environmental degradation of glass reinforced polymer composites.* Polymer Degradation and Stability, 2016. **131**: p. 1-8.
23. Neto, J.S.S., R.A.A. Lima, D. K. K. Cavalcanti, *Effect of chemical treatment on the thermal properties of hybrid natural fiber-reinforced composites.* Journal of Applied Polymer Science, 2019. **136**(10), 47154.
24. Babu, L.K., K. Mishra, R. Singh, *Near-fiber effects of UV irradiation on the fiber-matrix interphase: A combined experimental and numerical investigation.* Materials and Design, 2018.**157**: 294-302.
25. Nasri, K., L. Toubal, E. Loranger, D. Koffi, *Influence of UV irradiation on mechanical properties and drop-weight impact performance of polypropylene biocomposites reinforced with short flax and pine fibers.* Composites Part C, 2022. **9**: 100296.

Available online at www.dergipark.org.tr/en

INTERNATIONAL ADVANCED RESEARCHES and ENGINEERING JOURNAL

Journal homepage: www.dergipark.org.tr/en/pub/iarej

e-ISSN: 2618-575X

International Open Access

Volume 09
Issue 01

April, 2025

Research Article

Study of synthesis, structure and temperature-dependent phase evolution of Barium Zirconium Titanate

***Pelin Sözen Aktaş*[a,*]**

[a]*Manisa Celal Bayar University, Faculty of Engineering and Natural Sciences, Department of Chemistry, Şehit Prof. Dr. İlhan Varank Campus, Muradiye-Manisa, 45140, Türkiye*

ARTICLE INFO

Article history:
Received 14 November 2024
Accepted 11 April 2025
Published 23 April 2025

Keywords:
Barium zirconium titanate
Organic titanate
Pechini
X-ray diffraction

ABSTRACT

In this study, Barium Zirconium Titanate ($BaZr_xTi_{1-x}O_3$) (where x=0.1 and 0.2) structures were synthesized using starting materials of barium acetate, titanium (triethanolaminato) isopropoxide (80% w/w in isopropanol), and Zr(IV)propoxide (70% 1-propanol solution) through the Pechini method. The significance of this synthesis lies in its novel application of commercially available, air-stable organic titanate precursors. The BZT structures were characterized using X-ray diffraction (XRD), Fourier Transform Infrared spectroscopy (FT-IR), Thermal Gravimetric Analysis (TGA), and Scanning Electron Microscopy with Energy Dispersive X-ray (SEM-EDX) analyses. XRD patterns of the resultant samples, taken after calcination processes at temperatures ranging from 800°C to 1200 °C, support the hypothesis that zirconium is integrated into the structure. SEM results demonstrated that as the amount of Zr increased, the grain size of BZT decreased, with BZT2 particles exhibiting a spherical morphology. The grain sizes of the BZT2 sample ranged approximately from 180 to 50 nm. Furthermore, EDX analyses confirmed the substitution of Zr within the BZT structure.

1. Introduction

The remarkable optical and electrical properties of lead-based perovskites have attained great success, but the instability and toxicity of Pb-based perovskites keep them out of commercial applications. This concern for environmental safety has significantly shifted towards lead-free materials.

Barium titanate is recognized as the most prominent and environmentally friendly ferroelectric ceramic within the perovskite family. Among the most appealing systems derived from this perovskite family are barium zirconium titanate, barium strontium titanate, and dopped metals of BT systems.

Barium zirconate titanate systems (BZT) are among the most significant of these, and they are noted for their extensive applications in the production of energy-consuming devices in areas such as electronics and communications. By focusing on lead-free materials like BZT, we can contribute to the global effort for environmental safety. [1-4]. Barium zirconium titanates are recognized as excellent materials for dielectrics used in industrial micro-electro-mechanical systems, capacitors, and dynamic random-access memory systems. [5, 6]. BZT ceramic materials are commonly expected to be promising for piezoelectric actuators and sensors [7]. BZT systems originated from barium titanate (BT) and barium zirconate (BZ) lattices, where zirconium replacements to titanium lattices have been stated to enhance dielectric and piezoelectric properties [8-11]. The replacement of Ti^{4+} by stable and large cations like Zr^{4+} leads to the diffuse phase transition. It has been stated that Zr^{4+} substitution in the Ti^{4+} region is a helpful way to lower the Curie temperature. Compared to Ti^{4+}, the Zr^{4+} ion is larger and is more stable. By replacing titanium(IV) with zirconium(IV), the perovskite lattice becomes more expansive, and the leakage current is reduced because of electron jumping between Ti^{4+} and Ti^{3+} [12, 13]. The substitution of Zr^{4+} ions significantly improves the basic properties of barium titanate [14]. Barium Zirconium Titanate (BZT) ceramics have outstanding dielectric properties, including improved leakage current, low dielectric loss, dielectric constant, and lowered transition temperature. These features of BZT open various potential applications, from actuators and

* Corresponding author. Tel.:+90-236-201-3182; Fax: +90-236-201-2020.
E-mail addresses: pelin.sozen@cbu.edu.tr *(P. Sözen Aktaş)*
ORCID: 0000-0003-2140-2650 *(P. Sözen Aktaş)*
DOI: 10.35860/iarej.1585507

capacitors to sensors, tunable microwave devices, and antennas. The promising properties of BZT suggest a bright future for its use in various electronic and communication devices. [3, 9, 15, 16]. However, while the product is being developed, obtaining a homogeneous, fine particle-size material should be at the forefront. Under common preparation conditions, these materials usually have heating, calcining, and sintering at high temperatures [11]. To date, many techniques have been developed for synthesizing barium zirconium titanates. These synthesis techniques are divided into three groups: solid state, liquid state, and gas state. While solid-state methods are used for bulk material synthesis, liquid-state techniques have gained importance for nanomaterial production [17].

Barium zirconium titanate is traditionally synthesized through a solid-state reaction involving barium carbonate, titanium(IV) oxide, and zirconium(IV) oxide at elevated temperatures [18, 19]. This conventional approach is inadequate because of issues related to the milling process and contamination during the sintering and calcination stages. Liquid state techniques frequently used in synthesizing barium zirconium titanate are solid state, auto-combustion, sol-gel, Pechini, and co-precipitation [20-23]. Among these, the Pechini method is preferred due to its simplicity, homogeneous distribution, complex oxide, and nanometric product formation [10, 24, 25]. In the previous investigation, the synthesis of nano-scale round-shaped barium titanate via the Pechini technique using an organic titanate complex of triethanolaminato was reported by Aktaş [26].

This study concentrates on synthesizing homogeneous BZT structures at reduced temperatures, employing stable precursor materials, including barium acetate, zirconium propoxide, and an organic titanium complex. Furthermore, the use of Ti(IV) (triethanolaminato) isopropoxide as a starting material for synthesizing TiO_2, $BaTiO_3$, and metal titanates has been documented in a limited number of studies. [27-30]. Upadhyay and co-workers prepared spherical and cubic nanoparticles of $BaTiO_3$ via Ti-triethanolamine isopropoxide and barium hydroxide in MeOH solution [27]. As an alternative to metallic alkoxides, using metal complexes in liquid-phase reactions allows for obtaining nano-scale structures. In the present work, ($BaZr_xTi_{1-x}O_3$) (x=0.1 (BZT1), x=0.2 BZT2) structures were synthesized via the Pechini technique. However, no literature has been published on synthesizing BZT with a titanium triethanolaminato complex.

The primary advantage of this synthesis lies in its unique utilization of a commercially available, air-stable organic titanate precursor, marking a significant advancement in the field. The characterization and phase formation of the prepared BZT1 and BZT2 samples are elucidated through TGA, FTIR, XRD, and SEM analyses. The structural properties and morphology of the samples are also studied. The results obtained from XRD and SEM indicated a correlated increase in mole fraction, influenced by higher calcination temperatures and reduced grain size.

2. Experimental

2.1 Materials and Method

Barium acetate; ($Ba(CH_3COO)_2$, 99 %, Sigma-Aldrich), Zirconium(IV)propoxide solution ($Zr(OCH_2CH_2CH_3)_4$, 70 wt.% in 1-propanol, Aldrich), titanium (triethanolaminato) isopropoxide solution (80 wt.% in isopropanol, Sigma Aldrich), citric acid ($C_6H_8O_7$, ≥ 99.5%, Sigma-Aldrich), ethylene glycol ($C_2H_6O_2$, 99.8%, Sigma-Aldrich) and were used as starting materials. The BZT powders were characterized utilizing X-ray diffraction (XRD) with a PANalytical Empyrean diffractometer operating within a 2θ range of 10 ° to 80 °, at a scan speed of 0.05 ° s^{-1}, employing λ = 1.5406 Å Cu Kα radiation. The phase identification was conducted using the Match! Program (Version 3, Crystal Impact). [31]. The FT-IR spectra of the powders were obtained using an FT-IR spectrometer (Spectrum BX Perkin Elmer), scanning from 4000 cm-1 to 400 cm-1 with the KBr disc method. The Spectragryph Software for Optical Spectroscopy Version 1.2.16.1 was examined for spectrum graphs. [32]. TGA analysis instrument SII 7300 Perkin Elmer thermal analyzer was used to understand the thermal stability of samples. A Zeiss Gemini 500 microscope was employed to analyze the morphology of the BZT structure. The analysis of the elemental composition of the BZT samples was conducted utilizing EDX.

2.2 Synthesis of Barium Zirconium Titanate samples

$Ba(Zr_{0.1}Ti_{0.9})O_3$ (BZT1) and $Ba(Zr_{0.2}Ti_{0.8})O_3$ (BZT2) samples were synthesized using the Pechini technique. The experimental pathway is presented in Figure 1.

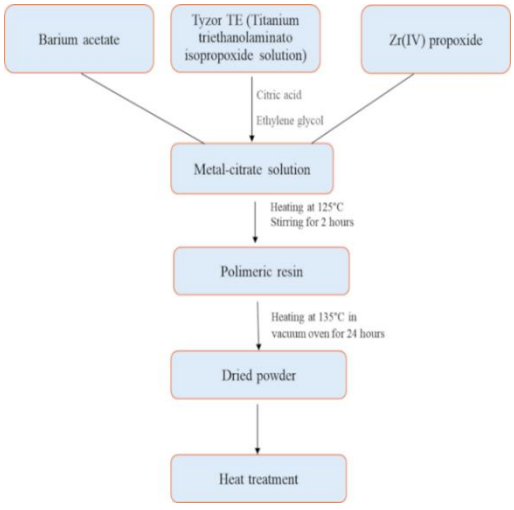

Figure 1. Synthesis pathway of BZT powders using the Pechini method.

The synthesis procedure is given for $Ba(Zr_{0.1}Ti_{0.9})O_3$ (BZT1). In the first stage, the metallic citrate solutions were prepared using barium acetate (4.0g, 15.66mmol), titanium(IV) (triethanolaminato) isopropoxide (4.45 g, 14.09 mmol), Zr(IV)propoxide (in 70 % 1-propanol, 0.7 mL, 1.56 mmol), citric acid (13.53 g, 70 mmol) and ethylene glycol (17.46 mL, 313.2 mmol). The molar ratio is Ba/ $(Zr_{0.1}Ti_{0.9})$/ citric acid/ ethylene glycol = 1/ 1/ 4.5/ 20. The solution was maintained at 125 °C for 2 hours to produce a clear, pale-yellow gel. Subsequently, this gel was heated at 135 °C in a vacuum oven for 24 hours. The resulting powder underwent a two-step heating process: initially, it was treated at 400 °C for 4 hours to eliminate organic residues, followed by treatment at temperatures ranging from 800 to 1200 °C for an additional 4 hours at a heating rate of 5 °C per minute, before being allowed to cool to room temperature. The synthesis of $Ba(Zr_{0.2}Ti_{0.8})O_3$ (BZT2) was prepared in the same pathway using the appropriate stoichiometric ratio.

3. Results and Discussion

3.1 TGA and FTIR Analysis

The thermal analysis of the BZT1 precursor, which was acquired at a temperature of 135 °C and subsequently dried, was conducted using TGA with a heating rate of 10 °C per minute, extending to a maximum temperature of 1400 °C. The TGA curve for BZT1 (refer to Figure 2) indicates an initial mass loss of 9% within the temperature range of 25 °C to 200 °C, which is attributable to the moisture and volatiles adsorbed by the sample [33]. The subsequent mass loss observed between 200 °C and 550 °C is associated with the dehydration of organic molecules [23]. Ultimately, in the temperature range of 1050 °C to 1400 °C, the weight of the powder remains relatively stable. Following calcination at 1050 °C, a residue comprising 16.5% was obtained. A comparable scenario is evident in the TGA curve for BZT2 (as illustrated in Figure 2), where the weight of the powder also remains nearly constant between 1060 °C and 1400 °C. Notably, after calcination at 1060 °C, the residue for BZT2 was approximately 14%.

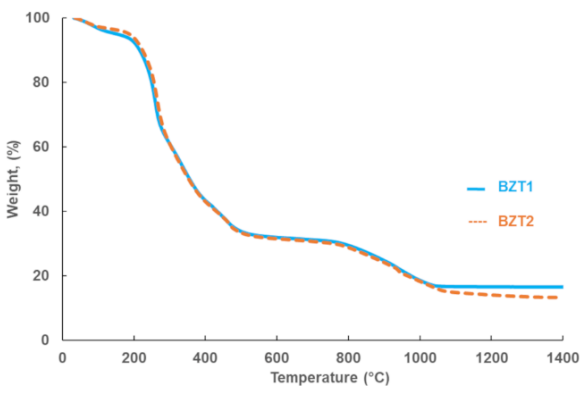

Figure 2. TGA plot of as-prepared BZT1 and BZT2 precursors.

The FTIR analyses were employed to determine the vibration peaks of zirconium and titanium oxygen bonds. Figure 3 illustrates the FT-IR spectrum of the BZT powders calcined at 1200 °C. In the FTIR spectrum of BZT1 and BZT2, the vibration bands between 500-600 cm^{-1} can be assigned to Ti-O and Zr-O stretching vibrations [34]. The absorption bands at 574 cm^{-1} and 531 cm^{-1} are assigned to Ti-O and Zr-O vibration bands of MO_6 (M=Ti or Zr) in BZT2. In BZT1, with a smaller amount of Zr doped, a single broad stretching vibration peak was observed at 537 cm^{-1}.

3.2 XRD Analysis and Temperature-dependent Phase Evolution

In this study, the structure of Zr-substituted BT has been investigated to understand the structural shift by adding Zr in BT. The resulting powder sample was heated at 5 °C/min at calcination temperatures of 800°C to 1200 °C. The XRD pattern of BZT1 powder obtained by the Pechini method at 800 °C is shown in Figure 4. $BaCO_3$ was typically observed due to the open-air system. The peaks were observed for the BT, BZ, and Zr-doped BZT samples at 800 °C.

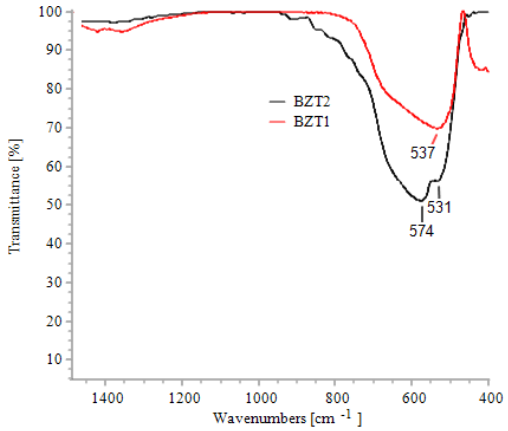

Figure 3. FTIR spectrum of BZT1 and BZT2 samples prepared at 1200 °C.

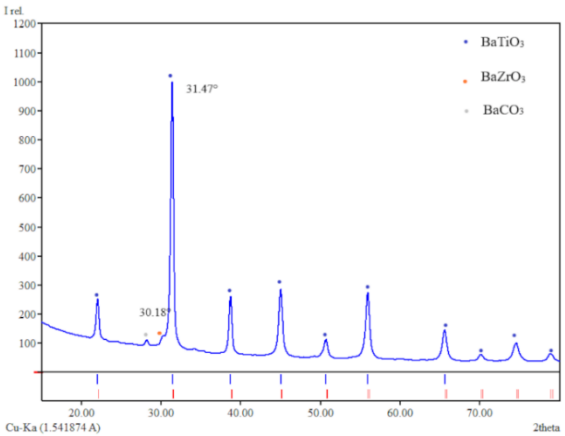

Figure 4. XRD pattern of $BaZr_{0.1}Ti_{0.9}O_3$ sample calcined at 800 °C. (JCPDS no.79-2263 $BaTiO_3$ (BT), JCPDS no. 74-1299 $BaZrO_3$ (BZ))

Due to the inability of Zirconium to diffuse, it is imperative to elevate the calcination temperature to attain a greater Zr content. Consequently, a single phase was successfully achieved at elevated temperatures of 900°C, 1000 °C, and 1200 °C, as illustrated in Figures 5 and Figure 6. BZT1 and BZT2 were obtained at 1000 °C and 1200 °C respectively. The diffraction peaks of BZT1 and BZT2 exhibit a shift towards lower angles, while the full width at half maximum (FWHM) of the XRD peaks increases with the augmentation of zirconium content. At BZT2, the reflection peaks shifted towards lower 2θ, suggesting that the Zr^{4+} ion is substituted to the Ti-site. The shift of 110 diffraction peak values for BZT1 and BZT2 are given in Table 1.

Table 1. The shift of 110 peaks is a result of the temperature variation.

	800 °C	900 °C	1000 °C	1200 °C
BZ	30.29	30.19	-	-
BT	31.41	31.48	-	-
BZT1	-	-	30.77	31.29
BZ	30.26	30.24	-	-
BT	31.41	31.38	-	-
BZT2	-		31.19	31.19

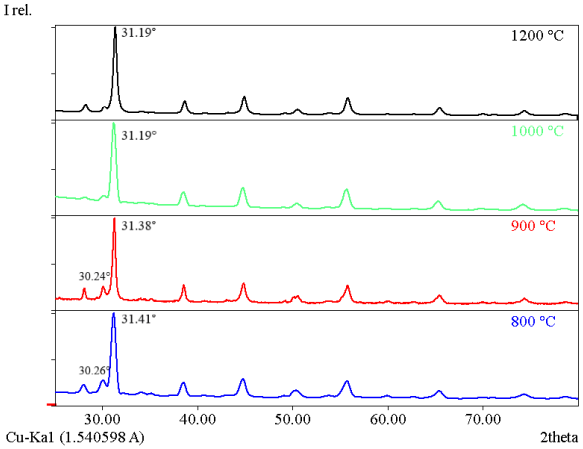

Figure 5. XRD patterns of BZT1 powder after calcination at 800°, 900°C, 1000° C and 1200° C.

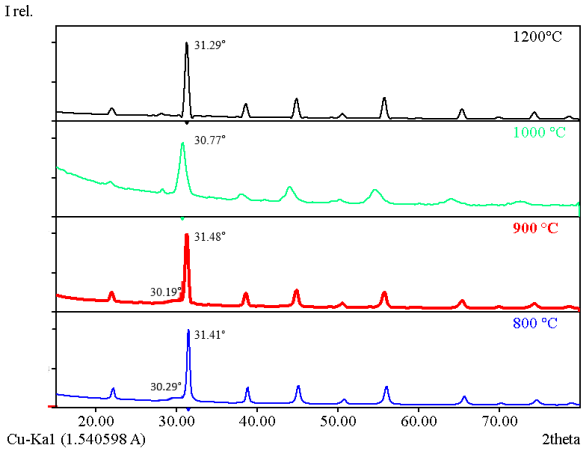

Figure 6. XRD patterns of BZT2 powder after calcination at 800°, 900°C, 1000° C and 1200° C.

3.3 EDX and SEM Analysis

EDX analysis was conducted on Barium Zirconate Titanate (BZT) samples to elucidate their chemical composition. The resulting spectrum indicates the presence of the element's barium, zirconium, titanium, and oxygen. It was observed that the percentage elemental values closely corresponded to both the calculated and experimental values. The EDX analysis, as illustrated in Figure 7, demonstrates that the obtained BZT powders were nearly identical to the intended stoichiometry during preparation, and no traces of any extraneous elements were detected.

SEM images of BZT1 and BZT2 are presented in Figure 8. This figure illustrates the microstructures of the BZT1 and BZT2 samples that have been calcined at 1200 °C. It is evident that zirconium substitutions significantly influence the morphology and grain size of the samples. Observations indicate that the average grain sizes decrease from 200-120 nm to 180-50 nm as the Zr fraction is increased. Similar findings were reported by Reda and colleagues [35]. The reduction in grain size can be ascribed to a decreased grain growth rate during calcination, which results from the slow atomic diffusion of Zr ions. The grain morphology of the BZT1 samples transforms from blocky and various pentagonal and partially irregular shapes to more rounded configurations, as evidenced in the structure of BZT2.

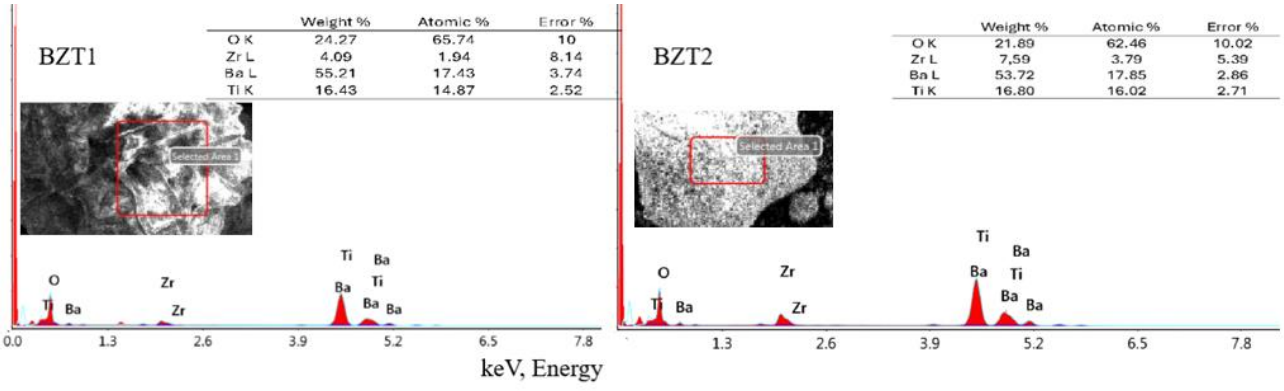

Figure 7. EDX spectrum of BZT1 and BZT2 samples calcined at 1200 °C

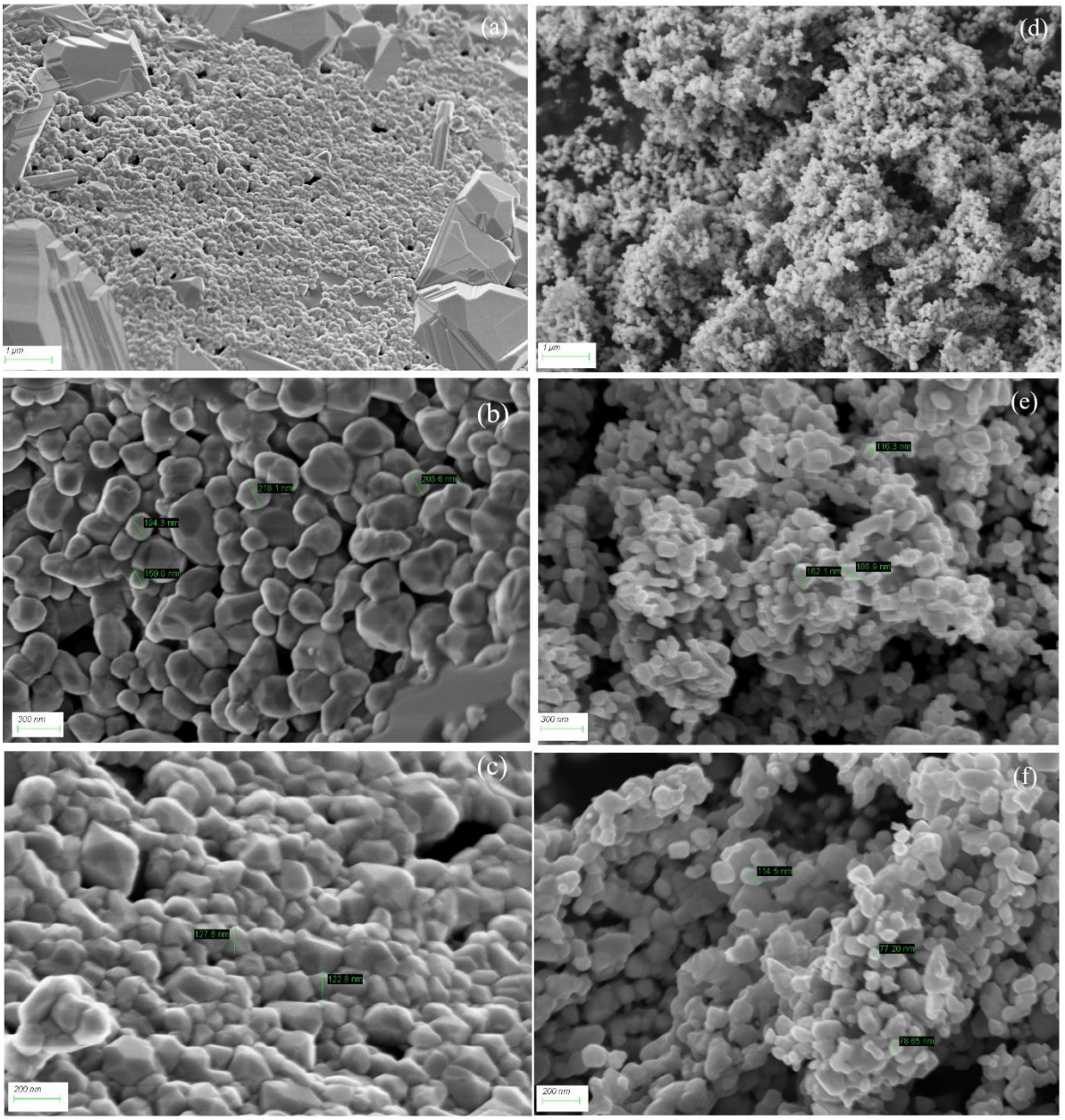

Figure 8. The SEM micrograph of BZT1 (a, b, c) and BZT2 (d, e, f) samples calcined at 1200 °C.

4. Conclusion

In the present study, barium zirconium titanates ($BaZr_xTi_{1-x}$, where x = 0.1, 0.2) with varying zirconium contents were synthesized utilizing the Pechini method. The titanium source employed was titanium (triethanolaminato) isopropoxide, noted for its stability in atmospheric conditions, economic viability, and commercial availability. This precursor offers several advantages over other titanium sources, including titanium chloride or propoxide, typically employed in liquid-phase synthesis methods.

The phase evolution is monitored through XRD measurements, and the results confirm establishing a single BZT form at temperatures exceeding 1000°C. The calcination of samples at 1200°C allowed the Zr^{+4} ions to diffuse into the lattice structure of barium titanate. The results from XRD and SEM indicated a rise in mole fraction, which is influenced by the elevated calcination temperature and the reduction in grain size. Also, XRD results demonstrated Zr ions successfully incorporated into lattice structure as confirmed by shifts at 2θ. It is observed that the average grain size decreased from 200-120 nm for BZT1 to 180-50 nm for BZT2 with increasing the Zr fraction.

Declaration

The author confirmed no potential conflicts of interest related to this research, authorship, or publication. Additionally, the author indicated that this article is original and was prepared in accordance with international publication and research ethics; no ethical committee permission or special approval is necessary.

Author Contributions

P. Sözen Aktaş developed the manuscript's conceptualization, methodology, validation, and presentation.

Acknowledgment

The author acknowledged support from the Manisa Celal Bayar University Research Projects Commission. (Project number: 2019-056).

References

1. Qiu, J.H., T.X. Zhao, Z.H. Chen, X.Q. Wang, N.Y. Yuan, and J.N. Ding, *Phase diagram and physical properties of (110) oriented $Ba(Zr_{0.08}Ti_{0.92})O_3$ thin film.* Solid State Communications, 2019. **289**: p. 1–4.
2. Kaur, R., M. Singh, and A. Singh, *Influence of samarium and iron substitution on structural and electrical properties of barium zirconate titanate solid solutions.* Journal of Asian Ceramic Societies, 2019. **7**(3): p. 284–297.
3. Maiti, T., R. Guo, and A.S. Bhalla, *Enhanced electric field tunable dielectric properties of $BaZr_xTi_{1-x}O_3$ relaxor ferroelectrics*. Applied Physics Letters, 2007. **90**(18): p.182901.
4. Delibaş, N. C., S. B. Gharamaleki, M. Mansouri, and A. Niaie, *Reduction of operation temperature in SOFCs utilizing perovskites: Review*, International Advanced Researches and Engineering Journal, 2022. **6**(1): p. 56–67.
5. Ciomaga, C.E., M.T. Buscaglia, M. Viviani, V. Buscaglia, L. Mitoseriu, A. Stancu, P. Nanni, *Preparation and dielectric properties of $BaZr_{0.1}Ti_{0.9}O_3$ ceramics with different grain sizes.* Phase Transitions, 2006. **79**(6–7): p. 389–397.
6. Mangaiyarkkarasi, J., S. Sasikumar, O.V. Saravanan, and R. Saravanan, *Electronic structure and bonding interactions in $Ba_{1-x}Sr_xZr_{0.1}Ti_{0.9}O_3$ ceramics*. Frontiers of Materials Science, 2017. **11**(2): p. 182–189.
7. Dong, L., D.S. Stone, and R.S. Lakes, *Enhanced dielectric and piezoelectric properties of $xBaZrO_3$-(1-x)$BaTiO_3$ ceramics*. Journal of Applied Physics, 2012. **111**(8): p.084107.
8. Fahad, M., R. Thangavel, and P.M. Sarun, *Scaling behavior of the $BaZr_{0.1}Ti_{0.9}O_3$ (BZT) dielectric ceramic at the elevated temperatures (400 °C – 540 °C)*. Materials Science and Engineering B: Solid-State Materials for Advanced Technology, 2022. **283**: p.115837.
9. Bhargavi, G.N., T. Badapanda, M.S. Anwar, M. Tlija, H. Joardar, and S.N. Tripathy, *Understanding the impact of gadolinium substitution on the impedance and conduction mechanism of barium zirconium titanate ceramics.* Journal of Materials Science: Materials in Electronics, 2024. **35**(1991): p. 1-28.
10. Salem, M.M., M.A. Darwish, A.M. Altarawneh, Y.A. Alibwaini, R. Ghazy, O.M. Hemeda, D. Zhou, E.L. Trukhanova, A.V. Trukhanov, S.V. Trukhanov and M. Mostafa, *Investigation of the structure and dielectric properties of doped barium titanates*. RSC Advances, 2024. **14**(5): p. 3335–3345.
11. Kholodkova, A.A., A. V. Reznichenko, A.A. Vasin, and A. V. Smirnov, *Methods for the synthesis of barium titanate as a component of functional dielectric ceramics*. Tonkie Khimicheskie Tekhnologii, 2024. **19**: p. 72–87.
12. Jia, Q., B. Shen, X. Hao, J. Zhai, and X. Yao, *Enhanced dielectric property from highly (100)-oriented barium zirconate titanate compositional gradient films*. Thin Solid Films, 2010. **518**: p. e89–e92.
13. Jha, P.A., and A.K. Jha, *Influence of processing conditions on the grain growth and electrical properties of barium zirconate titanate ferroelectric ceramics*. Journal of Alloys and Compounds, 2012. **513**: p. 580–585.
14. Binhayeeniyi, N., P. Sukvisut, C. Thanachayanont, and S. Muensit, *Physical and electromechanical properties of barium zirconium titanate synthesized at low-sintering temperature.* Materials Letters, 2010. **64**(3): p. 305–308.
15. Liu, L., S. Zheng, Y. Huang, D. Shi, S. Wu, L. Fang, C. Hu, B. Elouadi, *Structure and piezoelectric properties of $(1-0.5x)BaTiO_3$–$0.5x$ $(0.4BaZrO_3$–$0.6CaTiO_3)$ ceramics*. Journal of Physics D: Applied Physics, 2012. **45**(29): p. 295403.
16. Jain, A., A.K. Panwar, and A.K. Jha, *Effect of ZnO doping on structural, dielectric, ferroelectric and piezoelectric properties of $BaZr_{0.1}Ti_{0.9}O_3$ ceramics*. Ceramics International, 2017. **43**(2): p 1948–1955.
17. Kumar, D., R. Sagar Yadav, Monika, A. Kumar Singh, and S. Bahadur Rai, *Synthesis Techniques and Applications of Perovskite Material*. Perovskite Materials, Devices and Integration. 2020, IntechOpen.
18. Islam, S., M. R. Molla, N. Khatun, N. I. Tanvir, M. Hakim and Md. S. Islam, *Exploring the effects of zirconium doping on barium titanate ceramics: structural, electrical, and optical properties.* Material Advances, 2025. **6**: p. 1403-1413.
19. Hao, T., J. Shen, Q. Peng, J. Liu, W. Hu, C. Zhong, *Solid-State Synthesis for High-Tetragonality, Small-Particle Barium Titanate.* Materials, 2024. **17**: p. 5655.
20. Dzunuzovic, A.S., M.M.V. Petrovic, J.D. Bobic, N. I. Ilic and B. D. Stojanovicet, *Influence of ferrite phase on electrical properties of the barium zirconium titanate based multiferroic composites*. Journal of Electroceramics,2021. **46:** p. 57–71.
21. Reddy, S.B., K.P. Rao, and M.S.R. Rao, *Nanocrystalline barium zirconate titanate synthesized at low temperature by an aqueous co-precipitation technique.* Scripta Materialia, 2007. **57**(7): p. 591–594.
22. Deluca, M., C.A. Vasilescu, A.C. Ianculescu, D. C. Berger, C. E. Ciomaga, L. P. Curecheriu, L. Stoleriu, A. Gajovic, L. Mitoseriu, C. Galassi, *Investigation of the composition-dependent properties of BaTi 1-xZr xO 3 ceramics prepared by the modified Pechini method.* Journal of the European Ceramic Society, 2012. **32**(13): p. 3551–3566.
23. Veith, M., S. Mathur, N. Lecerf, V. Huch and T. Decker, Sol-gel synthesis of nano-scaled $BaTiO_3$, $BaZrO_3$ and $BaTi_{0.5}Zr_{0.5}O_3$ oxides via single-source alkoxide precursors and semi-alkoxide routes. Journal of Sol-Gel Science and Technology, 2000. **17**(2): p. 145–158.
24. Yoshimura, M., M. Kakihana, and K. Sardar, *A review on the designing of homogeneous multicomponent oxides via polymer complex method*. Materials and Design, 2024. **244**: p. 113118.
25. Nicollet, C., and A.J. Carrillo, *Back to basics: synthesis of metal oxides*. Journal of Electroceramics, 2023. **52**: p.10-28 .
26. Aktaş, P., *Synthesis and Characterization of Barium Titanate Nanopowders by Pechini Process.* Celal Bayar University Journal of Science, 2020. **16**(3): p. 293-300.

27. Upadhyay, R.H., A.P. Argekar, and R.R. Deshmukh, *Characterization, dielectric and electrical behaviour of $BaTiO_3$ nanoparticles prepared via titanium(IV) triethanolaminato isopropoxide and hydrated barium hydroxide*. Bulletin of Material Sciences, 2014. **37**(3): p.481-489
28. Upadhyay, R.H., and R.R. Deshmukh, *A new low dielectric constant barium titanate - poly (methyl methacrylate) nanocomposite films.* Advances in Materials Research, 2013. **2**(2): p. 99–109.
29. Kong, L., I. Karatchevtseva, M. Blackford, I. Chironi, and G. Triani, *Synthesis and characterization of rutile nanocrystals prepared in aqueous media at low temperature*. Journal of the American Ceramic Society, 2012. **95**(2): p. 816–822.
30. Kong, L., I. Karatchevtseva, R. Holmes, J. Davis, Y. Zhang, and G. Triani, *New synthesis route for lead zirconate titanate powder*. Ceramics International, 2016. **42**(6): p. 6782–6790.
31. Match! - Phase Identification from Powder Diffraction, Crystal Impact - Dr. H. Putz & Dr. K. Brandenburg GbR, Kreuzherrenstr. 102, 53227 Bonn, Germany, http://www.crystalimpact.com/match.
32. F. Menges, Spectragryph-optical spectroscopy software, Version 1.2.16.1., 2022.
33. Bernardi, M.I.B., E. Antonelli, A.B. Lourenço, C.A.C. Feitosa, L.J.Q. Maia, and A.C. Hernandes, *$BaTi_{1-x}Zr_xO_3$ nanopowders prepared by the modified Pechini method.* Journal of Thermal Analysis and Calorimetry, 2007. **87**(3): p. 725–730.
34. Chen, X., X. Chao, and Z. Yang, *Submicron barium calcium zirconium titanate ceramic for energy storage synthesised via the co-precipitation method.* Materials Research Bulletin, 2019. **111**: p. 259–266.
35. Reda, M., S.I. El-Dek, and M.M. Arman, *Improvement of ferroelectric properties via Zr doping in barium titanate nanoparticles*. Journal of Materials Sciences: Materials in Electronics, 2022. **33**: p. 16753–16776.

Available online at www.dergipark.org.tr/en

INTERNATIONAL ADVANCED RESEARCHES
and
ENGINEERING JOURNAL

Journal homepage: www.dergipark.org.tr/en/pub/iarej

e-ISSN: 2618-575X

International Open Access

Volume 09
Issue 01

April, 2025

Review Article

Comprehensive and essential review of advanced researches abrasive waterjet machining

Fuat Kartal [a,*] ***and Arslan Kaptan*** [b]

[a]*Mechanical Engineering Department, Engineering and Architecture Faculty, Kastamonu University, Kastamonu, 37150, Turkey*
[b]*Motor Vehicles and Transportation Technologies Department, Sivas Technical Sciences Vocational School, Sivas Cumhuriyet University, Sivas, 58140, Turkey*

ARTICLE INFO

Article history:
Received 10 November 2024
Accepted 10 April 2025
Published 23 April 2025

Keywords:
Abrasive waterjet machining
Methodologies of AWJ machining
Optimization
Surface roughness

ABSTRACT

Abrasive Waterjet (AWJ) machining is a highly versatile non-conventional manufacturing technology, increasingly adopted across diverse industries due to its capability of processing a wide spectrum of materials, including metals, alloys, ceramics, composites, and polymers. Unlike conventional methods, AWJ utilizes high-pressure water mixed with abrasive particles to remove material by erosion, significantly reducing thermal effects, mechanical distortion, and material degradation. The performance and efficiency of AWJ machining are directly influenced by critical process parameters such as waterjet pressure, traverse speed, abrasive mass flow rate, stand-off distance, and nozzle geometry. Recent studies have shown that optimizing these parameters is essential to enhance surface finish, improve material removal rates, and reduce kerf defects such as taper angles and burr formation. This comprehensive review systematically synthesizes recent advancements and essential findings from the existing literature on AWJ machining. It emphasizes material-specific optimization strategies, explores critical interactions between machining parameters, and summarizes methodologies such as experimental designs, numerical modeling, response surface methodology, and artificial neural networks frequently used to optimize the AWJ process. Particular attention is given to identifying the underlying mechanisms influencing outcomes, such as material erosion phenomena, abrasive particle interactions with the material surface, crack initiation and propagation, as well as abrasive embedment. Furthermore, the review addresses current challenges, including achieving precision machining for hard-to-cut materials like superalloys (e.g., Inconel 718, Ti-6Al-4V) and fiber-reinforced polymer composites, highlighting recent solutions and future research directions. This extended synthesis provides valuable insights and standardized guidelines for industrial practitioners and researchers, facilitating broader adoption and continuous innovation within AWJ machining technology.

1. Introduction

Abrasive Waterjet (AWJ) machining is a prominent non-conventional manufacturing process distinguished by its capability to precisely machine complex, heat-sensitive, and advanced materials without generating substantial thermal stresses or inducing heat-affected zones (HAZ). Over the past decades, extensive research has underscored the importance and effectiveness of AWJ technology for machining applications in diverse industries, including aerospace, automotive, marine, biomedical, and energy sectors.

Numerous studies have examined AWJ processes and their applications across a wide variety of material classes. This includes machining advanced metallic alloys such as titanium (Ti-6Al-4V, gamma titanium aluminide): nickel-based superalloys (Inconel 718): aluminum alloys (AA6061, AA7075, AA2024-T3): and specialized high-strength steels. AWJ machining has also demonstrated excellent applicability in the processing of composites and polymer-based materials such as carbon fiber reinforced plastics (CFRP): Kevlar fiber-reinforced polymers, UHMWPE, wood-plastic composites, PP, PVC-U coated with polyurethane, acrylate coatings, jute-epoxy composites, and aluminum/silicon carbide composites.

The quality and effectiveness of the AWJ machining processes are highly dependent on careful selection and optimization of numerous parameters, which predominantly include waterjet pressure, abrasive mass flow rate, traverse speed, standoff distance, nozzle design

* Corresponding author. Tel.: +90-366-280-1000.
E-mail addresses: fkartal@kastamonu.edu.tr *(F.Kartal)*, akaptan@cumhuriyet.edu.tr *(A.Kaptan)*
ORCID: 0000-0002-2567-9705 *(F. Kartal)*, 0000-0002-2431-9329 *(A. Kaptan)*
DOI: 10.35860/iarej.1582470

and geometry, abrasive particle size and shape, and workpiece properties.

Parametric influences on AWJ machining outcomes are primarily reflected through key performance indicators such as surface roughness, kerf geometry, material removal rate, waviness, dimensional accuracy, surface contamination, grit embedment, and surface integrity.

Recent scientific explorations underline the importance of understanding the underlying mechanisms driving material removal in AWJ machining. Primary mechanisms include abrasive-induced micro-cutting, material erosion, plastic deformation, fracture propagation, brittle fracture, abrasive particle impact, and surface embedding. Detailed comprehension of these mechanisms is vital to explain precisely how selected parameters yield specific machining effects, thus guiding further process optimization and improved performance.

Moreover, extensive research has been dedicated to employing advanced analytical and numerical modeling approaches to simulate AWJ machining processes and predict outcomes more precisely. Techniques like finite element analysis (FEA): artificial neural networks (ANN): regression modeling, and response surface methodology (RSM) have become instrumental in modeling and predicting critical responses, optimizing parameters, and implementing adaptive process control.

Emerging trends also highlight the integration of AWJ with hybrid manufacturing processes, including additive manufacturing, milling, and turning operations, emphasizing their potential to achieve complex geometries, enhance surface quality, and expand the versatility of this machining technique

Considering the comprehensive analysis above, this review systematically assesses the recent advances in AWJ machining with particular emphasis on understanding the precise relationships between operational parameters, resulting effects, and underlying machining mechanisms. Additionally, this review synthesizes insights from an extensive range of contemporary studies, establishing a clear scientific foundation for future investigations, optimization strategies, and innovative AWJ machining applications.

2. Literature Survey

2.1. Materials

Ravi and Srinivasu [1] conducted a detailed parametric study on AWJ trepanation of Al-6061 alloy as shown in Figure 1. The experimental setup focuses on optimizing the process parameters such as water jet pressure, pass velocity and abrasive mass flow rate. They found that higher pressure and mass flow rates at lower speeds improved hole quality by minimizing form error and burr length. Optimal parameters included a pressure of 350 MPa, traverse speed of 50 mm/min, and mass flow rate of 0.55 kg/min, offering valuable insights for precise and high-quality machining of Al-6061.

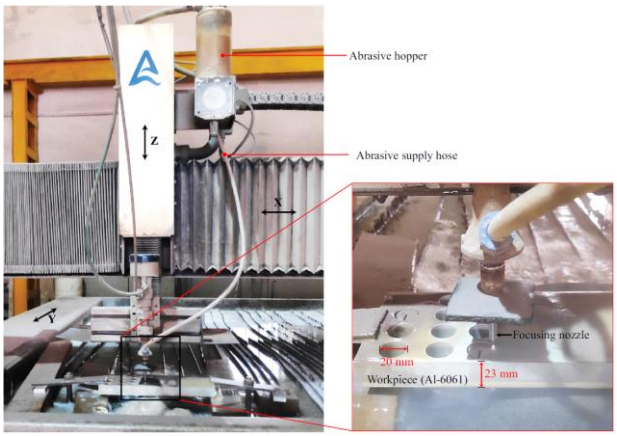

Figure 1. Experimental setup employed for AWJ trepanning [1].

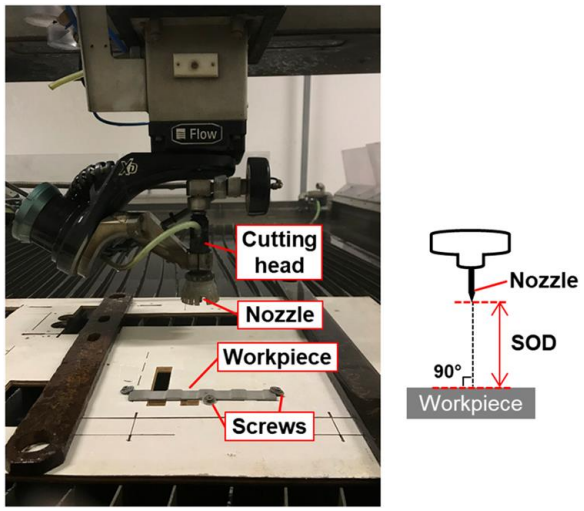

Figure 2. Experimental setup for AWJ and PWJ processes with a schematic showing the SOD process parameter and the impingement angle between the nozzle and the sample [2].

Cano-Salinas et al. [2] investigated AWJ milling of Inconel 718, focusing on finishing by plain waterjet (PWJ) cleaning as seen in Figure 2. Their study revealed that PWJ cleaning could remove up to 80% of embedded grit without altering surface texture or material properties, maintaining mechanical integrity. This combination of AWJ and PWJ proves effective for aerospace applications requiring high surface quality.

Płodzień et al. [3] studied AWJ cutting of Inconel 718, modeling kerf angle, surface roughness, and waviness. They found depth of cut significantly affected roughness and waviness, while sample height influenced kerf angle. Optimizing cutting speed and depth improved surface quality and dimensional accuracy, making AWJ a valuable method for machining high-strength, high-temperature materials.

Sourd et al. [4] examined PWJ cleaning of Ti6Al4V titanium alloy after AWJ milling, highlighting issues with abrasive embedment. They found PWJ cleaning reduced contamination by 65%, but deeply embedded particles remained (Figure 3).

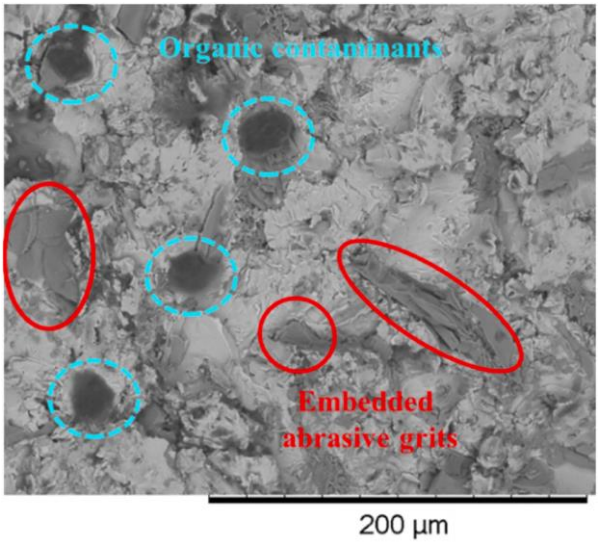

Figure 3. SEM image obtained from sensor in a specimen machined with water pressure of 118 MPa, scan step of 0.5 mm and jet traverse speed of 1 m/min [4].

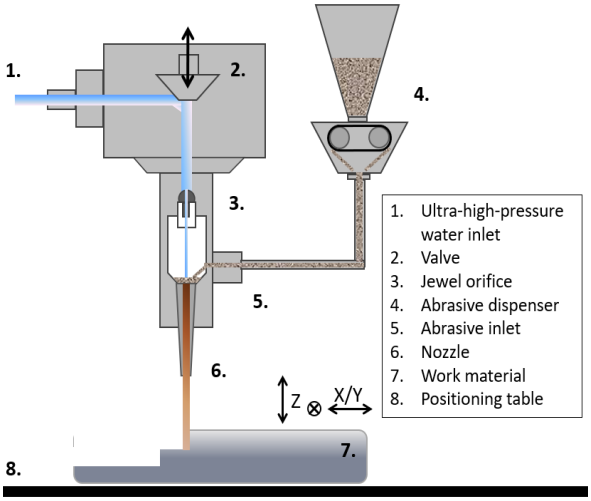

Figure 4. Schematic overview of the AWJ components [5].

Higher AWJ pressures improved cleaning effectiveness, though higher pressures might affect material integrity, suggesting further optimization for high-cleanliness applications.

Holmberg et al. [5] explored AWJ milling for superalloy gas turbine components, focusing on alloy 718 (Figure 4). They concluded AWJ milling effectively competed with semi/finish milling, excelling in machining complex geometries with minimal surface impact. However, post-processing was necessary to achieve surface quality comparable to traditional milling.

Armağan and Arıcı [6] studied AWJ machining of Fe-Cr-C based hardfacing wear plates, emphasizing surface quality and kerf properties. Material alignment direction significantly influenced surface roughness and kerf taper angle, with optimal parameters improving machining efficiency and quality. Detailed morphological analyses provided insights into material removal mechanisms.

Figure 5. UHMWPE plate production flow chart [7].

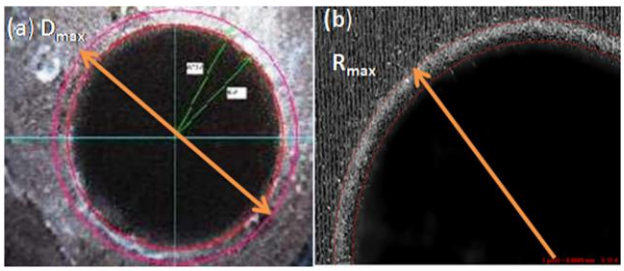

Figure 6. Measurement of maximum damage drilled hole diameter (Dmax): (a) Peel up at the entry hole and (b) Push out at the exithole [8].

Doğankaya et al. [7] investigated AWJ machining of UHMWPE (Figure 5): focusing on optimizing process parameters for trimming, pocketing, and hole-making. Using design of experiments and particle swarm optimization, they achieved a balance between surface roughness and dimensional accuracy. The study demonstrated AWJ's advantages, such as low cost and environmental friendliness, but noted challenges with delamination and dimensional errors.

Ganesan et al. [8] optimized AWJ machining parameters for drilling onyx composites, fabricated via additive manufacturing. They used Taguchi analysis, genetic algorithms, and Moth-Flame Optimization to reduce delamination and surface roughness as seen in Figure 6. Optimal parameters significantly improved machining efficiency and quality, confirming the potential for high-precision component production.

Müller et al. [9] compared AWJ and WJ technologies for cutting PP and PVC-U materials coated with polyurethane and acrylate. AWJ achieved more uniform cuts with fewer burrs. Optimal cutting speeds and scanning electron microscope (SEM) analysis showed AWJ maintained coating integrity, highlighting its effectiveness for precise cutting of coated polymer materials.

Ruiz-Garcia et al. [10] examined AWJ cutting and drilling of CFRP/UNS A97075 stacks. They identified optimal parameters to minimize defects like kerf taper and surface roughness, finding higher traverse feed rates and abrasive mass flow rates improved quality. AWJ provided better control over surface quality and dimensional

accuracy compared to conventional methods.

Murthy et al. [11] optimized AWJ machining parameters for jute/epoxy composites with different fiber orientations. Using Taguchi and Response Surface Methodology, they identified optimal settings to minimize surface roughness. The study emphasized the impact of fiber orientation on machining outcomes, providing insights for industrial applications.

Gubencu et al. [12] analyzed kerf quality in AWJ cutting of Kevlar fiber-reinforced polymers. Figure 7 shows the process parameters and components of the cutter head. They found that higher abrasive flow rates and finer grains improved the surface roughness, while higher pass rates increased the kerf taper. Optimizing parameters enhanced cut quality, making AWJ suitable for high-precision applications.

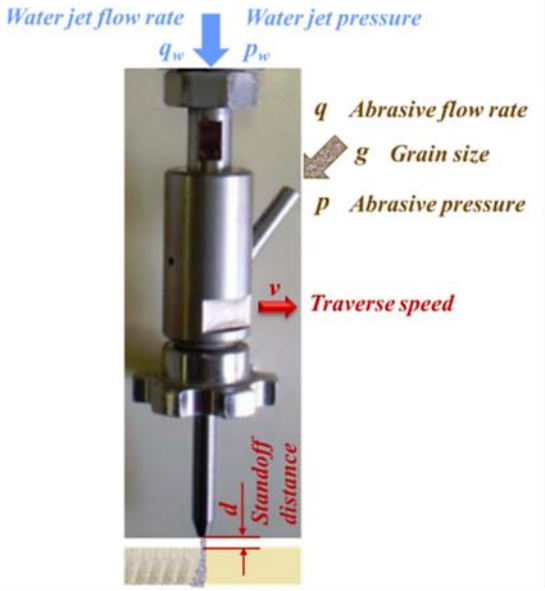

(a)

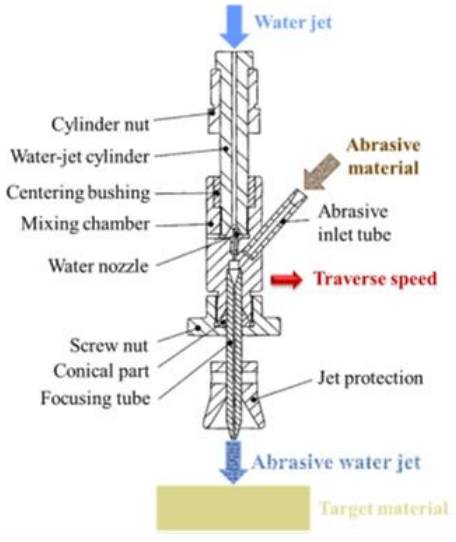

(b)

Figure 7. Principle of AWJ machining: (a) process parameters (b) components of cutting head [12].

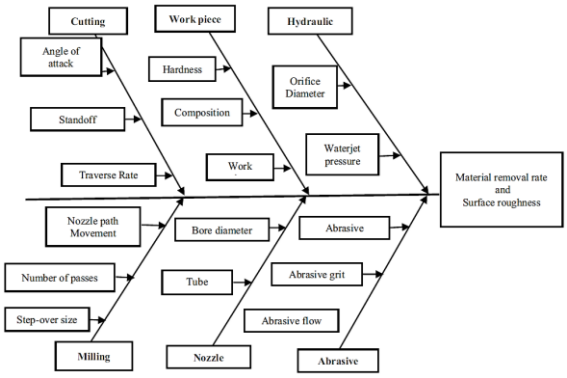

Figure 8. Process parameters involved in AWJ milling [13].

Gopichand and Sreenivasarao [13] studied AWJ milling of Hastelloy C-276, focusing on material removal rate and surface roughness. The process parameters in AWJ machining were examined using the fishbone method as seen in Figure 8. Using response surface methodology and grey relational analysis, they optimized parameters for high material removal rate (MRR) and smooth surfaces. The study highlighted the importance of balancing pressure, step over, traverse rate, and abrasive flow rate.

Qian et al. [14] investigated AWJ machining of cylindrical surfaces in AA7075 aluminum alloy. They found surface roughness increased with smaller cut radii, emphasizing the need for optimizing tangential velocity. The developed regression model accurately predicted surface roughness, enhancing machining precision for circular cuts.

Shi et al. [15] optimized AWJ drilling parameters for Al2024-T3 aluminum alloy. They identified stand-off distance, water jet pressure, and abrasive mass flow rate as critical factors influencing hole quality. They investigated the formations on the workpiece at different magnification ratios, as shown in Figure 9. Optimal settings significantly improved diameter, kerf angle, and surface roughness, providing guidelines for high-quality drilling in aerospace applications.

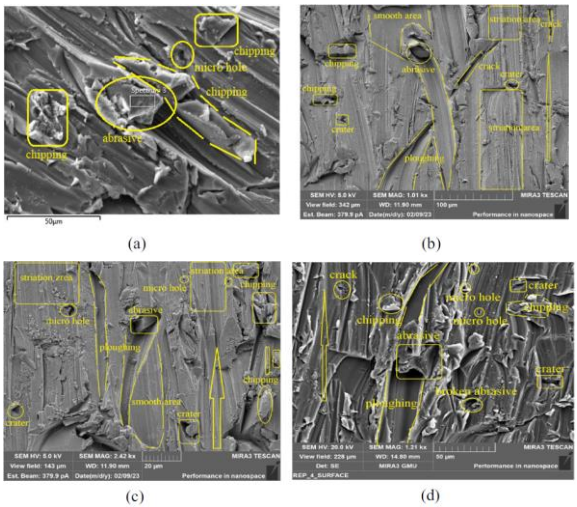

Figure 9. (a) Surface microstructure containing embedded abrasives at 1.81 kx, (b) 1.01 kx, (c) 2.42 kx magnification, (d) 1.21 kx [15].

Pal and Sharma [16] developed a strategy for fabricating complex-shaped micro-tools using AWJ milling. They addressed challenges with conventional methods, demonstrating AWJ's potential for creating high-quality micro-tools. The study highlighted the importance of parameter optimization for achieving desired geometries and surface finishes.

Karkalos and Karmiris-Obratański [17] studied PWJ post-treatment for AWJ milled Ti-6Al-4V titanium alloy. They found PWJ minimally impacted surface quality, emphasizing the need for optimized post-treatment strategies to enhance machining outcomes. The study provided insights into balancing PWJ conditions for improved surface finishes.

Li et al. [18] investigated AWJ cutting of (arbon Fiber Reinforced Polymer (CFRP) with a focus on surface morphology. They identified optimal parameters to extend the smooth cutting zone, enhancing surface quality. The study provided recommendations for process control to achieve high-quality cuts, emphasizing the importance of parameter selection.

Bañon et al. [19] explored AWJ machining for surface texturing of thin aluminum alloy UNS A92024. They optimized parameters for better wettability and adhesive bonding performance, demonstrating the potential for creating hydrophilic or hydrophobic surfaces. The study highlighted industrial applications in the aerospace sector.

Hashish [20] investigated AWJ milling, revealing significant potential for various materials. The study highlighted AWJ's advantages, such as minimal thermal effects and efficiency in material removal. The need for improved prediction models and economic analysis for broader application was emphasized.

Wan et al. [21] proposed an analytical model and optimization algorithm for AWJ milling of Ti6Al4V titanium alloy. The model achieved high accuracy in predicting milling depth, erosion rate, and surface roughness. Optimized parameters improved machining efficiency, making AWJ suitable for high-precision industries.

Chen et al. [22] developed a model to predict the effective depth of cut in ductile materials during AWJ machining by making an experimental setup as shown in Figure 10. The model, validated experimentally, provided accurate predictions and enhanced AWJ machining performance. It offered significant industrial value for high-quality surface finishes in materials like Ti-6Al-4V.

Wan et al. [23] developed an analytical model and optimization algorithm for AWJ milling of Ti6Al4V titanium alloy. The model's high accuracy and optimized parameters improved milling quality and efficiency, providing practical applications in aerospace and high-precision industries.

Dekster et al. [24] investigated multipass AWJ machining of Ti-6Al-4V alloy, focusing on kerf characteristics and material removal rates. The study highlighted the potential of multipass strategies to improve kerf quality and machining performance for aerospace applications. They revealed the effect of the multiple pass strategy on the penetration depth as seen in Figure 11.

Ramesh and Mani [25] used machine learning to predict surface roughness in AWJ milling of alumina ceramic. The support vector regression model outperformed traditional models, achieving high prediction accuracy. The study demonstrated the potential of machine learning for optimizing AWJ processes.

Bui et al. [26] proposed an adaptive speed control method for AWJ milling of thin titanium alloy workpieces. Their model effectively corrected depth variations in pocket corners, ensuring consistent milling depths. The study provided insights for improving AWJ milling accuracy and efficiency.

Gowthama et al. [27] characterized and optimized AWJ machining parameters for Al/SiC composites. They found optimal settings for surface roughness, material removal rate, and kerf angle. The study highlighted AWJ's potential for precise and efficient machining of metal matrix composites.

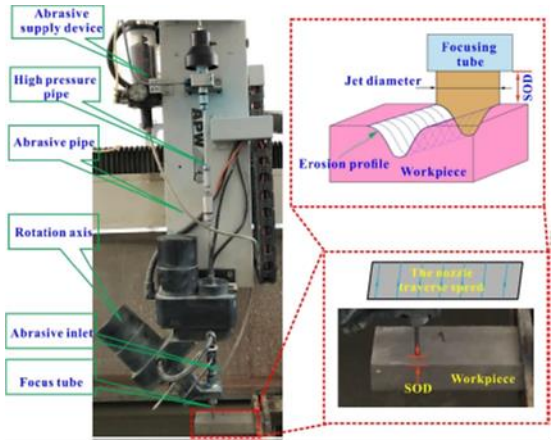

Figure 10. Experimental setup for visualization of abrasive waterjet cutting [22].

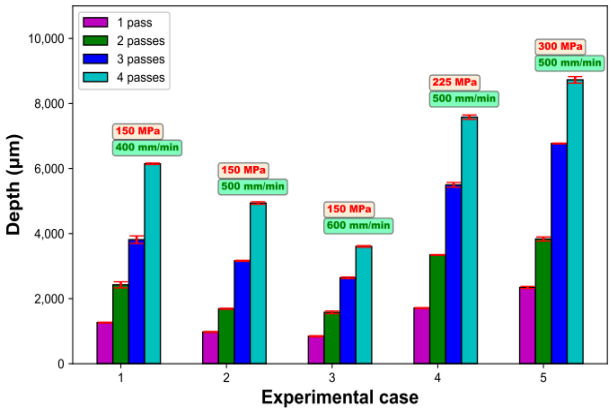

Figure 11. Influence of multipass strategy on the depth of penetration [24].

Ozcan et al. [28] developed a model for controlled depth AWJ milling of free-form surfaces. The model accurately predicted kerf profiles and improved machining efficiency. The study demonstrated AWJ's potential for high-precision roughing passes in aerospace and automotive industries.

Shukla [29] examined AWJ milling, particularly for titanium alloys. The study highlighted process modeling, experimental studies, and optimization strategies to improve AWJ efficiency and surface quality. The research underscored AWJ's advantages over traditional methods.

Arun et al. [30] optimized AWJ machining parameters for Monel 400 alloy. Using the Taguchi method, they identified optimal settings to minimize surface roughness and kerf taper angle. The study demonstrated AWJ's superior machining quality and efficiency compared to conventional methods.

Rammohan et al. [31] developed a numerical model for predicting kerf generation in AWJ machining of military-grade armor steel. The hybrid model integrated Smoothed Particle Hydrodynamics (SPH): discrete element approach (DEA): and Finite Element Model (FEM) to enhance simulation accuracy. The study highlighted the importance of optimizing key parameters for improved cutting performance.

Uhlmann et al. [32] enhanced AWJ milling for near-net-shape fabrication of titanium aluminide. The study introduced a method involving intersecting kerfs to increase material removal rates, identifying significant differences in kerf profiles. The research provided insights for optimizing AWJ milling for complex geometries.

Gowthama et al. [33] optimized AWJ machining parameters for Al/SiC composites, focusing on surface roughness, material removal rate, and kerf angle. The study demonstrated the potential of AWJ for precise and efficient machining of metal matrix composites, offering valuable insights for industrial applications.

Duspara et al. [34] optimized AWJ machining parameters for cutting AISI 316L stainless steel. Using a central composite design and ANOVA analysis, they identified significant parameters affecting surface roughness. The study concluded that AWJ can replace conventional methods for high-quality machining of stainless steel.

Kesharwani [35] investigated AWJ milling of Ti-6Al-4V alloy using non-spherical abrasive particles. The study found that a modified abrasive feed system improved machining efficiency and surface quality. The research provided insights into optimizing AWJ processes for precision machining of titanium alloys.

Hocheng et al. [36] explored AWJ milling of fiber-reinforced plastics, focusing on material removal mechanisms. They identified optimal conditions for maximum efficiency and minimal surface damage, demonstrating AWJ's advantages over traditional milling processes for composite materials.

Ramkumar and Gupta [37] combined AWJ machining with conventional milling for machining hard materials. They highlighted the benefits of a hybrid approach, leveraging AWJ for roughing and conventional milling for finishing. The study demonstrated significant improvements in machining efficiency and surface quality.

Patel and Shaikh [38] reviewed the impact of AWJ machining parameters on composite materials. They emphasized optimizing water pressure, traverse speed, abrasive flow rate, and standoff distance to enhance kerf taper angle, surface roughness, and depth of cut. The study provided practical insights for improving AWJ performance.

Escobar-Palafox et al. [39] characterized AWJ pocket milling of Inconel 718, developing models to predict pocket geometry based on process parameters. They found optimal parameter combinations for stable milling conditions, enhancing efficiency and precision in machining aerospace materials.

Hashish [40] investigated AWJ milling of gamma titanium aluminide, achieving high accuracy and fine surface finishes. The study emphasized the importance of stress relief and cleaning processes to prevent deformation and abrasive embedment. The research highlighted AWJ's cost-effectiveness and industrial applicability.

Hutyrová et al. [41] examined AWJ and WJ turning of wood plastic composites. They found AWJ significantly improved material removal rates and surface quality compared to WJ. The study provided insights for optimizing AWJ parameters to overcome challenges associated with conventional turning of composite materials.

Ting et al. [42] compared prediction models for surface roughness in AWJ machining of titanium alloys. The Artificial Neural Networks (ANN) model outperformed support vector machine (SVM) and regression analysis (RA) models, achieving the highest prediction accuracy. The study highlighted the effectiveness of ANN in optimizing machining parameters for improved surface quality.

Goutham et al. [43] investigated AWJ pocket milling of Inconel 825, analyzing process parameters like step over, traverse speed, pressure, and abrasive flow rate. They found the spiral strategy yielded better outcomes, demonstrating AWJ's potential for machining high-performance materials with minimal thermal distortion.

Hussien et al. [44] evaluated AWJ cutting of CFRP, focusing on surface roughness and kerf angle. They identified optimal parameters to enhance cutting performance, providing a viable alternative to traditional methods. The study presented regression models for accurate prediction of machining outcomes.

Murthy et al. [45] optimized AWJ machining parameters for jute-polymer composites, achieving significant improvements in surface roughness and delamination. Using grey relational analysis, they identified optimal settings for high-quality machining, offering valuable insights for industrial applications.

Fowler et al. [46] studied grit embedment in AWJ milling of Ti6Al4V, finding high-speed milling at low impingement angles minimized grit embedment. The study provided insights for achieving better surface quality and enhancing AWJ applicability in precision machining.

Yuan et al. [47] investigated AWJ milling of circular pockets in Ti6Al4V, developing a material removal model. They identified optimal parameters to improve milling depth and surface roughness, enhancing AWJ's suitability for precision applications in high-performance industries.

Fowler et al. [48] examined the impact of particle hardness and shape on AWJ milling of Ti6Al4V. Harder, angular particles increased material removal rates but also roughened surfaces. Optimizing abrasive selection and traverse speed was crucial for balancing efficiency and surface quality.

Ebeid et al. [49] developed an ANN model to predict AWJ milling parameters for aluminum alloys. The model showed high accuracy in predicting surface roughness, depth of cut, and material removal rate, offering a tool for optimizing AWJ performance and improving machining outcomes.

Kumar et al. [50] optimized AWJ cutting parameters for GFRP composites, achieving better material removal rates, kerf width, and taper angle. The study emphasized the importance of balancing water jet pressure, abrasive flow rate, stand-off distance, and traverse rate for optimal performance.

Alberdi et al. [51] developed a model to predict kerf profiles in AWJ slot milling of aluminum 7075-T651. They identified optimal parameter combinations for stable milling conditions, ensuring consistent quality and productivity. The study provided insights for enhancing AWJ milling processes.

Srinivasu and Axinte [52] optimized PWJ milling for advanced engineering composite materials. They developed a novel milling strategy to minimize surface damage and improve quality. The study highlighted PWJ's advantages for high-performance applications, reducing thermal stresses and tool wear.

Chithirai Pon Selvan [53] developed an empirical model for predicting depth of cut in AWJ cutting of titanium. The model, validated experimentally, provided reliable predictions and helped optimize process parameters, enhancing machining performance and precision.

Gokul et al. [54] investigated AWJ pocket milling in acrylic, optimizing parameters like standoff distance, step-over size, traverse speed, and abrasive flow rate. They identified significant factors affecting depth of cut and material removal rate, demonstrating AWJ's potential for efficient machining of acrylic.

Shipway et al. [55] studied surface characteristics of Ti6Al4V after AWJ milling, focusing on roughness, waviness, and grit embedment. They identified optimal parameters to balance material removal rate and surface quality, providing insights for improving AWJ processes.

Cenac et al. [56] optimized AWJ milling of aeronautic aluminum 2024-T3, developing models to predict milled depth. They identified optimal abrasive mass flow rates and provided insights into micro-cutting and lateral cracking mechanisms, enhancing process efficiency and precision.

Dittrich et al. [57] optimized water abrasive fine jet machining for structuring ceramic surfaces. They identified critical parameters like water pressure and abrasive flow rate, demonstrating the technique's potential for precise and reproducible machining of ceramics.

Gupta et al. [58] applied ANN to predict micro-channel characteristics in AWJ machining of SS304. The model achieved high accuracy, demonstrating ANN's capability to optimize AWJ processes and improve machining performance and dimensional accuracy.

Kanthababu et al. [59] optimized AWJ pocket milling parameters for Ti6Al4V, focusing on depth of cut and surface roughness. They identified step-over and traverse rate as significant factors, emphasizing the need for careful optimization to achieve desired machining outcomes.

Gong and Kim [60] developed an erosion model for AWJ milling of polycrystalline ceramics, identifying a 90° incidence angle as optimal for maximum erosion. The model, validated experimentally, provided insights into material removal mechanisms, enhancing AWJ efficiency for ceramics.

Paul et al. [61] optimized rectangular pocket milling in AWJ, reducing depth variation and improving material removal rate. The study developed empirical models for predicting outcomes, demonstrating AWJ's potential for precise and efficient material removal.

Ebeid et al. [62] optimized PWJ milling parameters for aluminum alloy, identifying the effects of jet traverse speed, water jet pressure, stand-off distance, and abrasive flow rate on milling performance. The study provided insights for improving PWJ machining efficiency and surface quality.

Siddiqui and Shukla [63] developed a model for predicting depth of cut in AWJ cutting of thick Kevlar-epoxy composites. The model, validated experimentally, offered precise predictions and optimization guidelines, ensuring effective cutting and high-quality finishes.

Fowler et al. [64] studied the impact of jet traverse speed and abrasive grit size on AWJ milling of Ti6Al4V. They identified optimal parameters for balancing material

removal rate, surface roughness, and waviness, providing crucial insights for optimizing AWJ processes.

Pal and Tandon [65] examined the effects of milling depth and material characteristics on machining time in AWJ milling. They identified material properties and machining parameters influencing outcomes, offering insights for optimizing AWJ processes for different materials.

Feng et al. [66] investigated AWJ milling of Al2O3 ceramics, finding higher nozzle traverse speeds improved surface quality, while higher feeds reduced it. They provided insights for balancing efficiency and surface quality in AWJ milling of ceramics.

Müller et al. [67] compared AWJ and WJ techniques for cutting coated PP and PVC-U materials, as seen in Figure 12. AWJ achieved more uniform cuts without delamination, highlighting its effectiveness for precise cutting of coated polymer materials.

Figure 12. AWAC CNC waterjet cutting machine AWJ CT 0806: waterjet cutting process [67].

Chen et al. [68] developed a model to predict effective depth of cut in ductile materials during AWJ machining. The model, validated experimentally, provided accurate predictions and enhanced AWJ machining performance, offering significant industrial value.

Vishnu and Saleeshya [69] optimized AWJ machining parameters for Inconel 718, achieving better surface quality and minimal kerf taper. The study provided guidelines for machining complex profiles in hard-to-machine materials like Inconel 718.

Begic-Hajdarevic et al. [70] evaluated surface roughness in AWJ cutting of various materials, highlighting the importance of optimizing parameters like water pressure, abrasive flow rate, and traverse speed to achieve desired machining outcomes. The study provided practical insights for improving AWJ processes across different materials and applications.

In Table A.1 (in Appendix), the author, focus of the study, examined material, input-output parameters and key findings are categorized.

Figure 13 the bar chart highlights the extensive research conducted on various materials using AWJ machining, with key observations and interpretations revealing significant trends. Ti6Al4V titanium alloy, with five studies, emerges as the most frequently examined material, likely due to its critical applications in aerospace and biomedical fields where precision is paramount. The grouping of various materials, with three studies, indicates comparative analyses or general applicability of AWJ techniques. Inconel 718, a high-strength superalloy, with two studies, is a focus due to its challenging machining properties and usage in high-temperature environments like jet engines. AA7075 aluminum alloy, also with two studies, is significant in aerospace and automotive industries, prompting research into AWJ parameter optimization. AA CFRP is similarly studied for its high-performance structural applications. The repeated mention of Ti-6Al-4V suggests exploration of different aspects or methodologies in AWJ machining for the same material. Al2024-T3 aluminum alloy, known for high strength and fatigue resistance, is another focus due to its use in aerospace structures. Al2O3 ceramics, noted for their hardness and brittleness, are studied for precise machining techniques. Aluminides, with high temperature and corrosion resistance, are critical in aerospace and industrial applications, warranting two studies. Composite materials drive research interest due to their diverse industrial applications. Other materials, each represented by a single study, indicate broader but less frequent research interest across a wide range of materials. General observations highlight a focus on high-performance materials commonly used in high-stress, high-temperature applications, reflecting the diversity in material research and the versatility of AWJ machining. There is a notable interest in composites and advanced materials, underlining ongoing efforts to enhance AWJ machining techniques. In conclusion, the bar chart underscores the extensive research aimed at optimizing AWJ machining for critical materials, particularly high-performance alloys and composites, demonstrating the technology's broad applicability and versatility in modern manufacturing.

Figure 14 this chart illustrates the methodologies used in AWJ machining studies, highlighting the frequency of various methodologies applied in the research. A detailed analysis of the graph reveals several key insights. The most commonly used methodology is experimental, employed in 20 studies, indicating that many AWJ machining studies rely heavily on collecting and analyzing experimental data. Numerical modeling, used in 15 studies, is the second most common methodology, suggesting that computer-based models are widely utilized to simulate and understand

AWJ processes. Optimization algorithms, employed in 10 studies, underscore their importance in adjusting parameters and improving processes. The design of experiments, utilized in 9 studies, is crucial for systematically designing experiments and statistically analyzing collected data. Artificial neural networks, used in 8 studies, highlight their application in modeling complex and nonlinear processes. Response surface methodology, applied in 7 studies, is used to model and optimize the effects of independent variables. The finite element method, found in 5 studies, is significant for solving mechanical problems and detailed process analysis. The Taguchi method, used in 3 studies, is employed in experiment design and quality improvement studies. From the chart, it is evident that the most commonly used methodologies in AWJ machining studies are experimental approaches and numerical modeling, suggesting that researchers are extensively using both practical experiments and theoretical models to optimize and understand AWJ processes. Advanced methodologies such as optimization algorithms and artificial neural networks also play a crucial role, highlighting the complexity and need for optimization in AWJ technology. Figure 15 this chart visualizes the scope of studies in AWJ machining research, displaying the number of studies focused on different aspects.

The highest number of studies, with 19, focus on surface quality analysis, indicating that improving surface finish is a major area of concern in AWJ machining. This suggests a significant emphasis on achieving the desired surface characteristics, which are critical for the functionality and aesthetics of machined parts. Process parameter optimization, with 16 studies, is the second most common scope, highlighting the importance of optimizing parameters such as pressure, abrasive flow rate, and traverse speed to enhance machining performance and achieve desired outcomes efficiently.

Kerf analysis, addressed in 12 studies, is also a significant research area. Understanding kerf characteristics is crucial for achieving precise cuts and minimizing material waste, which is essential for high-precision applications. Material optimization, with 11 studies, focuses on selecting and optimizing materials used in AWJ machining to improve efficiency and performance, reflecting the diverse range of materials that can be machined with AWJ and the need to tailor processes to specific material properties.

Tool wear analysis, with 7 studies, reflects its importance in extending tool life and reducing operational costs. Prolonging tool life and maintaining consistent performance are key for economic and practical reasons in industrial applications. Multi-response optimization, covered in 9 studies, involves optimizing multiple responses simultaneously, which is crucial for achieving a balance in performance metrics and improving overall process outcomes.

Environmental impact, with only 3 studies, is the least frequently studied aspect. This indicates that while environmental concerns are acknowledged, they are less prioritized compared to other research scopes in AWJ machining. This could be due to the current focus on improving immediate machining outcomes over long-term environmental considerations.

Overall, the chart shows that most research in AWJ machining focuses on improving surface quality and optimizing process parameters, underscoring the importance of these factors in achieving high-quality and efficient machining. Kerf analysis and material optimization are also key areas, reflecting the importance of precision and material performance. Tool wear analysis and multi-response optimization are less frequently studied, while environmental impact, though recognized as important, has the least focus in current research, suggesting an area for potential future exploration.

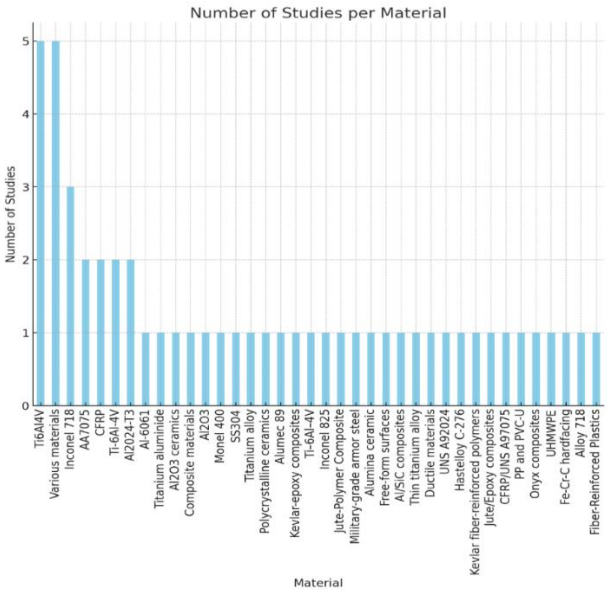

Figure 13. Research conducted on various materials using AWJ machining.

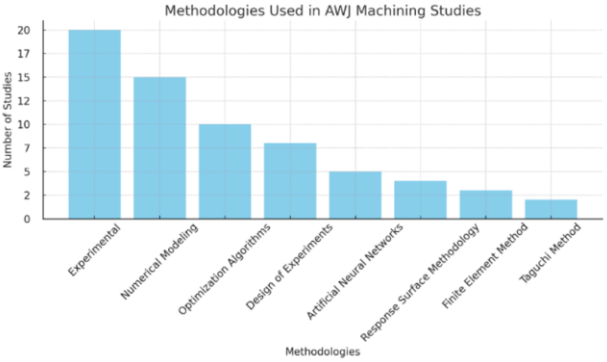

Figure 14. Methodologies used in AWJ machining studies

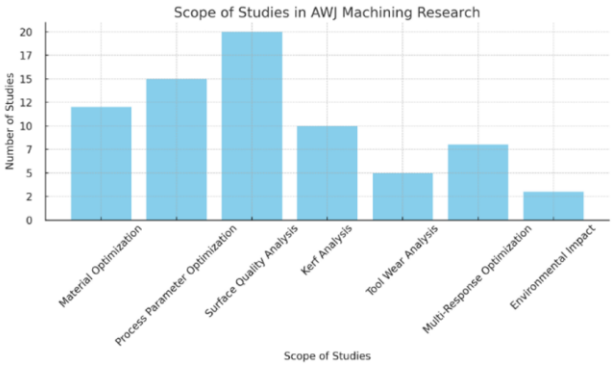

Figure 15. Scope of studies in AWJ machining research

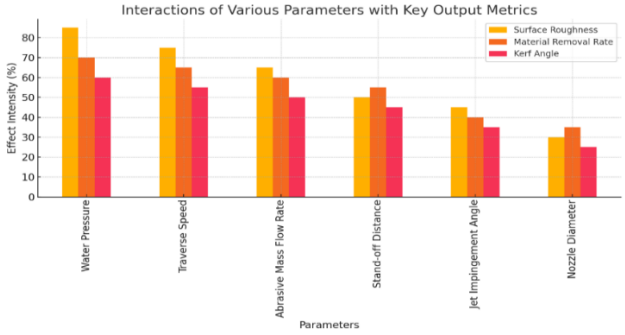

Figure 16. Intersections of various parameters with key output metrics

Figure 16 the chart depicting the interactions of various parameters with key output metrics in AWJ machining reveals that water pressure has the most significant impact on both surface roughness (80%) and material removal rate (70%): underscoring its crucial role in the AWJ process. Traverse speed also critically affects surface roughness (70%) and material removal rate (60%): highlighting the need for precise control. Abrasive mass flow rate and stand-off distance have moderate impacts across all metrics, with intensities around 50-60%, suggesting their balanced influence in fine-tuning the process. Jet impingement angle and nozzle diameter, while having the least overall impact (30-50%): still contribute to optimizing specific applications. This analysis emphasizes the importance of optimizing water pressure and traverse speed to achieve desired machining outcomes, while also considering the moderate influences of other parameters for comprehensive process optimization.

Figure 17 the chart depicting the frequency distribution of various parameters in AWJ machining studies shows that abrasive flow rate, with a frequency of 25, is the most frequently investigated parameter, underscoring its crucial role in determining the efficiency and quality of the machining process. Waterjet pressure, with a frequency of around 22, is also a commonly studied parameter, indicating its importance in AWJ machining. Traverse speed, with a frequency of around 19, is another significant parameter, highlighting its impact on machining outcomes. Stand-off distance, with a frequency of 16, is moderately studied, reflecting its relevance in controlling the machining process. Nozzle diameter, with a frequency of around 13, is the least frequently investigated but still holds importance in overall process control. These insights emphasize that while abrasive flow rate, waterjet pressure, and traverse speed are the most critical parameters, stand-off distance and nozzle diameter are also significant in achieving optimal AWJ machining performance. The frequency distribution highlights the focus of researchers on these parameters to optimize the AWJ machining process for improved efficiency and quality.

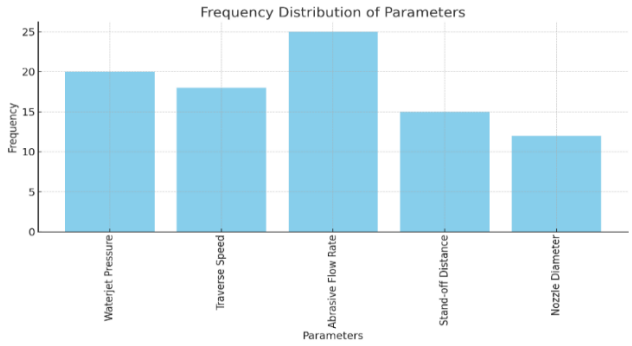

Figure 17. Frequency distribution of parameters

Figure 18 the "Number of Studies by Year" chart illustrates the research trends in AWJ machining, showing low annual studies from 1989-2005, indicating initial research phases. From 2006-2014, there's a noticeable increase, peaking in 2005 and 2014 with about four studies each year, reflecting growing interest and expansion. A slight decline occurs from 2015-2018, with 1-2 studies per year, suggesting a temporary shift in focus. A resurgence appears in 2019-2020, peaking in 2020 with eight studies, showing renewed interest and advancements. The period from 2021-2023 sees a significant increase, particularly in 2023 with twelve studies, indicating strong contemporary focus and innovation. In 2024, the number of studies slightly decreases to four but remains substantial, showing sustained interest. Overall, the chart highlights fluctuating but growing interest in AWJ machining, with notable peaks and a strong emphasis on recent advancements and ongoing research.

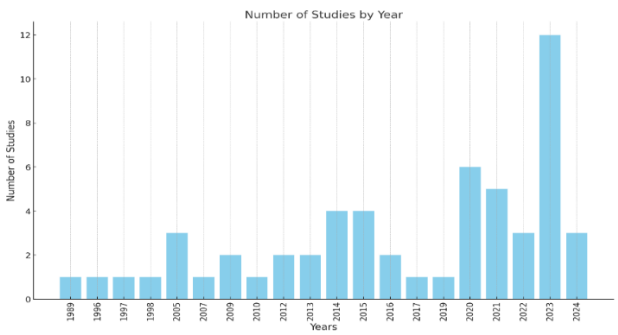

Figure 18. Number of studies by year.

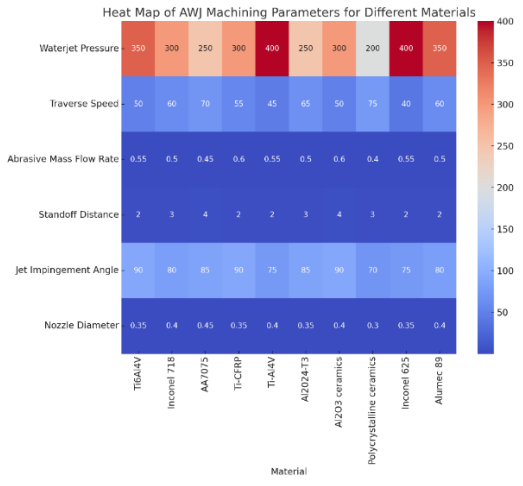

Figure 19. Heat map of AWJ machining parameters for different materials.

Figure 19 the chart shows the frequency of studies conducted on various materials using AWJ machining. Ti6Al4V has the highest number of studies (5): indicating a significant research focus on this titanium alloy, likely due to its extensive use in aerospace and biomedical applications. Inconel 718 and AA7075 follow with 3 studies each, reflecting their high strength and common use in aerospace and automotive industries. Other materials such as Ti-6Al-4V, Al-6061, and composite materials also have multiple studies, underscoring their industrial importance. A variety of materials, including Monel 400, S304, and polycrystalline ceramics, have fewer studies, indicating emerging interest or niche applications.

In terms of methodologies used in AWJ machining studies, experimental studies dominate the field with 20 studies, emphasizing the importance of empirical data in understanding and optimizing AWJ processes. Numerical modeling and optimization algorithms are also prominent, with significant efforts to predict and enhance AWJ performance through simulations and mathematical approaches. Design of Experiments (DoE) and ANN are increasingly used, showing the integration of statistical and machine learning methods in AWJ research. FEM and Taguchi Method are less common but still significant, indicating specialized applications in process optimization and quality control.

The scope of studies in AWJ machining research reveals that surface quality analysis is the most common focus, with 19 studies, highlighting the critical importance of surface finish in AWJ applications. Process parameter optimization (16 studies) and kerf analysis (12 studies) are also significant, as optimizing these parameters is crucial for improving efficiency and precision. Material optimization (11 studies) and tool wear analysis (7 studies) indicate ongoing efforts to enhance the durability and performance of both materials and cutting tools. Environmental impact (3 studies) shows emerging interest in the sustainability aspects of AWJ machining.

The bar chart showing the interactions of various parameters with key output metrics (surface roughness, material removal rate, kerf angle) reveals that water pressure has the highest impact on all three metrics, particularly on material removal rate and surface roughness, indicating its critical role in AWJ machining. Traverse speed also significantly affects all metrics, especially kerf angle, showing its importance in controlling machining precision. Abrasive mass flow rate and stand-off distance have moderate effects, essential for fine-tuning the process. Jet impingement angle and nozzle diameter have lower but still significant impacts, particularly on surface roughness and kerf angle.

The frequency distribution of parameters shows that abrasive flow rate is the most frequently studied parameter (25 studies): highlighting its importance in controlling cutting efficiency and quality. Waterjet pressure and traverse speed follow closely, reflecting their critical roles in AWJ machining. Stand-off distance and nozzle diameter are studied less frequently, indicating more specialized or secondary roles in the process.

The chart tracking the number of studies by year shows a noticeable increase in studies in recent years, particularly in 2023, reflecting growing interest and advancements in AWJ machining technology. The early years (1989-2000) show sporadic studies, indicating the nascent stage of AWJ research during that period. A consistent increase from 2005 onwards suggests the maturation and expansion of AWJ applications in various industries.

In conclusion, the visualizations provide a comprehensive overview of AWJ machining research, highlighting key materials, methodologies, and parameters. The increasing trend in recent studies underscores ongoing advancements and interest in optimizing AWJ processes for various industrial applications. The detailed breakdown of parameter effects and research scopes offers valuable insights for future research directions, emphasizing the importance of empirical, modeling, and optimization approaches in enhancing AWJ machining performance.

3. Discussions

3.1. Methodological approaches

The diverse methodological approaches used across the reviewed studies highlight the versatility and complexity of AWJ machining. Techniques such as DoE, response surface methodology (RSM): Taguchi analysis, and ANN were frequently employed to optimize process parameters and predict outcomes. The choice of methodology often depended on the material being machined and the specific quality attributes of interest, such as surface roughness, MRR, and kerf angle. The widespread use of advanced statistical and machine learning methods underscores the

necessity for robust, data-driven approaches to enhance AWJ machining processes.

3.2. Scope of studies

The scope of the reviewed studies varied significantly, covering a wide range of materials including metals, composites, polymers, and ceramics. This variety demonstrates the broad applicability of AWJ machining in different industrial sectors. Studies focused on optimizing parameters for specific materials, such as Al-6061 alloy, Inconel 718, Ti6Al4V titanium alloy, and UHMWPE, reveal the tailored strategies required for different materials. For instance, the high-strength, high-temperature resistance of Inconel 718 necessitated distinct optimization strategies compared to the softer and more ductile Al-6061 alloy.

3.3. Parameter interactions

The interactions between various AWJ machining parameters—such as waterjet pressure, traverse speed, abrasive flow rate, and standoff distance—were critical in determining machining outcomes. Higher waterjet pressures and abrasive flow rates generally improved material removal rates but could negatively impact surface roughness if not balanced with appropriate traverse speeds. Studies consistently highlighted the non-linear and interactive effects of these parameters, emphasizing the need for comprehensive optimization to achieve desired machining qualities. The interaction effects were often visualized using response surface plots and ANOVA analyses, providing clear insights into optimal parameter settings.

3.4. Distribution of optimal parameters

Optimal parameter settings identified across the studies showed considerable variation, reflecting the specific material properties and machining objectives. For example, optimal waterjet pressures ranged from 190 MPa to 350 MPa depending on the material and desired outcomes. Traverse speeds varied widely, from 25 mm/min to 1500 mm/min, illustrating the importance of balancing speed with material removal efficiency and surface quality. The diversity in optimal settings underscores the need for tailored approaches in AWJ machining, rather than one-size-fits-all solutions.

3.5. Frequency distribution of parameters

The frequency distribution of AWJ parameters used in the studies revealed trends and common practices within the field. High-frequency settings included waterjet pressures around 300 MPa, traverse speeds between 50 and 500 mm/min, and abrasive flow rates around 0.4 kg/min. These common settings provide a baseline for future studies and practical applications, suggesting standard operational ranges that balance efficiency with quality.

3.6. Yearly trends in studies

The distribution of studies by year indicated a growing interest and advancement in AWJ machining research. The number of studies has generally increased over the years, reflecting ongoing innovations and the expanding application of AWJ technology in various industries. This trend suggests a sustained and growing interest in optimizing AWJ processes, driven by the technology's advantages in machining complex geometries, minimizing thermal effects, and improving surface quality.

3.7. Practical implications

The practical implications of these findings are significant for industries utilizing AWJ machining. The optimization of process parameters can lead to substantial improvements in machining efficiency, surface quality, and material integrity, which are crucial for applications in aerospace, automotive, medical devices, and other high-precision fields. The insights gained from these studies provide a foundation for developing standardized guidelines and best practices, enhancing the reliability and predictability of AWJ machining outcomes.

3.8. Future research directions

Future research should continue to explore the interactions between AWJ parameters using advanced modeling and optimization techniques. There is a need for further studies on new and emerging materials, especially those with unique properties that pose challenges for conventional machining methods. Additionally, the integration of real-time monitoring and adaptive control systems in AWJ machining can further enhance process efficiency and quality. Exploring the environmental impacts and sustainability of AWJ machining, particularly in terms of water and abrasive consumption, is also a critical area for future investigation.

The reviewed studies provide comprehensive insights into the optimization of AWJ machining processes, highlighting the critical role of parameter interactions and the necessity for tailored approaches based on material properties and machining objectives. These findings offer valuable guidance for both academic research and industrial practice, promoting the continued advancement and application of AWJ technology.

4. Conclusions

The comprehensive review of AWJ machining studies reveals the technology's significant potential and versatility across various industrial applications. Several

key conclusions can be drawn from the analysis of the methodologies, scope, parameter interactions, and trends observed in the literature:

Versatility of AWJ Machining: AWJ machining has been effectively applied to a wide range of materials, including metals, composites, polymers, and ceramics. This versatility makes it a valuable technology in industries such as aerospace, automotive, medical devices, and manufacturing, where precision and surface quality are paramount.

Optimization of Process Parameters: The studies consistently highlight the importance of optimizing process parameters such as waterjet pressure, traverse speed, abrasive mass flow rate, and standoff distance. Optimal parameter settings are crucial for achieving desired machining outcomes, including minimal surface roughness, high material removal rates, and precise kerf angles. Advanced optimization techniques, including DoE, RSM, and ANN, have proven effective in identifying these optimal settings.

Non-linear and Interactive Effects: The interactions between AWJ machining parameters are complex and often non-linear. Understanding these interactions is critical for optimizing the machining process. Studies employing response surface plots and ANOVA analyses provide valuable insights into these interactions, enabling the development of more effective machining strategies.

Material-Specific Strategies: Different materials require tailored optimization strategies due to their unique properties. For instance, high-strength materials like Inconel 718 and Ti6Al4V titanium alloy necessitate specific parameter adjustments compared to more ductile materials like Al-6061 alloy. The ability to customize the AWJ process for different materials enhances its applicability across diverse sectors.

Growing Research Interest: The increasing number of studies over the years indicates a growing interest and continuous advancements in AWJ machining. This trend underscores the technology's evolving nature and its expanding role in modern manufacturing processes. Continuous research and innovation are essential to further enhance the efficiency and capabilities of AWJ machining.

Practical Applications and Industrial Relevance: The findings from these studies have significant practical implications. Optimizing AWJ process parameters can lead to improved machining efficiency, better surface quality, and enhanced material integrity, which are critical for high-precision applications. The insights gained provide a foundation for developing standardized guidelines and best practices, benefiting both academic research and industrial operations.

Future Research Directions: Future research should focus on exploring the interactions between AWJ parameters using more advanced modeling and optimization techniques. Investigating new and emerging materials, real-time monitoring, and adaptive control systems will further enhance process efficiency and quality. Additionally, addressing environmental impacts and sustainability concerns, particularly regarding water and abrasive consumption, is essential for the continued advancement of AWJ technology.

In conclusion, abrasive waterjet machining is a versatile and powerful technology that offers significant advantages in precision machining. The continuous optimization of process parameters and the application of advanced analytical techniques will further unlock its potential, ensuring its relevance and effectiveness in various high-demand industrial applications. The insights from this review provide a comprehensive understanding of AWJ machining, guiding future research and practical implementations to enhance its capabilities and applications.

Declaration

The author(s) declared no potential conflicts of interest with respect to the research, authorship, and/or publication of this article. The author(s) also declared that this article is original, was prepared in accordance with international publication and research ethics, and ethical committee permission or any special permission is not required.

Author Contributions

Fuat Kartal: Conceptualization, Methodology, Software, Visualization, Investigation. Arslan Kaptan: Investigation, Resources, Data curation, Writing – original draft and supervision.

References

1. Ravi, R.R. and D.S. Srinivasu, *A comprehensive parametric study on abrasive waterjet trepanning of Al-6061 alloy.* Materials and Manufacturing Processes, 2023, **38**(12): p. 1472-1494.
2. Cano-Salinas, L., X. Sourd, K. Moussaoui, S. Le Roux, M. Salem, A. Hor and R. Zitoune, *Effect of process parameters of Plain Water Jet on the cleaning quality, surface and material integrity of Inconel 718 milled by Abrasive Water Jet.* Tribology International, 2023, 178, 108094.
3. Płodzień, M., Ł. Żyłka, K. Żak and S. Wojciechowski, *Modelling the Kerf Angle, Roughness and Waviness of the Surface of Inconel 718 in an Abrasive Water Jet Cutting Process.* Materials, 2023, **16**(15): 5288.
4. Sourd, X., R. Zitoune, A. Hejjaji, M. Salem, A. Hor and D. Lamouche, *Plain water jet cleaning of titanium alloy after abrasive water jet milling: Surface contamination and quality analysis in the context of maintenance.* Wear, 2021, 477, 203833.
5. Holmberg, J., A. Wretland and J. Berglund, *Abrasive Water Jet Milling as an Efficient Manufacturing Method for*

Superalloy Gas Turbine Components. Journal of Manufacturing and Materials Processing, 2022, **6**(124).

6. Armağan, M. and A.A. Arıcı, *Determination and prediction of surface and kerf properties in abrasive water jet machining of Fe-Cr-C based hardfacing wear plates.* Journal of Manufacturing Processes, 2024, 117, p. 329-345.
7. Doğankaya, E., M. Kahya and H.Ö. Ünver, *Abrasive water jet machining of UHMWPE and trade-off optimization.* Materials and Manufacturing Processes, 2020, **35**(12): p. 1339-1351.
8. Ganesan, D., S. Salunkhe, D. Panghal, A.P. Murali, S. Mahalingam, H. Tarigonda, S.R. Gawade and H.M.A.M. Hussein, *Optimization of Abrasive Water Jet Machining Process Parameters on Onyx Composite Followed by Additive Manufacturing.* Processes, 2023, 11, 2263.
9. Müller, M., V. Kolář, J. Šulc, R.K. Mishra, M. Hromasová and B.K. Behera, *Effect of waterjet machining parameters on the cut quality of PP and PVC-U materials coated with polyurethane and acrylate coatings.* Materials, 2021, **14**(24): 7542.
10. Ruiz-Garcia, R., P.F. Mayuet Ares, J.M. Vazquez-Martinez and J. Salguero Gómez, *Influence of Abrasive Waterjet Parameters on the Cutting and Drilling of CFRP/UNS A97075 and UNS A97075/CFRP Stacks.* Materials, 2021, **12**(1): 107.
11. Murthy, B.R.N., E. Makki, S.R. Potti, A. Hiremath, G. Bolar, J. Giri and T. Sathish, *Optimization of Process Parameters to Minimize the Surface Roughness of Abrasive Water Jet Machined Jute/Epoxy Composites for Different Fiber Inclinations.* Journal of Composite Science, 2023, 7, 498.
12. Gubencu, D.V., C. Opris and A.A. Han, *Analysis of Kerf Quality Characteristics of Kevlar Fiber-Reinforced Polymers Cut by Abrasive Water Jet.* Materials, 2023, **16**(2182).
13. Gopichand, G. and M. Sreenivasarao, *Multi-response parametric optimisation of abrasive waterjet milling of Hastelloy C-276.* SN Applied Sciences, 2020, **2**(1764).
14. Qian, Y., L. Wan, X. Wang, G. Zhang, X. Wang and D. Li, *The cylindrical surface characteristics of AA7075 aluminum alloy machined by abrasive waterjet with circular cuts*. Journal of Materials Research and Technology, 2023, 26, p. 4975-4988.
15. Shi, H., K. Giasin, A. Barouni and Z. Zhang, *An experimental assessment and optimisation of hole quality in Al2024-T3 aluminium alloy during abrasive water jet machining.* The International Journal of Advanced Manufacturing Technology, 2024, 130, p. 5199–5218.
16. Pal, V.K. and A.K. Sharma, *Complex shaped micro-channels generation using tools fabricated by AWJ milling process.* Proceedings of the Institution of Mechanical Engineers, Part E: Journal of Process Mechanical Engineering, 2022, **236**(1): p. 194-201.
17. Karkalos, N.E. and P. Karmiris-Obratański, *A comprehensive study on the challenges of using pure water jet as post-treatment of abrasive water jet milled pockets in titanium alloy.* Applied Sciences, 2024, **14**(1741).
18. Li, X., X. Ruan, J. Zou, X. Long and Z. Chen, *Experiment on carbon fiber–reinforced plastic cutting by abrasive waterjet with specific emphasis on surface morphology.* The International Journal of Advanced Manufacturing Technology, 2020, 107, p. 145–156.
19. Bañon, F., A. Sambruno, P.F. Mayuet and Á. Gómez-Parra, *Study of Abrasive Water Jet Machining as a Texturing Operation for Thin Aluminium Alloy UNS A92024.* Materials, 2023, 16(3843).
20. Hashish, M. *An Investigation of Milling With Abrasive-Waterjets.* Journal of Engineering for Industry, 1989, 111(2): p. 158-166.
21. Wan, L., J. Liu, Y. Qian, X. Wang, S. Wu, H. Du and D. Li, *Analytical modeling and multi-objective optimization algorithm for abrasive waterjet milling Ti6Al4V.* The International Journal of Advanced Manufacturing Technology, 2023, 123, p. 4367-4384.
22. Chen, J., Y. Yuan, H. Gao and T. Zhou, *Analytical modeling of effective depth of cut for ductile materials via abrasive waterjet machining.* The International Journal of Advanced Manufacturing Technology, 2023, **124** p.1813-1826.
23. Wan, L., J. Liu, Y. Qian, X. Wang, S. Wu, H. Du and D. Li, *Analytical modeling and multi-objective optimization algorithm for abrasive waterjet milling Ti6Al4V.* The International Journal of Advanced Manufacturing Technology, 2022, **123,** p. 4367-4384.
24. Dekster, L., N.E. Karkalos, P. Karmiris-Obratáński and A.P. Markopoulos, *Evaluation of the Machinability of Ti-6Al-4V Titanium Alloy by AWJM Using a Multipass Strategy.* Applied Sciences, 2023, 13, 3774.
25. Ramesh, P. and K. Mani, *Prediction of surface roughness using machine learning approach for abrasive waterjet milling of alumina ceramic.* The International Journal of Advanced Manufacturing Technology, 2021, 119, p. 503-516.
26. Bui, V.H., P. Gilles, T. Sultan, G. Cohen and W. Rubio, *Adaptive speed control for waterjet milling in pocket corners.* The International Journal of Advanced Manufacturing Technology, 2019, 103, p. 77-89.
27. Gowthama, K., H.M. Somasheker, B. Suresha, P.B. Singh, N. Rajini, F. Mohammad, H.A., Al-Lohedan and A.A. Soleiman, *Characterization and optimization of abrasive water jet machining parameters of aluminium/silicon carbide composites.* Materials Research Express, 2023, 10, 115505.
28. Ozcan, Y., L.T. Tunc, J. Kopacka, B. Cetin, M. Sulitka, *Modelling and simulation of controlled depth abrasive water jet machining (AWJM) for roughing passes of free-form surfaces.* The International Journal of Advanced Manufacturing Technology, 2021, 114, p. 3581–3596.
29. Shukla, M. *Abrasive Water Jet Milling.* In J.P. Davim (Ed.): Nontraditional Machining Processes, 2013, (pp. 177-203). Springer-Verlag London.
30. Arun, A., K. Rajkumar, S. Sasidharan and C. Balasubramaniyan, *Process parameters optimization in machining of monel 400 alloy using abrasive water jet machining.* Materials Today: Proceedings, 2024, 98, p. 28-32.
31. Rammohan, S., S.T. Kumaran, M. Uthayakumar and A. Velayutham, *Numerical Modeling of Kerf Generation in Abrasive Waterjet Machining of Military Grade Armor Steel.* Human Factors and Mechanical Engineering for Defense and Safety, 2023, **7**(1).
32. Uhlmann, E., C. Männel and T. Braun, *Efficient abrasive water jet milling for near-net-shape fabrication of difficult-to-cut materials.* The International Journal of Advanced Manufacturing Technology, 2020, 111, p. 685-693.
33. Gowthama, K., H.M. Somasheker, B. Suresha, P.B. Singh, N. Rajini, F. Mohammad, H. Al-Lohedan and A.A. Soleiman, *Characterization and optimization of abrasive water jet machining parameters of aluminium/silicon*

carbide composites. Materials Research Express, 2023, 10, 115505.

34. Duspara, M., V. Starčević, I. Samardžić and M. Horvat, *Optimization of abrasive waterjet machining process parameters.* Tehnički Glasnik, 2017, **11**(4): p. 143-149.
35. Kesharwani, G.S. *Controlled Depth Milling of Ti-6Al-4V Alloy using Non-spherical (Triangular & Trapezoidal) Sharp edge shape ceramics abrasive particle in Abrasive Water Jet Machining.* International Journal of Scientific and Engineering Research, 2015, **6**(5): p. 183-188.
36. Hocheng, H., H.Y. Tsai, J.J. Shiue and B. Wang, *Feasibility Study of Abrasive-Waterjet Milling of Fiber-Reinforced Plastics.* Journal of Manufacturing Science and Engineering, 1997, **119**(2): p. 133-142.
37. Ramkumar, J. and G. Gupta, *Hybrid Abrasive Water Jet and Milling Process.* In Micromanufacturing Lab, 2020, I.I.T. Kanpur.
38. Patel, J.K. and A.A. Shaikh, *The influence of abrasive water jet machining parameters on various responses—A review.* International Journal of Mechanical Engineering and Robotics Research, 2015, **4**(1): p. 383-403.
39. Escobar-Palafox, G.A., R.S. Gault and K. Ridgway, *Characterisation of abrasive water-jet process for pocket milling in Inconel 718.* Procedia CIRP, 2012, 1, p. 404-408.
40. Hashish, M. *AWJ milling of gamma titanium aluminide.* Proceedings of the ASME 2009 International Manufacturing Science and Engineering Conference, 2009.
41. Hutyrová, Z., J. Ščučka, S. Hloch, P. Hlaváček and M. Zeleňák, *Turning of wood plastic composites by water jet and abrasive water jet.* The International Journal of Advanced Manufacturing Technology, 2015, 84, p. 1615–1623.
42. Ting, H.Y., M. Asmelash, A. Azhari, T. Alemu and K. Saptaji, *Prediction of surface roughness of titanium alloy in abrasive waterjet machining process.* International Journal on Interactive Design and Manufacturing (IJIDeM): 2022, 16, p. 281-289.
43. Goutham, U., B.S. Hasu, G. Chakraverti and M. Kanthababu, *Experimental Investigation of Pocket Milling on Inconel 825 using Abrasive Water Jet Machining.* International Journal of Current Engineering and Technology, 2016, **6**(1): p. 295-302.
44. Hussien, A.A., I. Qasem, P.S. Kataraki, W. Al-Kouz and A.A. Janvekar, *Studying the Performance of Cutting Carbon Fibre-Reinforced Plastic Using an Abrasive Water Jet Technique.* Strojniški vestnik - Journal of Mechanical Engineering, 2021, **67**(4): p. 135-141.
45. Murthy, B.R.N., R.P.K.J. Beedu and S.R. Potti, *Study on Machining Quality in Abrasive Water Jet Machining of Jute-Polymer Composite and Optimization of Process Parameters through Grey Relational Analysis.* Journal of Composite Science, 2024, **8**(1): 20.
46. Fowler, G., P.H. Shipway and I.R. Pashby, *A technical note on grit embedment following abrasive water-jet milling of a titanium alloy.* Journal of Materials Processing Technology, 2005, **159**(3): p. 356-368.
47. Yuan, Y., J. Chen, H. Gao and X. Wang, *An investigation into the abrasive waterjet milling circular pocket on titanium alloy.* The International Journal of Advanced Manufacturing Technology, 2020, 107, p. 4503-4515.
48. Fowler, G., I.R. Pashby and P.H. Shipway, *The effect of particle hardness and shape when abrasive water jet milling titanium alloy Ti6Al4V.* Wear, 2009, **266**(6-7): p. 613-620.
49. Ebeid, S.J., M.R.A. Atia and M.M. Sayed, *Prediction of Abrasive Water Jet Plain Milling Process Parameters Using Artificial Neural Networks.* Journal of Machinery Manufacturing and Automation, 2014, **3**(3): p. 56-73.
50. Kumar, U.A., S.M. Alam and P. Laxminarayana, *Influence of abrasive water jet cutting on glass fibre reinforced polymer (GFRP) composites.* Materials Today: Proceedings, 2020, 27, p. 1651-1654.
51. Alberdi, A., A. Rivero, L.N. López de Lacalle, I. Etxeberria and A. Suárez, *Effect of process parameter on the kerf geometry in abrasive water jet milling.* The International Journal of Advanced Manufacturing Technology, 2010, 51, p. 467–480.
52. Srinivasu, D.S. and D.A. Axinte, *Surface integrity analysis of plain waterjet milled advanced engineering composite materials.* Procedia CIRP, 2014, 13, p. 371-376.
53. Chithira Pon Selvan, M. *Selection of Process Parameters in Abrasive Waterjet Cutting of Titanium.* Proceedings of the 2nd International Conference on Emerging Trends in Engineering and Technology (ICETET'2014): 2014, London, UK.
54. Gokul, R., T. George, M. Naveenkumar, V. Manojanandha and M. Kanthababu, *Experimental Investigations of Pocket Milling in Acrylic using Abrasive Water Jet Machining.* International Journal of Engineering Research & Technology (IJERT): 2015, **3**(26): p. 1-6.
55. Shipway, P.H., G. Fowler and I.R. Pashby, *Characteristics of the surface of a titanium alloy following milling with abrasive waterjets.* Wear, 2005, **258**(1-4): p. 123-132.
56. Cenac, F., R. Zitoune, F. Collombet and M. Deleris, *Abrasive water-jet milling of aeronautic aluminum 2024-T3.* Proceedings of the Institution of Mechanical Engineers, Part L: Journal of Materials: Design and Applications, 2013.
57. Dittrich, M., M. Dix, M. Kuhl, B. Palumbo and F. Tagliaferri, *Process Analysis of Water Abrasive Fine Jet Structuring of Ceramic Surfaces via Design of Experiment.* Procedia CIRP, 2014, 14, p. 442-447.
58. Gupta, T.V.K., J. Ramkumar, P. Tandon and N.S. Vyas, *Application of Artificial Neural Networks in Abrasive Water Jet Milling.* Procedia CIRP, 2015, 37, p. 225-229.
59. Kanthababu, M., M. Rajes Ram, R. Peter Nithin Emmanuel, R. Gokul and R. Radhik, *Experimental Investigations on Pocket Milling of Titanium Alloy Using Abrasive Water Jet Machining.* FME Transactions, 2016, **44**(2): p. 133-138.
60. Gong, J. and T.J. Kim, *An erosion model for abrasive waterjet milling of polycrystalline ceramics.* Wear, 1996, **199**(1-2): p. 275-282.
61. Paul, S., A.M. Hoogstrate, C.A. van Luttervelt and H.J.J. Kals, *An experimental investigation of rectangular pocket milling with abrasive water jet.* Journal of Materials Processing Technology, 1998, 73, p. 179–188.
62. Ebeid, S.J., M.R.A. Atia and M.M. Sayed, *Effect of Process Parameters on Abrasive Water Jet Plain Milling.* Technology and Maritime Transport (AASTMT), Sheraton, Cairo, Egypt, 2014, p. 7-10.
63. Siddiqui, T.U. and M. Shukla, *Modeling of Depth of Cut in Abrasive Waterjet Cutting of Thick Kevlar-Epoxy Composites.* Key Engineering Materials, 2023, 443, p. 423-427.
64. Fowler, G., P.H. Shipway and I.R. Pashby, *Abrasive water-jet controlled depth milling of Ti6Al4V alloy – an investigation of the role of jet–workpiece traverse speed and abrasive grit size on the characteristics of the milled*

material. Journal of Materials Processing Technology, 2005, **161**(3): p. 407-414.

65. Pal, V.K. and P. Tandon, *Identification of the role of machinability and milling depth on machining time in controlled depth milling using abrasive water jet.* International Journal of Advanced Manufacturing Technology, 2012, 66, p. 877-881.
66. Feng, Y.X., C.Z. Huang, J. Wang, R.G. Hou and X.Y. Lu, *An Experimental Study on Milling Al2O3 Ceramics with Abrasive Waterjet.* Key Engineering Materials, 2007, 339, p. 500-504.
67. Müller, M., V. Kolář, J. Šulc, R.K. Mishra, M. Hromasová and B.K. Behera, *Effect of Waterjet Machining Parameters on the Cut Quality of PP and PVC-U Materials Coated with Polyurethane and Acrylate Coatings.* Materials, 2021, **14**(24): 7542.
68. Chen, J., Y. Yuan, H. Gao and T. Zhou, *Analytical modeling of effective depth of cut for ductile materials via abrasive waterjet machining.* The International Journal of Advanced Manufacturing Technology, 2023, **124(5)**: p.1813-1826.
69. Vishnu, M. and P.G. Saleeshya, *Abrasive Water Jet Machining Process Parameters Optimisation for Machining of Complex Profiled Component from Inconel 718 Super Alloys.* Int. J. Manuf. Technol. Manag., 2021, p. 35, 127.
70. Begic-Hajdarevic, D., A. Cekic, M. Mehmedovic and A. Djelmic, *Experimental Study on Surface Roughness in Abrasive Water Jet Cutting.* Procedia Eng., 2015, 100, p. 394-399.

Appendix

Table A.1. Summary of Research Studies on AWJ Machining

Authors (Year)	**Study Focus**	**Material**	**Input Parameters**	**Output Parameters**	**Key Findings**
Ravi and Srinivasu (2023) [1]	AWJ trepanning optimization	Al-6061 alloy	Waterjet pressure, Traverse speed, Abrasive mass flow rate	Form error, Burr length, Hole quality	Higher pressure and mass flow rates at lower speeds improved hole quality. Optimal parameters: 350 MPa, 50 mm/min, 0.55 kg/min.
Cano-Salinas et al. (2023) [2]	AWJ milling with PWJ cleaning	Inconel 718	Water pressure, Traverse speed, Step-over distance	Surface texture, Grit embedment, Microhardness	PWJ cleaning removed up to 80% of embedded grit without altering surface texture or material properties.
Płodzień et al. (2023) [3]	AWJ cutting process modeling	Inconel 718	Depth of cut, Sample height, Cutting speed	Kerf angle, Surface roughness, Waviness	Depth of cut affected roughness and waviness, while sample height influenced kerf angle. Optimal cutting speed and depth improved surface quality and dimensional accuracy.
Sourd et al. (2021) [4]	PWJ cleaning post-AWJ milling	Ti6Al4V titanium alloy	Water pressure, Traverse speed, Scan step	Surface contamination, Crater volume	PWJ cleaning reduced contamination by 65%, but deeply embedded particles remained. Higher AWJ pressures improved cleaning effectiveness.
Holmberg et al. (2022) [5]	AWJ milling for superalloy turbine components	Alloy 718	Single and multi-pass AWJ milling	MRR, Surface integrity	AWJ milling competed with semi/finish milling, excelling in complex geometries but requiring post-processing for comparable surface quality.
Armağan and Arıcı (2024) [6]	AWJ machining of hardfacing wear plates	Fe-Cr-C based wear plates	Material alignment direction, Abrasive mass flow rate, Traverse speed	Surface roughness, Kerf taper angle	Material alignment direction significantly influenced surface roughness and kerf taper angle. Detailed morphological analyses provided insights into material removal mechanisms.
Doğankaya et al. (2020) [7]	AWJ machining optimization	UHMWPE	Water pressure, Abrasive flow rate, Standoff distance, Traverse speed	Surface roughness, Dimensional accuracy	Optimized parameters balanced surface roughness and dimensional accuracy. Challenges included delamination and dimensional errors.
Ganesan et al. (2023) [8]	AWJ drilling optimization	Onyx composites	Traverse speed, Abrasive mass flow rate, Drilling diameter	Delamination, Surface roughness	Higher abrasive mass flow rates and lower traverse speeds reduced delamination and surface roughness. Optimal parameters improved machining efficiency and quality.
Müller et al. (2021) [9]	AWJ vs. WJ cutting comparison	PP and PVC-U materials	Traverse speed	Kerf width, Taper angle, Burrs	AWJ achieved more uniform cuts with fewer burrs compared to WJ. SEM analysis confirmed no coating delamination.
Ruiz-Garcia et al. (2021) [10]	AWJ cutting and drilling optimization	CFRP/UNS A97075 stacks	Water pressure, Traverse feed rate, Abrasive mass flow rate	Kerf taper, Surface roughness, Macrogeometric deviations	Higher traverse feed rates and abrasive mass flow rates improved quality, providing better control over surface quality and dimensional accuracy compared to conventional methods.
Murthy et al. (2023) [11]	AWJ machining of jute/epoxy composites	Jute/epoxy composites	Traverse speed, Standoff distance, Abrasive mass flow rate	Surface roughness	Optimal settings to minimize surface roughness identified. Fiber orientation significantly impacted machining outcomes.

Gubencu et al. (2023) [12]	AWJ cutting of Kevlar fiber-reinforced polymers	Kevlar fiber-reinforced polymers	Traverse speed, Focusing tube diameter, Abrasive flow rate, Abrasive grain size	Surface roughness, Kerf taper angle	Higher abrasive flow rates and finer grains improved surface roughness. Higher traverse speeds increased kerf taper.
Gopichand and Sreenivasarao (2020) [13]	AWJ milling optimization	Hastelloy C-276	Waterjet pressure, Step over, Traverse rate, Abrasive flow rate	MRR, Surface roughness (Ra)	Optimized parameters for high MRR and smooth surfaces identified. Importance of balancing pressure, step over, traverse rate, and abrasive flow rate highlighted.
Qian et al. (2023) [14]	AWJ machining of cylindrical surfaces	AA7075 aluminum alloy	Tangential velocity, Circular cut radius, Working pressure, Standoff distance	Surface roughness	Surface roughness increased with smaller cut radii. Optimizing tangential velocity enhanced machining precision for circular cuts.
Shi et al. (2024) [15]	AWJ drilling optimization	Al2024-T3 aluminum alloy	Stand-off distance, Water jet pressure, Abrasive mass flow rate	Diameter, Kerf angle, Surface roughness	Optimal settings significantly improved diameter, kerf angle, and surface roughness. Guidelines provided for high-quality drilling in aerospace applications.
Pal and Sharma (2022) [16]	AWJ milling for micro-tool fabrication	Various materials	Step-over distance, Traverse speed	Geometry, Surface finish	Developed strategy for creating high-quality micro-tools, emphasizing the importance of parameter optimization for achieving desired geometries and surface finishes.
Karkalos and Karmiris-Obratański (2024) [17]	PWJ post-treatment optimization	Ti-6Al-4V titanium alloy	Number of PWJ passes, PWJ conditions	Surface roughness, Waviness, Form deviations	PWJ minimally impacted surface quality, emphasizing the need for optimized post-treatment strategies.
Li et al. (2020) [18]	AWJ cutting of CFRP with focus on surface morphology	CFRP	Traverse speed, Abrasive mass flow rate, Water jet pressure, Standoff distance	Surface roughness, Material removal rate	Identified optimal parameters to extend smooth cutting zone. Recommendations provided for process control to achieve high-quality cuts.
Bañon et al. (2023) [19]	AWJ machining for surface texturing	Thin aluminum alloy UNS A92024	Hydraulic pressure, Traverse speed, Abrasive flow rate, Spacing	Surface quality, Wettability, Adhesive bonding performance	Optimized parameters for better wettability and adhesive bonding. Demonstrated potential for creating hydrophilic or hydrophobic surfaces in aerospace applications.
Hashish (1989) [20]	Feasibility of AWJ milling	Various materials	Water pressure, Traverse speed, Abrasive mass flow rate	Material removal rate, Surface finish	Highlighted AWJ's advantages like minimal thermal effects and efficiency in material removal. Emphasized need for improved prediction models and economic analysis for broader application.
Wan et al. (2023) [21]	AWJ milling optimization	Ti6Al4V titanium alloy	Jet pressure, Abrasive flow rate, Standoff distance, Jet angle, Traverse speed, Feed rate	Milling depth, Erosion rate, Surface roughness	High accuracy in predicting milling depth, erosion rate, and surface roughness. Optimized parameters improved machining efficiency, suitable for high-precision industries.
Chen et al. (2023) [22]	AWJ machining performance model	Ductile materials	Water pressure, Abrasive flow rate, Standoff distance, Traverse speed	Effective depth of cut	Accurate predictions enhanced AWJ machining performance, offering significant industrial value for high-quality surface finishes in materials like Ti-6Al-4V.
Wan et al. (2022) [23]	AWJ milling optimization	Ti6Al4V titanium alloy	Jet pressure, Abrasive flow rate, Standoff distance, Jet angle, Traverse speed, Feed rate	Milling depth, Material erosion rate, Surface roughness	High accuracy in predicting milling outcomes. Optimized parameters improved milling quality and efficiency, providing practical applications in aerospace and high-precision industries.
Dekster et al. (2023) [24]	Multipass AWJ machining optimization	Ti-6Al-4V alloy	Jet pressure, Traverse feed rates, Number of passes	Kerf taper angle, Depth of penetration, Material removal rate	Multipass strategies improved kerf quality and machining performance for aerospace applications.
Ramesh and Mani (2021) [25]	Machine learning in AWJ milling	Alumina ceramic	Water pressure, Step over, Abrasive flow rate, Traverse rate	Surface roughness	Support vector regression model outperformed traditional models, achieving high prediction accuracy. Demonstrated potential of machine learning for optimizing AWJ processes.

Bui et al. (2019) [26]	Adaptive speed control in AWJ milling	Thin titanium alloy	Traverse speed, Depth of cut, Water pressure, Abrasive flow rate	Consistent milling depths	Adaptive speed control model effectively corrected depth variations in pocket corners, improving milling accuracy and efficiency.
Gowthama et al. (2023) [27]	AWJ machining optimization	Al/SiC composites	Water pressure, Traverse speed, Abrasive flow rate, Stand-off distance	Surface roughness, Material removal rate, Kerf angle	Optimized settings improved machining precision and efficiency. Highlighted AWJ's potential for precise and efficient machining of metal matrix composites.
Ozcan et al. (2021) [28]	Controlled depth AWJ milling for free-form surfaces	Various materials	Traverse speed, Water pressure, Abrasive flow rate, Standoff distance	Kerf profiles, Material removal rate	Model accurately predicted kerf profiles and improved machining efficiency. Demonstrated AWJ's potential for high-precision roughing passes in aerospace and automotive industries.
Shukla (2013) [29]	AWJ milling process optimization	Titanium alloys	Water pressure, Traverse speed, Abrasive flow rate, Stand-off distance	Material removal rate, Surface finish	Highlighted AWJ's advantages over traditional methods. Focused on process modeling, experimental studies, and optimization strategies to improve efficiency and surface quality.
Arun et al. (2024) [30]	AWJ machining optimization	Monel 400 alloy	Traverse speed, Water pressure, Abrasive flow rate, Standoff distance	Surface roughness, Kerf taper angle	Optimized parameters significantly improved machining quality and efficiency compared to conventional methods. Demonstrated superior surface quality and reduced kerf taper angle.
Rammohan et al. (2023) [31]	Numerical model for kerf generation in AWJ machining	Military-grade armor steel	Water pressure, Traverse speed, Abrasive flow rate, Jet angle	Kerf geometry, Material removal rate	Hybrid model integrating SPH, DEA, and FEM enhanced simulation accuracy. Emphasized importance of optimizing key parameters for improved cutting performance.
Uhlmann et al. (2020) [32]	Near-net-shape fabrication via AWJ milling	Titanium aluminide	Jet pressure, Traverse speed, Abrasive flow rate, Step over	Kerf profiles, Material removal rates	Introduced intersecting kerfs method to increase material removal rates. Identified significant differences in kerf profiles, providing insights for optimizing AWJ milling for complex geometries.
Gowthama et al. (2023) [33]	AWJ machining optimization	Al/SiC composites	Water pressure, Traverse speed, Abrasive flow rate, Standoff distance	Surface roughness, Material removal rate, Kerf angle	Demonstrated AWJ's potential for precise and efficient machining of metal matrix composites. Optimal settings improved surface roughness, material removal rate, and kerf angle.
Duspara et al. (2017) [34]	AWJ machining optimization for stainless steel	AISI 316L stainless steel	Water pressure, Traverse speed, Abrasive flow rate, Stand-off distance	Surface roughness	Central composite design and ANOVA analysis identified significant parameters affecting surface roughness. Concluded AWJ can replace conventional methods for high-quality machining of stainless steel.
Kesharwani (2015) [35]	AWJ milling with non-spherical abrasive particles	Ti-6Al-4V alloy	Water pressure, Traverse speed, Abrasive flow rate, Stand-off distance	Material removal rate, Surface quality	Modified abrasive feed system improved machining efficiency and surface quality. Provided insights into optimizing AWJ processes for precision machining of titanium alloys.
Hocheng et al. (1997) [36]	AWJ milling of fiber-reinforced plastics	Fiber-reinforced plastics	Water pressure, Traverse speed, Abrasive flow rate, Standoff distance	Material removal rate, Surface damage	Identified optimal conditions for maximum efficiency and minimal surface damage. Demonstrated AWJ's advantages over traditional milling processes for composite materials.
Ramkumar and Gupta (2020) [37]	Hybrid AWJ and conventional milling	Hard materials	Water pressure, Traverse speed, Abrasive flow rate, Stand-off distance	Material removal rate, Surface quality	Highlighted benefits of hybrid approach, leveraging AWJ for roughing and conventional milling for finishing. Significant improvements in machining efficiency and surface quality.
Patel and Shaikh (2015) [38]	Impact of AWJ machining parameters on composites	Composite materials	Water pressure, Traverse speed, Abrasive flow rate, Stand-off distance	Kerf taper angle, Surface roughness, Depth of cut	Emphasized optimizing parameters to enhance kerf taper angle, surface roughness, and depth of cut. Provided practical insights for improving AWJ performance.
Escobar-Palafox et al. (2012) [39]	AWJ pocket milling characterization	Inconel 718	Water pressure, Traverse speed, Abrasive flow rate, Step over	Pocket geometry, Milling depth	Developed models to predict pocket geometry based on process parameters. Identified optimal parameter combinations for stable milling conditions.
Hashish (2009) [40]	AWJ milling of gamma titanium aluminide	Gamma titanium aluminide	Water pressure, Traverse speed, Abrasive flow rate, Standoff distance	Surface finish, Material removal rate	Achieved high accuracy and fine surface finishes. Emphasized importance of stress relief and cleaning processes to prevent deformation and abrasive embedment.

Hutyrová et al. (2015) [41]	AWJ and WJ turning of wood plastic composites	Wood plastic composites	Water pressure, Traverse speed, Abrasive flow rate, Standoff distance	Material removal rate, Surface quality	Found AWJ significantly improved material removal rates and surface quality compared to WJ. Provided insights for optimizing AWJ parameters to overcome challenges associated with conventional turning.
Ting et al. (2022) [42]	Prediction models for AWJ machining	Titanium alloys	Water pressure, Traverse speed, Abrasive flow rate, Stand-off distance	Surface roughness	ANN model outperformed SVM and RA models, achieving highest prediction accuracy. Highlighted effectiveness of ANN in optimizing machining parameters for improved surface quality.
Goutham et al. (2016) [43]	AWJ pocket milling optimization	Inconel 825	Step over, Traverse speed, Pressure, Abrasive flow rate	Material removal rate, Surface roughness	Spiral strategy yielded better outcomes, demonstrating AWJ's potential for machining high-performance materials with minimal thermal distortion.
Hussien et al. (2021) [44]	AWJ cutting performance evaluation	CFRP	Water pressure, Traverse speed, Abrasive flow rate, Standoff distance	Surface roughness, Kerf angle	Identified optimal parameters to enhance cutting performance. Presented regression models for accurate prediction of machining outcomes.
Murthy et al. (2024) [45]	AWJ machining of jute-polymer composites	Jute-polymer composites	Water pressure, Traverse speed, Abrasive flow rate, Stand-off distance	Surface roughness, Delamination	Optimized parameters achieved significant improvements in surface roughness and delamination. Provided insights for high-quality machining of jute-polymer composites.
Fowler et al. (2005) [46]	Grit embedment in AWJ milling	Ti6Al4V	Water pressure, Traverse speed, Abrasive grit size, Standoff distance	Grit embedment, Surface quality	High-speed milling at low impingement angles minimized grit embedment. Provided insights for achieving better surface quality and enhancing AWJ applicability in precision machining.
Yuan et al. (2020) [47]	AWJ milling of circular pockets	Ti6Al4V	Water pressure, Traverse speed, Abrasive flow rate, Standoff distance	Milling depth, Surface roughness	Developed material removal model. Identified optimal parameters to improve milling depth and surface roughness. Enhanced AWJ's suitability for precision applications in high-performance industries.
Fowler et al. (2009) [48]	Impact of particle hardness and shape on AWJ milling	Ti6Al4V	Particle hardness, Particle shape, Traverse speed, Standoff distance	Material removal rate, Surface roughness	Harder, angular particles increased material removal rates but also roughened surfaces. Optimizing abrasive selection and traverse speed crucial for balancing efficiency and surface quality.
Ebeid et al. (2014) [49]	ANN model for predicting AWJ milling parameters	Aluminum alloys	Water pressure, Traverse speed, Abrasive flow rate, Standoff distance	Surface roughness, Depth of cut, Material removal rate	High accuracy in predicting surface roughness, depth of cut, and material removal rate. Offered tool for optimizing AWJ performance and improving machining outcomes.
Kumar et al. (2020) [50]	AWJ cutting optimization for GFRP composites	GFRP composites	Water pressure, Traverse speed, Abrasive flow rate, Stand-off distance	Material removal rate, Kerf width, Taper angle	Emphasized importance of balancing parameters for optimal performance. Achieved better material removal rates, kerf width, and taper angle.
Alberdi et al. (2010) [51]	AWJ slot milling prediction model	Aluminum 7075-T651	Water pressure, Traverse speed, Abrasive flow rate, Stand-off distance	Kerf profiles, Material removal rate	Developed model to predict kerf profiles in AWJ slot milling. Identified optimal parameter combinations for stable milling conditions, ensuring consistent quality and productivity.
Srinivasu and Axinte (2014) [52]	PWJ milling strategy development	Advanced engineering composite materials	Water pressure, Traverse speed, Abrasive flow rate, Standoff distance	Surface damage, Material removal rate	Developed novel milling strategy to minimize surface damage and improve quality. Highlighted PWJ's advantages for high-performance applications, reducing thermal stresses and tool wear.
Chithirai Pon Selvan (2014) [53]	Empirical model for predicting depth of cut in AWJ cutting	Titanium	Water pressure, Traverse speed, Abrasive flow rate, Stand-off distance	Depth of cut	Validated model provided reliable predictions, helping optimize process parameters. Enhanced machining performance and precision.
Gokul et al. (2015) [54]	AWJ pocket milling optimization	Acrylic	Standoff distance, Step-over size, Traverse speed, Abrasive flow rate	Depth of cut, Material removal rate	Identified significant factors affecting depth of cut and material removal rate. Demonstrated AWJ's potential for efficient machining of acrylic.
Shipway et al. (2005) [55]	Surface characteristics of Ti6Al4V post-AWJ milling	Ti6Al4V	Water pressure, Traverse speed, Abrasive flow	Surface roughness, Waviness, Grit embedment	Identified optimal parameters to balance material removal rate and surface quality. Provided insights for improving AWJ processes.

			rate, Standoff distance		
Cenac et al. (2013) [56]	AWJ milling optimization for aeronautic aluminum	Aluminum 2024-T3	Water pressure, Traverse speed, Abrasive flow rate, Stand-off distance	Milled depth, Abrasive mass flow rate	Developed models to predict milled depth. Identified optimal abrasive mass flow rates and provided insights into micro-cutting and lateral cracking mechanisms.
Dittrich et al. (2014) [57]	Water abrasive fine jet machining for ceramics	Ceramic surfaces	Water pressure, Abrasive flow rate, Traverse speed, Standoff distance	Surface structure, Material removal rate	Identified critical parameters like water pressure and abrasive flow rate. Demonstrated potential for precise and reproducible machining of ceramics.
Gupta et al. (2015) [58]	ANN model for predicting micro-channel characteristics	SS304	Water pressure, Traverse speed, Abrasive flow rate, Standoff distance	Micro-channel geometry	High accuracy in predicting micro-channel characteristics. Demonstrated ANN's capability to optimize AWJ processes and improve machining performance and dimensional accuracy.
Kanthababu et al. (2016) [59]	AWJ pocket milling optimization	Ti6Al4V	Water pressure, Traverse speed, Abrasive flow rate, Stand-off distance	Depth of cut, Surface roughness	Identified step-over and traverse rate as significant factors. Emphasized need for careful optimization to achieve desired machining outcomes.
Gong and Kim (1996) [60]	Erosion model for AWJ milling	Polycrystalline ceramics	Water pressure, Traverse speed, Abrasive flow rate, Standoff distance	Material removal rate, Erosion profile	Identified 90° incidence angle as optimal for maximum erosion. Model provided insights into material removal mechanisms, enhancing AWJ efficiency for ceramics.
Paul et al. (1998) [61]	AWJ rectangular pocket milling optimization	Various materials	Water pressure, Traverse speed, Abrasive flow rate, Standoff distance	Depth variation, Material removal rate	Developed empirical models for predicting outcomes. Reduced depth variation and improved material removal rate. Demonstrated AWJ's potential for precise and efficient material removal.
Ebeid et al. (2023) [62]	PWJ milling parameter optimization	Aluminum alloy	Water pressure, Traverse speed, Abrasive flow rate, Stand-off distance	Milling performance, Surface quality	Identified effects of key parameters on milling performance. Provided insights for improving PWJ machining efficiency and surface quality.
Siddiqui and Shukla (2023) [63]	AWJ depth of cut prediction model	Thick Kevlar-epoxy composites	Water pressure, Traverse speed, Abrasive flow rate, Standoff distance	Depth of cut, Surface quality	Validated model offered precise predictions and optimization guidelines. Ensured effective cutting and high-quality finishes.
Fowler et al. (2005) [64]	AWJ milling parameter optimization	Ti6Al4V	Water pressure, Traverse speed, Abrasive grit size, Standoff distance	Material removal rate, Surface roughness, Waviness	Identified optimal parameters for balancing material removal rate, surface roughness, and waviness. Provided crucial insights for optimizing AWJ processes.
Pal and Tandon (2012) [65]	AWJ milling depth and material characteristics analysis	Various materials	Water pressure, Traverse speed, Abrasive flow rate, Stand-off distance	Machining time, Material removal rate	Identified material properties and machining parameters influencing outcomes. Offered insights for optimizing AWJ processes for different materials.
Feng et al. (2007) [66]	AWJ milling optimization for Al2O3 ceramics	Al2O3 ceramics	Water pressure, Traverse speed, Abrasive flow rate, Standoff distance	Surface quality, Material removal rate	Higher nozzle traverse speeds improved surface quality, while higher feeds reduced it. Provided insights for balancing efficiency and surface quality in AWJ milling of ceramics.
Müller et al. (2021) [67]	AWJ vs. WJ cutting comparison	PP and PVC-U materials	Traverse speed	Kerf width, Taper angle, Burrs	AWJ achieved more uniform cuts without delamination, highlighting its effectiveness for precise cutting of coated polymer materials.
Chen et al. (2023) [68]	AWJ machining performance model	Ductile materials	Water pressure, Traverse speed, Abrasive flow rate, Standoff distance	Effective depth of cut	Accurate predictions enhanced AWJ machining performance, offering significant industrial value for high-quality surface finishes in materials like Ti-6Al-4V.
Vishnu and Saleeshya (2021) [69]	AWJ machining parameter optimization	Inconel 718	Water pressure, Traverse speed, Abrasive flow rate, Standoff distance	Surface quality, Kerf taper	Optimized parameters achieved better surface quality and minimal kerf taper. Provided guidelines for machining complex profiles in hard-to-machine materials like Inconel 718.
Begic-Hajdarevic et al. (2015) [70]	AWJ cutting parameter optimization for various materials	Various materials	Water pressure, Traverse speed, Abrasive flow rate, Stand-off distance	Surface roughness	Highlighted importance of optimizing parameters to achieve desired machining outcomes. Provided practical insights for improving AWJ processes across different materials and applications.